UNIVERSITY OF SOUTHAMPTON

Faculty of Engineering and Physical Sciences
School of Chemistry

Combining X-ray Free Electron Laser Probes of Chemical Dynamics

by

Weronika Olimpia Razmus
ORCiD: 0009-0009-8926-9957

A thesis for the degree of
Doctor of Philosophy

February 10, 2025

University of Southampton

Abstract

Faculty of Engineering and Physical Sciences
School of Chemistry

Doctor of Philosophy

Combining X-ray Free Electron Laser Probes of Chemical Dynamics

by Weronika Olimpia Razmus

The development of ultrafast laser sources capable of generating extreme ultraviolet (XUV) and X-ray photons has significantly advanced the study of photochemical processes. This thesis investigates the use of Free Electron Lasers (FELs) as powerful probes for time-resolved spectroscopy, enabling detailed examination of molecular dynamics. Additionally, an experiment utilising a high harmonic generation source (HHG) is also described in this thesis. This provides a comparison and an overview of how the two sources can be used to complement one another.

The focus of the experimental work is on 2- and 3-iodothiophene. Ultraviolet (UV) excitation within the 220–300 nm range populates either $\pi\pi^*$ states localized on the thiophene ring or $(n/\pi)\sigma^*$ states on the C-I bond, both leading to C-I bond dissociation. The iodine fragment was observed to form via competing dissociation pathways, consistent with earlier studies. Direct $(n/\pi)\sigma^*$ excitation results in prompt dissociation, while initial population of the $\pi\pi^*$ state leads to slower, potentially delayed fragmentation.

By harnessing FEL and HHG radiation, the post-excitation dynamics of iodothiophene were probed through various techniques. Each method offers unique insights, collectively providing a comprehensive understanding of the underlying photodissociation dynamics.

This Thesis is based on the following publications:

Chapter 3:

- **W.O. Razmus**, F. Allum, J. Harries, Y. Kumagai, K. Nagaya, S. Bhattacharyya, M. Britton, M. Brouard, P.H. Bucksbaum, K. Cheung, S.W. Crane, M. Fushitani, I. Gabalski, T. Gejo, A. Ghrist, D. Heathcote, Y. Hikosaka, A. Hishikawa, P. Hockett, E. Jones, E. Kukk, H. Iwayama, H.V.S. Lam, J.W. McManus, D. Milesevic, J. Mikosch, S. Minemoto, A. Niozu, A. J. Orr-Ewing, S. Owada, D. Rolles, A. Rudenko, D. Townsend, K. Ueda, J. Unwin, C. Vallance, A. Venkatachalam, S-i. Wada, T. Walmsley, E.M. Warne, J.L. Woodhouse, M. Burt, M.N.R. Ashfold, R.S. Minns and R. Forbes, *Exploring the ultrafast and isomer-dependent photodissociation of iodothiophenes via site-selective ionization*, Phys. Chem. Chem. Phys., 2024, **26**, 12725-12737

In addition, contributions were made to the following publications:

- **W.O. Razmus**, K. Acheson, P. Bucksbaum, M. Centurion, E. Champenois, I. Gabalski, M. C. Hoffman, A. Howard, M-F. Lin, Y. Liu, P. Nunes, S. Saha, X. Shen, M. Ware, E.M. Warne, T. Weinacht, K. Wilkin, J. Yang, T.J.A. Wolf, A. Kirrander, R.S. Minns, and R. Forbes, *Multichannel photodissociation dynamics in* CS_2 *studied by ultrafast electron diffraction*, Phys. Chem. Chem. Phys., 2022, **24**, 15416-15427
- I. Gabalski, M. Sere, K. Acheson, F. Allum, S. Boutet, G. Dixit, R. Forbes, J.M. Glowina, N. Goff, K. Hegazy, A.J. Howard, M. Liang, M.P. Minitti, R.S. Minns, A. Natan, N. Peard, **W.O. Razmus**, R.J. Sension, M.R. Ware, P.M. Weber, N. Werby, T.J.A. Wolf, A. Kirrander and P.H. Bucksbaum, *Transient vibration and product formation of photoexcited* CS_2 *measured by time-resolved X-ray scattering*, J. Chem. Phys., 2022, **157**, 164305
- J. Unwin, F. Allum, M. Britton, I. Gabalski, H. Bromberger, M. Brouard, P.H. Bucksbaum, T. Driver, N. Ekanayake, D. Garg, E. Gougoula, D. Heathcote, A.J. Howard, P. Hockett, D.M.P. Holland, S. Kumar, C-S. Lam, J.W.L. Lee, J. McManus, J. Mikosch, D. Milesevic, R.S. Minns, C.C. Papadopoulou, C. Passow, **W.O. Razmus**, A. Roder, A. Rouzee, M. Schuurman, A. Simao, A. Stolow, A. Tul-Noor, C. Vallance, T. Walmsley, D. Rolles, B. Erk, M. Burt and R. Forbes, *X-ray induced Coulomb explosion imaging of transient excited-state structural rearrangements in* CS_2, Comm. Phys., 2023, **6**, 309
- I. Gabalski, F. Allum, I. Seidu, M. Britton, G. Brenner, H. Bromberger, M. Brouard, P.H. Bucksbaum, M. Burt, J.P. Cryan, T. Driver, N. Ekanayake, B. Erk, D. Garg, E. Gougoula, D. Heathcote, P. Hockett, D.M.P. Holland, A.J. Howard, S.

Kumar, J.W.L. Lee, S. Li, J. McManus, J. Mikosch, D. Milesevic, R.S. Minns, S. Neville, A-T. Noor, C.C. Papadopoulou, C. Passow, **W.O. Razmus**, A. Roder, A. Rouzee, A. Simao, J. Unwin, C. Wallanve, T. Walmsley, J. Wang, D. Rolles, A. Stolow, M.S. Schuurman and R. Forbes, *Time-Resolved X-Ray Photoelectron Spectroscopy: Ultrafast Dynamics in* CS_2 *Probed at the S 2p Edge*, J. Phys. Chem. Lett, 2023, **31**, 7126-7133

- A.L. Grite, M.A. Parkes, **W.O. Razmus**, Y. Zhang, A.S. Wyatt, E. Springate, R.T. Chapman, D.A. Horke and R.S. Minns, *Direct Observation of a Roaming Intermediate and Its Dynamics*, J. Am. Chem. Soc., 2024, **146**, 12595-12600

- J. Unwin, **W.O. Razmus**, F. Allum, J.R. Harries, Y. Kumagai, K. Nagaya, M. Britton, M. Brouard, P. Bucksbaum, M. Fushitani, I. Gabalski, T. Gejo, P. Hockett, A.J. Howard, H. Iwayama, E. Kukk, C-S. Lam, J. McManus, R.S. Minns, A. Niozu, S. Nishimuro, J. Niskanen, S. Owada, J.D. Pickering, D. Rolles, J. Somper, K. Ueda, S-I. Wada, T. Walmsley, J.L. Woodhouse, R. Forbes, M. Burt and E.M. Warne, *Time-Resolved Probing of the Iodobenzene C-Band Using XUV-Induced Electron Transfer Dynamics*, ACS Phys. Chem. Au, 2024, *Special Issue*

Additionally, manuscripts are in preparation based on work presented in Chapters 4 & 5

Contents

List of Figures **ix**

List of Tables **xiii**

Declaration of Authorship **xv**

Acknowledgements **xvii**

1 Introduction **1**
- 1.1 Potential Energy Surfaces . . . 3
- 1.2 Photo-excitation . . . 5
- 1.3 Relaxation . . . 7
- 1.4 Photoinduced Dynamics of Iodothiophenes . . . 9
- 1.5 Pump-probe spectroscopy . . . 13

2 Light Sources **15**
- 2.1 Generating Probe Pulses . . . 15
  - 2.1.1 Free Electron Lasers . . . 16
    - 2.1.1.1 Self-Amplified Spontaneous Emission Free Electron Lasers 17
    - 2.1.1.2 Seeded Free Electron Lasers . . . 18
  - 2.1.2 Current state-of-the-art . . . 19
  - 2.1.3 High Harmonic Generation . . . 20
- 2.2 Generating Pump Pulses . . . 25
  - 2.2.1 Ti:Sapphire Lasers . . . 25
  - 2.2.2 Non-linear Crystals . . . 25
  - 2.2.3 Optical Parametric Amplifiers . . . 27
  - 2.2.4 Data analysis . . . 28

3 Time-resolved Coulomb Explosion Imaging Study of Iodothiophene Dissociation Dynamics **29**
- 3.1 Introduction . . . 30
  - 3.1.1 Principles of Inner-Shell Ionisation . . . 31
    - 3.1.1.1 Charge Transfer in pump-probe measurements . . . 33
- 3.2 Experimental details . . . 34
- 3.3 Data Treatment . . . 36
  - 3.3.1 FEL flutations . . . 36
  - 3.3.2 Time-of-flight calibration . . . 37
    - 3.3.2.1 UV only mass spectrum . . . 38

3.3.3 Determination of time-zero 38
3.4 Results and Discussion 41
3.4.1 Pump-probe mass spectra 41
3.4.2 Ion images 42
3.4.3 Time-resolved Momentum Distributions 45
3.4.4 Data Fitting 47
3.4.5 Energy partitioning in the fragments 54
3.4.6 Discussion of the dissociation dynamics 56
3.5 Conclusions 59

4 Time-resolved X-ray Scattering Study of Iodothiophene Dissociation Dynamics 61
4.1 Introduction 61
4.1.1 Principles of X-ray scattering 62
4.1.2 Elastic scattering 63
4.1.3 Inelastic scattering 65
4.1.4 Scattering from molecules 66
4.2 Experimental Details 68
4.3 Data Treatment 70
4.3.1 FEL fluctuations 70
4.3.2 Image integration 71
4.3.3 Detector Geometry Calibration 71
4.4 Results 74
4.4.1 Dynamics Scattering Results 74
4.4.2 Frequency-resolved spectrum 76
4.4.3 Data Fitting 78
4.5 Discussion 80
4.6 Conclusion 82

5 Time-resolved Valence Photoelectron Study of Iodothiophene Dissociation Dynamics 83
5.1 Introduction 83
5.1.1 Principles of time-of-flight spectrometry 86
5.2 Experimental Details 87
5.3 Data Treatment 88
5.4 Results 90
5.4.1 245 nm data 90
5.4.2 262 nm data 93
5.5 Discussion 94
5.6 Conclusion 96

6 Summary 97

List of Figures

1.1 Schematic representation of two potential energy surfaces overlapped with their corresponding vibrational wavefunctions. Vertical arrows illustrate the most likely transitions according to Frank-Condon principle. In this case: excitation from v=0 vibrational level of the lower potential energy surface to v=2 level of the upper surface, as well as a relaxation from v=0 of the upper surface to v=2 of the lower since the overlap is greatest between those vibrational wavefunctions. 4
1.2 Schematic representation of three potential energy surfaces including: the ground electronic state S_0, the first excited singlet state S_1 and the first excited triplet state T_1. Conical intersections between two electronic states, where their energies become degenerate, are circled. Reproduced from [15] 7
1.3 A ball and stick representation of 2-iodothiophene (2IT) and 3-iodothiophene (3IT). In both structures carbon atoms are grey, hydrogen is white, iodine is pink and sulfur is yellow. 9
1.4 A schematic representation of the main PESs involved in photodissociation dynamics observed in iodothiophenes including: the ground state (solid lines), the $(n/\pi)\sigma^*$ state (dashed lines) and the $\pi\pi^*$ state (dotted lines). Presented as a function of a) increasing C-I distance and b) C-S distance. Constructed with the aid of calculations from [22]. 10
1.5 A schematic representation of a pump-probe experimental set up. The pump and probe pulses intersect within a gaseous sample. A movable delay stage is placed in the path of the pump laser beam in order to control the time delay between the two pulses by varying the beam path length. 13

2.1 Schematic representation of an undulator in an FEL set up showing electron bunch separating into micro-bunches as it progresses through the length of the system facilitating coherent emission. 17
2.2 The three step model of a HHG process. The point of the laser electric field at each step is marked in red, below are the resulting shape of the atomic PES and the position of the electron. 21

3.1 The energy scheme of the four highest occupied atomic orbitals of iodine Panel a) highlights in purple the orbitals which are energetically accessible with a 95 eV photon. Panel b) shows the creation of a core hole by ionising an electron from the 4d orbital following absorption of the 95 eV photon. Panel c) depicts the Auger-Meitner decay mechanism which sees the core hole filled by a higher lying electron leading to the ejection of a secondary electron from the same orbital. 31

3.2 A histogram of A) FEL pulse power and B) FEL arrival time jitter of all shots recorded as part of the analysed dataset. Dashed vertical lines mark the subset of data carried forward for analysis. 36

3.3 Mass spectra obtained following ionisation of 2IT (blue) and 3IT (orange) with 2 μJ of 262 mn UV pump alone. Both spectra are normalised to the total number of shots combined to produce them. 38

3.4 Residual difference between experimental data and the fit described in Section 2.4.4 of I^{2+} obtained following photolysis of 2IT. Illustrating the characteristic "hockey-stick" signal (red) associated with classic Coulomb Explosion. 39

3.5 Integrated intensity between 150-200 arb. units of the residual between simulated and experimental data as a function of pump-probe delay(blue). An error function was fit using pre-time zero baseline and asymptotic intensity, the result is shown in red. 40

3.6 Mass spectra obtained from ionisation of 2IT a) and 3IT b) by UV + XUV pulses (red) and by XUV pulses only (blue). Each spectrum has been normalised by the total number of shots. The UV + XUV signal has been summed over all positive pump-probe delays (i.e. with the UV pulse preceding the XUV pulse). 41

3.7 Ion images of iodine photoproducts in charge states from 2+ to 5+ following ionisation of 2IT by XUV only (column a)), pumped by UV and subsequently ionised: summed over 200-500 fs (column b) and at all delays >3 ps (column c)). 43

3.8 Ion images of iodine photoproducts in charge states from 2+ to 5+ following ionisation of 3IT by XUV only (column a)), pumped by UV and subsequently ionised: summed over 200-500 fs (column b) and at all delays >3 ps (column c) 44

3.9 Time-resolved difference maps of the momentum distributions of the a)I^{2+}, b) I^{3+}, c) I^{4+} fragments formed followed by 262 nm photolysis of A) 2IT and B) 3IT and subsequent ionization with XUV probe. The ground state contribution (UV arriving after XUV) was subtracted. The momentum distributions at early (200-500 fs) and late (>3 ps) pump-probe delays are projected on the right-hand side of the panels as orange and purple lines respectively. The black dashed lines depict the expected appearance times of the fragments based on the OBT model. 46

3.10 Figures summarizing the fitting procedure described in text of the momentum distributions of the A)I^{2+}, B) I^{3+}, C) I^{4+} fragments formed followed by 262 nm photolysis of 2IT. a) Momentum basis functions depicting the ground state (green), prompt dissociation (blue) and delayed dissociation (red) momentum distributions. Shown with common peak intensity. b) Fit to the experimental data using a time-varying sum of the three basis function as per Equation 3.12 c) Residual error between the experimental and fitted data . d) Time-dependent amplitudes of the basis functions obtained from the fit using the same color scheme as panel a). 49

3.11 Figures summarizing the fitting procedure described in text of the momentum distributions of the A)I^{2+}, B) I^{3+}, C) I^{4+} fragments formed followed by 262 nm photolysis of 3IT. a) Momentum basis functions depicting the ground state (green), prompt dissociation (blue) and delayed dissociation (red) momentum distributions. Shown with common peak intensity. b) Fit to the experimental data using a time-varying sum of the three basis function as per Equation 3.12 c) Residual error between the experimental and fitted data . d) Time-dependent amplitudes of the basis functions obtained from the fit using the same color scheme as panel a). 50

3.12 TKER distributions obtained from the I^{2+} asymptotic velocity distributions from 262 nm photolysis of (a) 2IT (blue) and (b) 3IT (red), assuming two-body dissociation into I + C_4H_3S. The dashed curves show the TKER distributions associated with the 'prompt' and 'delayed' dissociation channels (derived from the respective momentum basis functions), while the dashed vertical lines show the maximum TKER values associated with forming I and I* photoproducts, given $D_0(\mathrm{R-I}) = 24,500\ \mathrm{cm}^{-1}$. 54

3.13 Gas phase absorption spectrum of 2IT a) and 3IT b) are plotted as solid lines along with a scaled absorption spectrum of CH_2BrI (dashed line) to emphasise the weak long wavelength absorption attributable to nσ^* excitation in both 2- and 3-iodothiophene. The intensity scale has been normalized to the maximum measured for each isomer to show relative changes in the shape. The structure of the two isomers are plotted as insets with the C-I bond vector highlighted as a dashed blue line and the center of mass of the thiophenyl radical marked by a star. Measured by collaborator Felix Allum. 56

3.14 A schematic representation of the main PESs involved in photodissociation dynamics observed in 2IT and 3IT following excitation at 262 nm including: the ground state (solid line), the $(n/\pi)\sigma^*$ state (dashed line) and the $\pi\pi^*$ state (dotted line). Constructed with the aid of calculations from [22]. Proposed pathways as described in text marked by red arrows. 59

4.1 A schematic representation of an incident x-ray beam being scattered by an electron within an atom's electronic cloud. 63

4.2 Theoretical form factors of iodine (blue), sulfur (orange), carbon (green), and hydrogen (red).[107] 64

4.3 Theoretical scattering pattern for 2IT calculated using Equation 4.1.4, showing the total scattering pattern (blue solid line) as well as the molecular (orange), atomic (green), and inelastic (red) scattering components as dashed lines. The atomic scattering patterns are taken from Ref. [107] 67

4.4 A histogram of a) FEL arrival time jitter and b) FEL pulse power of all shots recorded as part of the dataset. Dashed vertical lines mark the subset of data chosen for further analysis. 70

4.5 Scattering pattern of ground state of SF_6 calculated using the IAM (solid orange line) and the experimental scattering pattern (blue crosses) used to calibrate the detector position as desribed in text. Both patterns are multipled by momentum transfer vector q to improve visibility at large q values. 72

4.6 Scattering pattern of ground state of 2IT calculated using the IAM (solid red line) and adjusted for Compton Scattering, and the experimental scattering pattern (blue crosses). Both patterns are multiplied by momentum transfer vector q to improve visibility at large q values. 73
4.7 Time-resolved difference map of scattering intensity as a function of the momentum transfer, q, and pump-probe delay (fs) following excitation by a 252 nm photon. 74
4.8 FRXS representation of the TRXS data in the range $-200 < t < 1200$ fs. The dissociation velocities calculated through the Hough transform approach described in text are marked as dashed lines for 6.42 Å/ ps (green) and 16.95 Å/ ps (red). 76
4.9 Velocity - resolved Hough transform taken for y-intercept $v_0 = 0$ (blue solid line). The gaussian fits used to describe the two dissociating pathways peaking at 6.42 Å/ ps (red) and 16.95 Å/ ps (green) are shown as dashed lines. 77
4.10 a) Time-resolved difference map of scattering intensity as a function of the momentum transfer q, and pump-probe delay (fs) calculated using the fitting procedure described in text. b) Residual error between the experimental and fitted data. 79
4.11 A schematic representation of the main PESs involved in photodissociation dynamics observed in 2IT following excitation at 252 nm including: the ground state (solid line), the $(n/\pi)\sigma^*$ state (dashed line) and the $\pi\pi^*$ state (dotted line). Constructed with the aid of calculations from [22]. Proposed pathways as described in text marked by red arrows. 82

5.1 A simple schematic representation of a time-of-flight spectrometer. Higher energy electrons are shown in light blue and slower ones in dark blue. . 86
5.2 Difference spectrum following photolysis of 2IT using a 245 nm laser pulse. The ground state deletions are shown in blue and increased populations of other states in red. The intensity on the left hand side of the green dashed line is multiplied by 10 to make the lower intensity features clearer, ... 90
5.3 Total difference photoelectron intensities following photolysis of 2IT with a 245 nm laser pulse in the energy regions: a)3.8-4.2 eV, b) 7.25-8.0 eV, c) 10.38-10.53 eV and d) 11.2-11.45 eV. The measured intensities are shown in blue with "x" marking the data points and fits in panels c) and d) are shown as red dashed lines. A vertical dashed line marks the centre of rise calculated in the fit. 92
5.4 Difference spectrum following photolysis of 2IT using a 262 nm laser pulse. The ground state deletions are shown in blue and increased populations of other states in red. The intensity on the left hand side of the green dashed line is multiplied by 60 to make the lower intensity features clearer, ... 93
5.5 Total difference photoelectron intensities following photolysis of 2IT with a 262 nm laser pulse in the energy regions: a)3.8-4.2 eV, b) 7.25-8.0 eV. . 94
5.6 A schematic representation of the main PESs involved in photodissociation dynamics observed in 2IT following population of the $\pi\pi^*$ state (dotted) including: the ground state (solid line), the $(n/\pi)\sigma^*$ state (dashed line). Constructed with the aid of calculations from [22]. Proposed pathway to a ring-opened structure as described in text marked by red arrows. 96

List of Tables

3.1 Calculated total atomic absorption cross section, σ_{tot}, and relative cross sections,σ_{rel}, for photoionisation of all atoms in iodothiophene at the photon energy of 95 eV. Data taken from [79]. 31
3.2 Calculated atomic absorption cross section, σ_{abs}, for all energetically accessible iodine orbitals at 95 eV. Data taken from [79] 32
3.3 Values of k_i, and t_i obtained from fitting the experimental data to equation 3.12 as well as the expected apperance times calculated using Equation 3.4 assuming instantaneous bond breaking and acceleration to asymptotic velocities. 52

Declaration of Authorship

I declare that this thesis and the work presented in it is my own and has been generated by me as the result of my own original research.

I confirm that:

1. This work was done wholly or mainly while in candidature for a research degree at this University;
2. Where any part of this thesis has previously been submitted for a degree or any other qualification at this University or any other institution, this has been clearly stated;
3. Where I have consulted the published work of others, this is always clearly attributed;
4. Where I have quoted from the work of others, the source is always given. With the exception of such quotations, this thesis is entirely my own work;
5. I have acknowledged all main sources of help;
6. Where the thesis is based on work done by myself jointly with others, I have made clear exactly what was done by others and what I have contributed myself;
7. Parts of this work have been published in Razmus et.al., Phys. Chem. Chem. Phys., 2024, **26**, 12725-12737. Further manuscripts are in preparation based on the work presented in Chapters 4 and 5.

Signed:.. Date:..................

Acknowledgements

First and foremost, I would like to thank and acknowledge my PhD supervisor Russell Minns. In the last four years he has shown me unwavering support, a great deal of understanding and his ability to remain calm in all situations will forever astound me. I would also like to thank the other members of the Minns group. To Joanne Woodhouse, Ned Plackett, Emily Warne and Briony Downes-Ward for helping me ease into the project during the difficult time of the pandemic and social distancing. Special thank you to Joanne Woodhouse for countless coffees and discussions about lab infrastructure as well as experimental data (and many other topics in between).

During the project I have had an amazing opportunity to collaborate with many amazing people around the world. It would be impossible to list everyone individually therefore a massive thank you goes collectively to the many amazing beamline scientists who made the experiments possible as well as the research groups who showed up to handle the large volumes of data that was collected. Special thanks go to Ruaridh Forbes and Felix Allum who have been recurring figures in my PhD journey, kindly inviting me to participate in their experiments as well as spending hours of their time on zoom discussing data with me and freely sharing their experiences and expertise.

Outside of the academic world, I would like to thank Jared Wason for his excellent guardianship of my sanity. Thank you for always listening, never judging and sometimes understanding what I am ranting about.

Chapter 1

Introduction

Photochemistry, the study of chemical reactions and processes induced by light absorption, plays a fundamental role in nature and technology. Energy carried by light can be utilised in numerous applications via photophysical and photochemical processes. From understanding the mechanisms that drive photosynthesis in plants [1] to the design of solar cells [2], the principles of photochemistry underpin numerous scientific and technological advancements. A significant number of photochemical processes are considered ultrafast as they occur on the timescale of the vibrational motion of a molecule. A typical period of a vibrational mode is of the order of hundreds of femtoseconds (fs) [3]. Consequently, it is challenging to investigate these processes by using conventional light sources which tend to have much longer pulse durations.

The relevance of photochemical research was highlighted when the 1999 Nobel Prize was awarded to Ahmed Zewail, who became colloquially known as the ″father of femtochemistry″, for his observation of bond-breaking processes on the femtosecond scale [3]. His seminal research in 1985 employed Ti-sapphire mode-locked lasers to examine the light-induced C-I bond cleavage in ICN [4, 5]. The study recorded a 600 fs rise time for iodine product formation [4]. Since then pump-probe spectroscopy became widely employed, where an initial ″pump″ pulse excited the system, and a time-delayed ″probe″ pulse monitored the subsequent dynamics.

Visible and near-infrared lasers, particularly mode-locked Ti:Sapphire systems, dominated this field due to their ability to generate femtosecond pulses with high temporal resolution. Techniques such as transient absorption spectroscopy [6], time-resolved fluorescence [7] and resonance Raman spectroscopy [8] provided valuable insights into excited-state lifetimes, energy relaxation pathways, and bond-breaking processes. However these methods were constrained by the limited spectral range of conventional lasers, typically spanning the visible to near-ultraviolet regions. Efforts to extend the capabilities included the use of synchrotron radiation and X-ray tubes, but their low brightness and longer pulse durations often limited their applicability to ultrafast timescales [9, 10]. These challenges underscored the need for advanced light sources capable of providing both ultrafast temporal resolution and broad spectral coverage, paving the way for Free-Electron Lasers (FELs) and High-Harmonic Generation (HHG) sources.

Photochemical research has been revolutionised by improvements in FEL and HHG light sources. FELs generate exceptionally bright, coherent, and tuneable light pulses spanning wavelengths from the infrared to the X-ray regions. These distinctive features allow for unprecedented temporal and spatial resolutions in probing photochemical reaction dynamics. Similarly, HHG sources, which transform intense laser light into a wide spectrum of high-order harmonics, are capable of providing pulses in the extreme ultraviolet (XUV) and soft X-ray domains with durations in the range of 10s of femtoseconds.

The primary objective of this thesis is to examine the utilisation of FEL and HHG light sources in photochemical dynamics research. This chapter introduces excited state dynamics in isolated gas-phase molecules and reviews current literature around photochemical dynamics observed in iodothiophenes, the selected molecular target. Chapter 2 presents an more in-depth overview of the light sources used in the experiments in this thesis. The subsequent three chapters investigate photoexcited iodothiophene dynamics using various probes enabled by these FEL and HHG light sources, each focusing on a distinct probing method: inner-shell ionisation, X-ray diffraction, and time-resolved valence photoelectron spectroscopy. The application of all three probes to one system offers a valuable opportunity to compare the information obtained through each technique and demonstrate how they can be combined to provide a comprehensive description of the dynamics. All experiments conducted during this PhD project used gaseous samples as targets, in the gas phase the interactions between molecules can be neglected. This allows the properties of molecules free from perturbations from an environment to be studied.

1.1 Potential Energy Surfaces

The properties of a molecular system can be described by the time-independent Schrödinger equation [11]. This equation allows the behavior of molecules to be understood at the quantum level by solving for the wavefunction (ψ_{total}), which is a mathematical function which when squared represents the probability distribution of particles (including both nuclei and electrons) within the molecule.

The time-independent Schrödinger equation is particularly useful for mathematically describing molecules which do not interact with an environment such as those in the gas phase. Using this equation, one can determine the allowed energy levels (E_n) of the molecular system as well as the spatial distribution of electrons in the molecular orbitals. This approach is essential for predicting the chemical properties, reaction dynamics, and stability of molecules. The time-independent Schrödinger equation is given by [11]:

$$\hat{H}\psi_{total} = E_n \psi_{total} \tag{1.1}$$

where $\hat{H}$ is the Hamiltonian of the molecular system, ψ_{total} is the wavefunction describing the molecular system and E_n is the total energy of the system.

The Hamiltonian of the molecular system is the sum of the electronic , T_e, and nuclear , T_N, kinetic energy operators as well as the potential energy of the entire system, V, such that:

$$\hat{H}(R,r) = \hat{T}_N(R) + \hat{T}_e(r) + \hat{V}(R,r) \tag{1.2}$$

where R and r represent the nuclear and electron coordinates, respectively. However, solving the Schrödinger equation directly presents significant challenges due to the complex interactions between nuclei and electrons in a molecule. A common approach to simplify this problem is to apply the Born-Oppenheimer approximation, which assumes the nuclei, being orders of magnitude heavier than the electrons, move at a considerably slower rate [12]. This assumption justifies the separate treatment of nuclear and electronic motions, allowing for the solution of the electronic Schrödinger equation with fixed nuclei positions. Consequently, the nuclear kinetic energy term can be neglected ($\hat{T}_N = 0$) to yield the electronic Hamiltonian, $\hat{H}_e(R,r)$:

$$\hat{H}_e(R,r) = \hat{T}_e(r) + \hat{V}(R,r) \tag{1.3}$$

When the time-independent Schrödinger equation is solved using the electronic Hamiltionian, the values of E_n give the adiabatic electronic potential energy. These

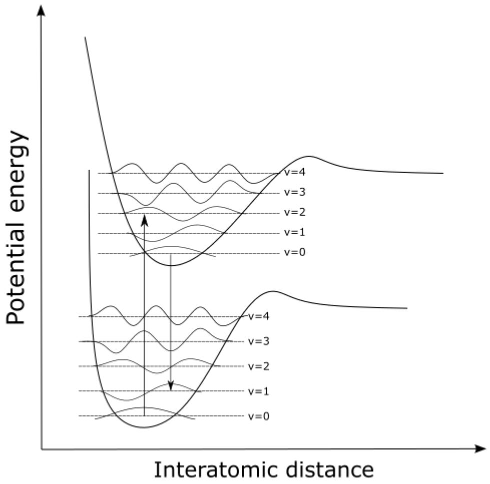

FIGURE 1.1: Schematic representation of two potential energy surfaces overlapped with their corresponding vibrational wavefunctions. Vertical arrows illustrate the most likely transitions according to Frank-Condon principle. In this case: excitation from v=0 vibrational level of the lower potential energy surface to v=2 level of the upper surface, as well as a relaxation from v=0 of the upper surface to v=2 of the lower since the overlap is greatest between those vibrational wavefunctions.

values characterise the electronic states within the molecular system. For each value of R, there exists a set of E_n eigenvalues and by varying the values of R and obtaining these energies at a range of nuclear geometries, surfaces of these states can be constructed; these are referred to as potential energy surfaces (PES), a depiction of adiabatic PES is shown in Figure 1.1.

While using the Born-Oppenheimer approximation greatly reduces the complexity involved with solving the Schrodinger equation, it can introduce errors in cases where the coupling between electronic and nuclear motions is significant. The spacing between the electronic states is typically significantly larger than the frequency of oscillations in the electric field experienced by electrons caused by nuclear vibrations. However, as the systems become more complex, the density of electronic states increases, decreasing the spacing between them. In some instances, oscillations in the electric field caused by nuclear vibrations may induce vibronic couplings and facilitate transitions between electronic states. A significant consequence of adiabatic coupling is the presence of conical intersections (CIs) between the potential energy surfaces of two or more electronic states. At a CI, the electronic states are degenerate in energy, enabling population transfer between the two electronic states [13].

1.2 Photo-excitation

The first step in a photochemical process is the absorption of light by the molecule. When a photon with sufficient energy is incident on the molecule, electrons may be promoted between molecular orbitals resulting in a molecule in a higher electronic state. The electromagnetic field of the incident light provides a perturbation to the system and the resulting probability of transition (per unit time) from a quantum state ψ_i to a quantum state ψ_f is given by Fermi's golden rule[14]:

$$T_{i\to f} = \frac{2\pi}{\hbar} \left| \langle \psi_f | \hat{H}' | \psi_i \rangle \right|^2 \rho_f \tag{1.4}$$

where $\hat{H}'$ is the perturbation Hamiltonian, and ρ_f is the density of final states.

The Frank-Condon principle is a concept in quantum chemistry and spectroscopy that is used to explain the relative intensities of the observed transitions between electronic states. The electronic transition dipole moment is assumed to be constant at the moment of excitation therefore only the change in vibrational states is considered. The principle states that the most intense transitions between any given two electronic states are those where the initial and final vibrational states overlap most significantly [14, 15]. To describe this mathematically, the probability of excitation to a single final vibrational state is considered. In such cases, the value of ρ_f becomes 1. The perturbation Hamiltonian for the electric-dipole transition is given by $\hat{H}' = -\hat{\mu} \cdot \hat{\epsilon}$, where $\hat{\mu}$ is the dipole moment operator, and $\hat{\epsilon}$ is the electric field. The wavelength of light typically used to excite the system is on the order of a few hundred nanometres; on the other hand, the typical size of the molecule is approximately two orders of magnitude smaller. This implies that the electric field experienced by the molecule is effectively constant, and $\hat{\epsilon}$ can be taken outside of the integral. With these considerations, the probability amplitude of the transition from a specific initial state (ψ_i) to a specific final state (ψ_f) becomes:

$$P_{i\to f} \propto \langle \psi_f | \hat{\mu} | \psi_i \rangle \tag{1.5}$$

The total dipole operator $\hat{\mu}$ is a sum over all particles within the system and may be separated into electronic, $\hat{\mu}^e$, and nuclear, $\hat{\mu}^n$, components ($\hat{\mu} = \hat{\mu}^e + \hat{\mu}^n$). Similarly, following the Born-Oppenheimer approximation, the wavefunctions for the initial and final states can be represented as the products of the electronic ψ^e, nuclear ψ^n, and spin ψ^s wavefunctions:

$$\psi_{total} = \psi^e \psi^n \psi^s \tag{1.6}$$

By substitution equation 1.5 becomes:

$$P_{i\to f} \propto \langle \psi_f^e \psi_f^n \psi_f^s | \, \hat{\mu}^e + \hat{\mu}^n \, | \psi_i^e \psi_i^n \psi_i^s \rangle \tag{1.7}$$

The terms relating to nuclear and electronic components can be further separated to give:

$$\begin{aligned} P_{i\to f} &\propto \langle \psi_f^e \psi_f^n \psi_f^s | \, \hat{\mu}^e \, | \psi_i^e \psi_i^n \psi_i^s \rangle + \langle \psi_f^e \psi_f^n \psi_f^s | \, \hat{\mu}^n \, | \psi_i^e \psi_i^n \psi_i^s \rangle \\ &\approx \underbrace{\langle \psi_f^e | \, \hat{\mu}^e \, | \psi_i^e \rangle}_{\text{orbital}} \; \underbrace{\langle \psi_f^n | \psi_i^n \rangle}_{\text{Frank$-$Condon}} \; \underbrace{\langle \psi_f^s | \psi_i^s \rangle}_{\text{spin}} + \underbrace{\langle \psi_f^e | \psi_i^e \rangle}_{=0} \langle \psi_f^n | \, \hat{\mu}^n \, | \psi_i^n \rangle \langle \psi_f^s | \psi_i^s \rangle \end{aligned} \tag{1.8}$$

From equation 1.8 it can be seen that none of the terms related to the nuclear component of the transition dipole, $\hat{\mu}_n$, contribute to the overall probability of transition. This is caused by multiplication with the term $\langle \psi_f^e | \psi_i^e \rangle$ which is equal to zero. As the electronic wavefunctions, ψ^e, are the eigenfunctions of a Hemitian operator they are orthogonal. In physical terms each one uniquely represents a distinct quantum state thus there is no overlap between them. Mathematically this results in $\langle \psi_f^e | \psi_i^e \rangle = 0$.

The key term describing the Frank-Condon principle is the second term of equation 1.8, namely $\langle \psi_f^n | \psi_i^n \rangle$. It describes the degree of overlap between initial and final vibrational wavefunctions. The greater the overlap, the higher the value of this term and therefore the more likely the transition. This is represented schematically in Figure 1.1. The figure shows two electronic PESs with typical vibrational energy levels overlaid on top. The wavefunction of the initial, $v = 0$, state has the greatest overlap with the $v = 2$ wavefunction of the excited state. Upon photoexcitation with a photon of sufficient energy the most likely transition is to the $v = 2$ vibrational state. This is visually represented by the shape of the wavefunction in the figure. Furthermore, it can be seen that the overlap is greatest near the edge of the of the PES, in classical terms this corresponds to the turning point of the vibrational motion (for example, the furthest point of a stretch). At the turning point the nuclear momentum is zero, since the momentum in the ground state is also zero, the transition may occur without any transfer of momentum to or from another part of the system, making it more likely to occur.

Additional factors affecting the probability of transitions also emerge from equation 1.8. The first term, $\langle \psi_f^e | \, \hat{\mu}^e \, | \psi_i^e \rangle$, mathematically describes the degree of overlap between the final electronic wavefunction and the initial electronic wavefunction once acted upon by the dipole operator. The inclusion of the dipole operator makes this different to the $\langle \psi_f^e | \psi_i^e \rangle$ case, making this term is non-zero. Finally the spectroscopic spin selection rule, which states that a transition which involves a change in spin multiplicity is not an allowed process, is described by the $\langle \psi_f^s | \psi_i^s \rangle$ term of equation 1.8. This rule is a direct consequence of the fact that the wavefunction of a molecule (or atom) must obey the Pauli exclusion principle, which requires that the overall wavefunction, including its spin part, remains antisymmetric for fermions [14].

1.3 Relaxation

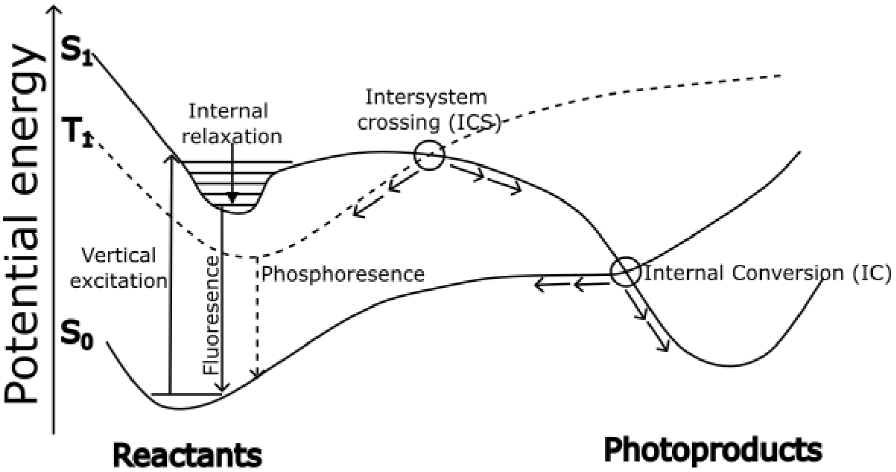

FIGURE 1.2: Schematic representation of three potential energy surfaces including: the ground electronic state S_0, the first excited singlet state S_1 and the first excited triplet state T_1. Conical intersections between two electronic states, where their energies become degenerate, are circled. Reproduced from [15]

Following the promotion of a molecule to a higher excited electronic state, various pathways allow the system to dissipate the acquired energy and either return to the ground electronic state or dissociate into photoproducts. Figure 1.2 illustrates possible relaxation pathways by depicting the PESs of three electronic states: the ground state S_0, the first excited singlet state S_1 and the first excited triplet state T_1. The initial excitation occurs from the ground, singlet, state S_0 vertically into the first (in this example) excited, singlet state S_1. Vertical excitation means that the molecule absorbs a photon and transitions to a higher energy level without changing its nuclear configuration, as described by the Frank-Condon principle. Once in the excited state, gas phase molecules cannot undergo internal relaxation, where energy would be lost until the molecule reached the lowest vibrational level within the S_1 state. The vibrational energy may be redistributed within different vibrational modes or the molecule may eventually return to the ground state via fluorescence, a radiative process in which the transition is accompanied by the emission of a photon, allowing the molecule to release excess energy.

Alternatively, the molecule can follow radiationless pathways, which are generally more complex and involve surface crossings between the PESs. These crossings can occur through conical intersections (CI) which serve as routes to transitions between states of the same multiplicity through internal conversion (IC) or between states of different multiplicities via intersystem crossing (ISC). If the molecule crosses into a triplet state, it can return to the ground state either by undergoing an additional ISC back to the singlet ground state or again by emitting a photon in a process known as phosphorescence, which typically occurs on a longer timescale than fluorescence.

A detailed understanding of the PESs is important for interpreting the photoinduced dynamics, as their topology can suggest likely pathways and outcomes. For example, sharp features, such as CIs, suggest a high likelihood of rapid radiationless transitions between electronic states. In contrast, smooth, deep wells on the PES correspond to stable nuclear configurations and may suggest fluorescence or phosphorescence as the more likely pathway. Moreover, the relative position and energy of CIs on the PES are important in determining the efficiency and speed of nonradiative processes. CIs can be considered as funnels which facilitate the conversion of electronic into vibrational energy. If the CI is close to the Frank-Condon region, where the initial photoexcitation occurs, the molecule may rapidly undergo IC. However, if significant nuclear rearrangement is required or an energy barrier is present, the lifetime of the transition can be expected to be longer. Overall, a PES provides a map of the energetic landscape that the molecule navigates following photoexcitation. By analysing these surfaces and comparing them to experimental observables, photochemical processes can be understood and potentially influenced.

1.4 Photoinduced Dynamics of Iodothiophenes

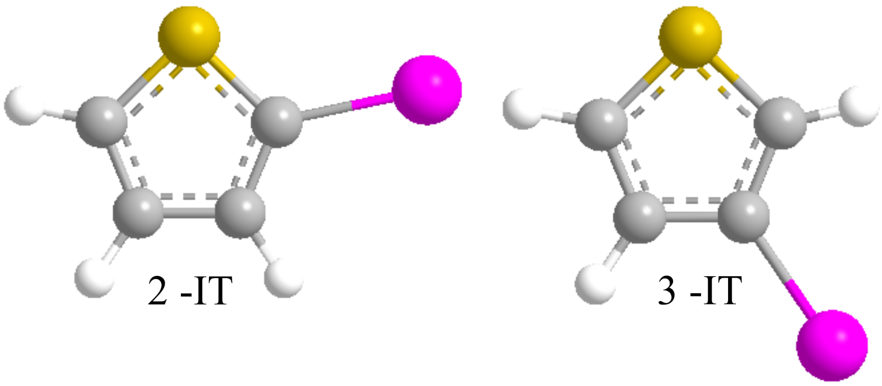

FIGURE 1.3: A ball and stick representation of 2-iodothiophene (2IT) and 3-iodothiophene (3IT). In both structures carbon atoms are grey, hydrogen is white, iodine is pink and sulfur is yellow.

Iodothiophene, depicted in Figure 1.3, is an organic compound in which an iodine atom is bonded to a thiophene ring at either the α (2IT) or β (3IT) position. These molecules present a compelling subject for photodissociation studies, not only because of their intricate electronic structure, but also because of their potential applications in organic electronics, where understanding their photoinduced behavior could lead to advances in materials science. The unique combination of the thiophene ring, a well-known building block in organic electronics, with the heavy iodine atom introduces a complex interplay of electronic states, making iodothiophene an ideal model for exploring the dynamics of photoexcitation and subsequent molecular processes [16–21].

Due to the quantum complexity of iodothiophene, the full PESs of its isomers have not been calculated. Figure 1.4 depicts a schematic interpretation of the main PESs involved in the photodynamics of iodothiophene. When iodothiophene absorbs light within the 220-300 nm wavelength range, an electron may be promoted to either the $(n/\pi)\sigma^*$ state localised on the C-I bond (depicted as dashed lines in Figure 1.4) or the $\pi\pi^*$ state predominately associated with the thiophene ring (depicted by a dotted line). The $(n/\pi)\sigma^*$ state is the result of the promotion of an electron from either a sigma (σ) or non-bonding (n) orbital into an anti-bonding sigma (σ^*) orbital, which weakens the C-I bond and predisposes it to dissociation. This results in a PES with a negative gradient leveling off at the energy associated with ground state fragments. On the other hand, the $\pi\pi^*$ state is populated by excitation from the bonding to the antibonding π orbitals localised on the thiophene ring. This transition can also lead to C-I bond cleavage, through a conical intersection visible in panel a) of Figure 1.4, ultimately resulting in the formation of a thiophene radical and an iodine atom. This dual pathway underscores the complexities present in iodothioophene excited state dynamics [22–24].

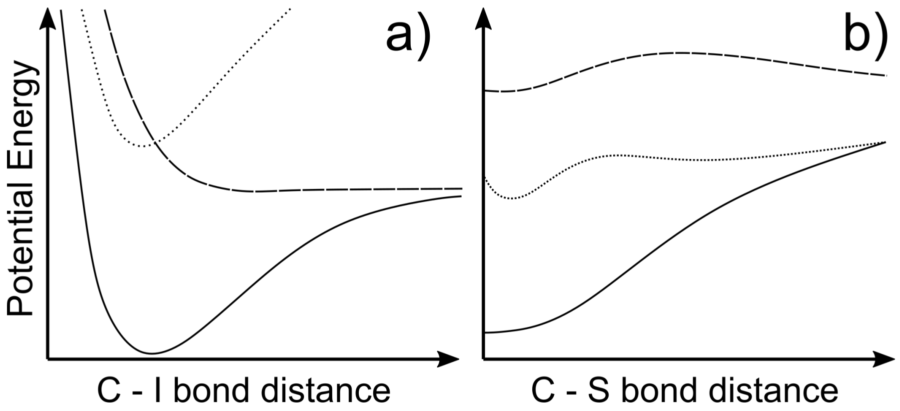

FIGURE 1.4: A schematic representation of the main PESs involved in photodissociation dynamics observed in iodothiophenes including: the ground state (solid lines), the $(n/\pi)\sigma^*$ state (dashed lines) and the $\pi\pi^*$ state (dotted lines). Presented as a function of a) increasing C-I distance and b) C-S distance. Constructed with the aid of calculations from [22].

Earlier studies on bare thiophene, particularly those involving resonance Raman spectroscopy conducted in 2010, revealed that excitation at 240 nm primarily indicated a $\pi \rightarrow \pi^*$ transition [25]. Raman spectroscopy is a technique used to determine the vibrational modes of molecules. The Raman spectra obtained for bare thiophene following excitation at 240 nm showed signals associated with vibrational modes which would allow the molecule to access a CI between the $\pi\pi^*$ PES and a "hot" ground state. This crossing could occur via either extension of the C-S bond or a puckering motion of the thiophene ring. The C-S bond extension indicates that the transition to the ground state may involve ring-opening motion. These findings were further confirmed by subsequent experimental and theoretical studies [25–29].

The behaviour of thiophenone, a derivative of thiophene with a carbonyl group present on the ring, can provide further insights into the possible dynamics of thiophene-like molecules. The system was initially studied using transient infrared absorption spectroscopy [30]. In the experiment, thiophenone was excited using 267 nm and the changes in the characteristic IR absorption features were monitored. These clearly showed signs of an antisymmetric ketene stretch, which confirms the presence of a ring-opening mechanism. This was further probed by a time-resolved photoelectron spectroscopy experiment which was able to track the changes in electronic states that the molecule goes through following photoexcitation [28]. This experiment, carried out at the FERMI FEL, was able to confirm the ring-opening pathway. By supporting their findings with *ab initio* calculations, the authors concluded that the initial ring-opening and nonadiabatic coupling to the ground state is driven by a ballistic C-S bond extension and deduced that the transition is complete within 350 fs. The study also highlighted the rich dynamics of the hot ground state which involves the formation of, and interconversion between, ring-opened and cyclic isomers and further fragmentation over much longer timescales [28, 30].

In iodothiophene, the introduction of a heavy iodine atom adds another layer of complexity to relaxation dynamics. New pathways are enabled by excited states formed by promoting an electron from a non-bonding (n) or π orbital to a σ^* orbital localised on the C-I bond. These states can be populated either directly through absorption or indirectly via nonadiabatic coupling from the more strongly absorbing $\pi\pi^*$ excited states. In either scenario, photoexcitation is expected to lead to efficient C-I bond fission, similar to that observed in extensively studied alkyl halides [31, 32]. This pathway is expected to compete with the nonadiabatic coupling to the ground state observed for bare thiophene and thiophenone. This is especially true where the initial excitation populates the $\pi\pi^*$ state, as this is where the nonadiabatic couplings will be in direct competition [22–24].

Resonance Raman spectra were also obtained for 2IT following photoexcitaiton at 245.9 nm and 252.7 nm. They showed intensity in regions associated with the C-I stretching mode, consistent with the early stages of C-I bond fission. Additionally, the spectra showed a significant signal associated with several skeletal vibrational modes of the thiophene ring, including C-S bond extension and therefore potential ring-opening. These findings provide the initial evidence that multiple relaxation pathways occur simultaneously [33].

A further resonance-enhanced multiphoton ionisation (REMPI) study was conducted to investigate the dissociation dynamics at play [22]. In this experiment 2IT was excited using various wavelengths in the 220-305 nm range and the total kinetic energy release (TKER) of the iodine atom products was measured. The results showed that iodine atoms were produced in both the ground-state I and the spin-orbit excited I* states at all the investigated excitation wavelengths. The TKER distributions of these iodine products exhibited two distinct components. The first component, which was dominant at longer excitation wavelengths, peaked at TKER values near the maximum allowed by energy conservation rules, indicating that relatively little energy was partitioned into the thiophene ring. These high TKER products were also observed to have anisotropic recoil velocity distributions, described with by a β parameter of 1.7 (where a value of 2 indicates recoil fully parallel with the laser polarisation axis) indicative of prompt dissociation following excitation of a transition dipole moment aligned parallel to the C-I bond [22].

The second component of the TKER distribution, centred at much lower TKER values, showed an isotropic angular distribution and became more prominent at shorter excitation wavelengths, where $\pi \rightarrow \pi^*$ transitions were dominant. Complementary ab initio electronic structure calculations suggested that the slow I/I* products observed at shorter excitation wavelengths might result from C-I bond fission in molecules that have decayed to vibrationally hot levels of the electronic ground state. This coupling to the ground state was suggested to be possible via elongation of the

C-S bond, but whether the hot ground state molecules are mostly ring closed or acyclic at the moment of C-I bond cleavage remained an open question [22].

Initial ultrafast time-resolved studies of 2IT dynamics following 268 nm photoexcitation were performed using transient absorption spectroscopy. Following photoexcitation, the molecule was ionised with wavelengths around the I 4d edge, and the findings have been reported recently along with supporting time-dependent density functional theory (TD-DFT) calculations [24]. This experiment monitored the appearance of features attributable to atomic iodine as the C-I separation increased, reporting a rise time of 160±30 fs [24]. These studies reported no evidence of ring opening or the lower TKER product pathway observed in earlier nanosecond laser experiments. A potential reason for this is that the products of both pathways appear in the same spectroscopic region, making it difficult to isolate and identify the minor, lower TKER product. Additionally, the supporting TD-DFT calculations suggested a negligible cross-section for excitation to $(n/\pi)\sigma^*$ states at 268 nm, and the authors postulated that the photophysics at these wavelengths were dominated by initial $\pi\pi^*$ excitation followed by efficient non-adiabatic coupling to the dissociative $(n/\pi)\sigma^*$ PES.

In summary, the photodissociation dynamics of iodothiophene are governed by the complex interplay of electronic states, with the presence of the iodine atom introducing new relaxation pathways that compete with the intrinsic dynamics of the thiophene ring. The balance between these pathways, influenced by factors such as the excitation wavelength and molecular structure, underscores the intricate nature of the excited-state behaviour of iodothiophene. Further studies, particularly those combining ultrafast spectroscopic techniques with advanced computational methods, will be crucial for unravelling the full scope of these dynamics and their implications for related systems.

1.5 Pump-probe spectroscopy

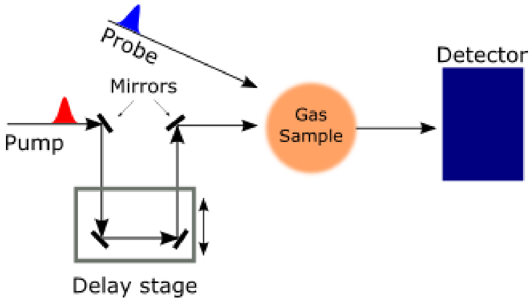

FIGURE 1.5: A schematic representation of a pump-probe experimental set up. The pump and probe pulses intersect within a gaseous sample. A movable delay stage is placed in the path of the pump laser beam in order to control the time delay between the two pulses by varying the beam path length.

Pump-probe spectroscopy is a widely used technique used to investigate the ultrafast photodynamics of molecules. The fundamental principle involves the use of two laser pulses: the pump pulse, which excites the target molecule, and the probe pulse, which is timed to follow the pump pulse by a controlled delay. This delay allows the probe to capture snapshots of the evolving molecular dynamics, essentially freezing moments in time to create a ”movie” of the molecular changes.

A typical experimental setup for pump-probe spectroscopy, as depicted schematically in Figure 1.5, involves a movable stage with two mounted mirrors placed in the path of one of the laser beams and used to change its path length. By altering the path length of this beam, the delay between the pump and probe pulses can be finely tuned, enabling the capture of a series of time-resolved measurements. The time difference between the pump and probe pulses is crucial because it dictates the temporal resolution of the experiment and allows the study of processes such as bond breaking, charge transfer, and molecular rearrangement in real time.

In most photochemical experiments, the pump pulse is typically an ultrashort UV or visible pulse that initiates photodynamics by exciting the molecule from its ground state to an excited electronic state. However, the choice of probe pulse can vary widely, depending on the type of information sought. The probe pulse can be tailored to perform a variety of spectroscopic or scattering experiments, and its characteristics, along with those of the detector and sample delivery system, can be selected based on the specific photophysical or photochemical processes under investigation.

In this thesis, three distinct probing techniques were employed to study the dissociation dynamics of iodothiophene, as discussed in detail in the subsequent sections. Each technique provides unique insights into different aspects of the photodissociation process, from electronic structure changes to atomic-level rearrangements and kinetic energy distributions of fragments.

In Chapter 3, the probe used was designed to ionise the inner-shell electrons of the iodine atom, resulting in the ejection of several electrons from this specific site. This ionisation process leaves behind highly unstable species that can undergo rapid fragmentation. When the molecule is still intact or shortly after photodissociation, the energy from the ionisation can redistribute within the molecule, leading to a Coulomb explosion, where fragments gain additional kinetic energy due to repulsion between like charges. However, if the photodissociating fragments are separated to a critical distance beyond which energy redistribution is no longer possible, the kinetic energy of the fragments will primarily reflect the dissociation pathway that produced them. By analysing the kinetic energies and angular distributions of these fragments as a function of time, detailed information about the dissociation dynamics, such as the timescales and pathways involved, can be inferred.

In Chapter 4, a different approach is adopted using a 14 keV X-ray beam as the probe. This significantly higher energy probe was employed in an X-ray scattering experiment to track the dynamics of a molecule through changes in atomic arrangement. Scattered X-rays provide direct information about the structural evolution of the molecule during and after excitation. By conducting a scattering experiment in a pump-probe configuration, the structural changes induced by the pump pulse can be monitored with high spatial and temporal resolutions. This approach allows the identification of key structural intermediates and determination of whether certain CIs are accessed during the photodissociation process.

Finally, in Chapter 5, a much lower energy probe was utilised in the form of a 22 eV pulse to ionise the valence electrons of 2IT in a time-resolved photoelectron spectroscopy (TRPES) experiment. TRPES is a powerful technique for probing the electronic structures of molecules as they undergo photochemical changes. In this experiment, the probe pulse ejects photoelectrons from the valance shell of the molecule. By analysing the kinetic energy and angular distribution of these photoelectrons, information regarding the transient electronic states and how their populations evolve over time can be obtained. TRPES provides insights into the electronic dynamics that accompany structural changes and offers a complementary perspective to the structural information obtained from X-ray scattering.

These three probing techniques, each with their own strengths and focus, collectively offer a comprehensive picture of the photodissociation dynamics of iodothiophene, revealing the intricate interplay between electronic and structural changes that govern the behaviour of the molecule under excitation.

Chapter 2

Light Sources

2.1 Generating Probe Pulses

The typical ionisation energies of small molecules fall within the range 9-14 eV, corresponding to wavelengths of approximately 90-140 nm [34]. These wavelengths lie in the extreme ultraviolet (XUV) to soft X-ray region of the electromagnetic spectrum, a range that is crucial for probing the electronic structure of molecules through experiments, such as photoelectron spectroscopy. Even higher photon energies are required for experiments such as X-ray diffraction described in Chapter 4 which uses a beam of 14 keV photons.

Traditional methods for generating X-ray radiation, such as X-ray tubes, predominantly produce incoherent radiation with long pulse durations and low brightness [9]. These characteristics render such sources unsuitable for time-resolved studies, where temporal resolution and signal clarity are paramount. The long pulses severely limit the temporal resolution, making it difficult to capture ultrafast processes on a femtosecond timescale. Additionally, the low brightness of these sources results in poor signal-to-noise ratios (SNR), complicating the extraction of meaningful data from experimental noise [10].

Synchrotron radiation sources, which have been widely used in various spectroscopic applications, offer improvements in terms of the pulse duration and bandwidth. Modern synchrotrons can generate pulses with sub-picosecond durations and narrow bandwidths, making them more suitable for time-resolved studies. However, despite these advancements, synchrotrons still suffer from a relatively low peak brightness. This limitation persists as a significant obstacle, particularly when attempting to resolve subtle spectral features or when a high temporal resolution is required. Conventional laser systems with pulse durations as short as 5 fs and exceptionally high brightness have also been employed to study ultrafast dynamics. However, these lasers are generally limited to a narrow spectral range (approximately 0.5-7 eV, which is well below the ionisation energy typically required for probing small molecules). This restriction severely limits their applicability to time-resolved photoelectron spectroscopy in the XUV and soft X-ray regions [10].

To overcome these challenges, two advanced light sources have emerged as solutions: free-electron lasers (FELs) and high-harmonic generation (HHG) sources. Both these technologies have revolutionised the field of time-resolved spectroscopy by providing the necessary temporal resolution, brightness, and spectral coverage.

2.1.1 Free Electron Lasers

A FEL is an advanced source of coherent radiation capable of producing light in the X-ray region with brightness levels that can exceed those of traditional X-ray generation methods by up to a billion times [10]. Additionally, FELs can produce pulses that are thousands of times shorter, making them unparalleled tools for ultrafast time-resolved studies [10].

The journey of FEL technology began with its application at longer wavelengths, with significant progress made by 1998, when lasing at a wavelength of 12 μm was successfully demonstrated [35]. However, the true potential of FELs was realised with their extension into the X-ray region. This breakthrough was first achieved at the FEL facility in Hamburg (FLASH) in 2005, where FELs began generating soft X-rays with photon wavelengths ranging from 89 to 26 nm [36]. These soft X-rays have opened up new possibilities for probing molecular and atomic structures with unprecedented precision.

The evolution of FEL technology continued with a major milestone in 2009, when the Linac Coherent Light Source (LCLS) at the SLAC National Accelerator Laboratory in California became the first facility to generate hard X-rays. The LCLS offered photon wavelengths ranging from 1.2 to 22 nm, extending the capabilities of the FELs into the hard X-ray region [37].

The advent of FELs represents a significant leap forward in the study of chemical dynamics and other fields that require high-brightness, ultrafast X-ray sources. These machines are relatively new tools that have only become available for scientific research in the past two decades. However, their impact has been profound, enabling researchers to capture snapshots of atomic and molecular processes with femtosecond resolution and explore phenomena that were previously inaccessible with conventional light sources. As more FEL facilities come online and existing ones continue to push the limits of wavelength, pulse duration, and brightness, the scope of scientific enquiry they enable will only expand, paving the way for new discoveries in physics, chemistry, biology, and materials sciences.

2.1.1.1 Self-Amplified Spontaneous Emission Free Electron Lasers

Unlike conventional lasers, which rely on electronic transitions between discrete atomic or molecular energy levels, a FEL operates based on the principle of energy exchange between a relativistic electron bunch and an electromagnetic wave within a magnetic structure known as an undulator, depcited in Figure 2.1. This interaction generates a highly coherent and tunable laser beam, making FELs exceptionally versatile tools in the field of high-energy photon science.

To generate the necessary electron bunch, FELs accelerate electrons to near-relativistic speeds, typically in the range 3–15 GeV [38]. This high energy not only compresses the electron bunch by mitigating the effects of electron-electron repulsion, known as space-charge effects, which would otherwise cause the electron bunch to disperse. This is a fundamental difference from conventional laser systems, which depend on the population inversion and stimulated emission of photons within a gain medium.

One of the simplest and most widely used types of FELs is based on the Self-Amplified Spontaneous Emission (SASE) process, which does not require an external light source to initiate lasing [39]. In a SASE FEL, the initial noise—random fluctuations in the electron bunch serve as the seed for generating the laser pulse. The concept of SASE was first proposed by John Madey in 1971 and involves passing the accelerated electron bunch through an undulator, as depicted in Figure 2.1 [40].

The undulator consists of two parallel rows of magnets with alternating poles, creating a periodic magnetic field that forces the electrons to oscillate or ”wiggle” as they traverse the structure. These oscillations cause electrons to emit synchrotron

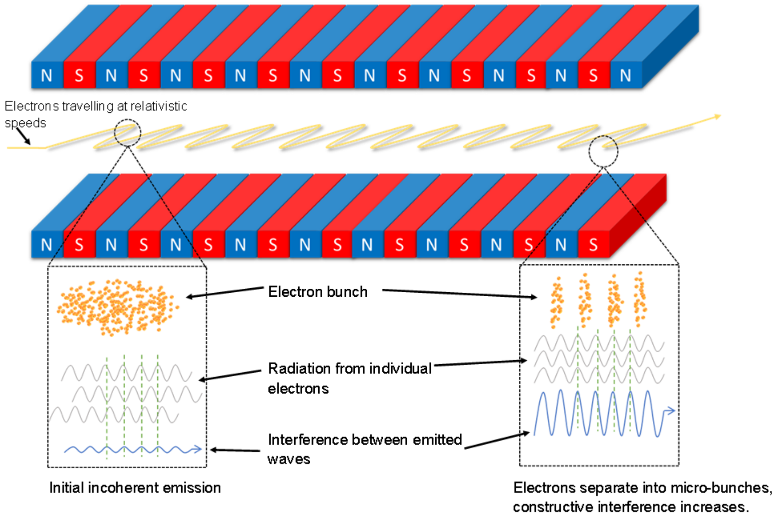

FIGURE 2.1: Schematic representation of an undulator in an FEL set up showing electron bunch separating into micro-bunches as it progresses through the length of the system facilitating coherent emission.

radiation in the form of electromagnetic waves. The key to amplifying this radiation lies in the interaction between the magnetic component of the emitted radiation and electron bunch. Depending on the phase relationship between each electron and the radiation field, the electrons may either gain or lose energy, leading to a process called microbunching [41].

As the electrons become more coherently aligned within these microbunches, the radiation they emit also becomes more in-phase, resulting in a dramatic increase in intensity due to constructive interference. This amplification process is exponential, with the radiation intensity increasing by a factor of up to 10^8 as the electrons travel further along the undulator [39]. Eventually, the intensity asymptotically levels off as the system reaches saturation [42].

A significant advantage of the FELs is their tunability. Because the output wavelength is not determined by fixed atomic energy levels, but by the energy of the electron bunch and the period of the magnetic field in the undulator, FELs can produce a wide range of wavelengths. In particular, SASE FELs can deliver radiation with narrow bandwidths, typically around 0.1% of the photon energy, and pulse lengths as short as a few tens of femtoseconds [43, 44]. Recent advancements have even enabled the generation of pulses in the attosecond domain, opening new possibilities for ultrafast spectroscopy and imaging [45].

However, the SASE process has several limitations. Because they rely on spontaneous emission, SASE FELs can exhibit significant shot-to-shot variations in both photon energy and intensity, leading to poor reproducibility. Furthermore, the noisy startup process associated with spontaneous emission results in a lack of longitudinal coherence, implying that the phases of the emitted light waves do not align consistently over the pulse duration. This necessitates the measurement of the characteristics of each pulse, which are then used to correct for these variations during the data analysis [46].

2.1.1.2 Seeded Free Electron Lasers

The inherent challenges posed by SASE radiation in FELs have driven researchers to explore a variety of strategies to enhance the stability, coherence, and overall performance of these advanced light sources. SASE, while enabling the generation of high-intensity radiation lacks predictability on shot-to-shot basis. This unpredictability of the output radiation can limit the precision and utility of FELs in applications which require high spectral purity and temporal stability.

One of the most promising approaches to overcome these limitations is seeding, in which an external laser pulse is introduced to interact with the electron bunch before it enters the undulator. This interaction effectively pre-conditions the electron bunch, initiating the micro-bunching process, and aims to introduce coherent modulation onto the electron bunch before it enters the undulator. The resulting radiation is synchronized with the seed laser. By imprinting coherent modulation on the electron beam, seeding can significantly reduce the noise and enhance the reproducibility of the FEL output, resulting in significantly improved spectral purity and temporal stability [47, 48].

There are two primary mechanisms for seeding FELs: external seeding and self-seeding. Both methods share the goal of enhancing the coherence of the FEL output, but differ in their approaches and technical challenges. In an external seeding scenario, a precisely tuned laser pulse is introduced to interact with the electron bunch before it enters the undulator [36, 49, 50]. In a self-seeding setup, the FEL system is divided into two stages, each with its own undulator. The first undulator operates in the traditional SASE mode, generating broad band, incoherent radiation that contains a wide range of wavelengths. These are filtered and used as the seeding pulse for the second undulator stage [51–53].

2.1.2 Current state-of-the-art

X-ray free-electron lasers (XFELs) have fundamentally transformed the landscape of scientific research by offering previously unattainable capabilities for generating ultra-bright coherent X-ray pulses. Since the early 2000s, XFELs have emerged as indispensable tools for studying phenomena at the atomic and molecular levels owing to their ability to produce exceptionally intense and brief bursts of X-rays. In 2024, eight XFEL facilities are in user operation worldwide, distributed across Europe, North America, and Asia. They are FLASH [54] and European XFEL [55] in Germany, LCLS [37] in the USA, SACLA [56] in Japan, FERMI [57] in Italy, PAL-XFEL [58] in South Korea, SXFEL [59] in China, and SwissFEL [60] in Switzerland.

These facilities span a broad range of operational capabilities, with some specialising in soft X-rays and others extending into the hard X-ray regime, thus allowing researchers to probe matter with unprecedented precision. The European XFEL and LCLS-II, for example, can produce hard X-rays down to wavelengths as short as 1.5 Å (0.15 nm), making them invaluable for high-resolution imaging and diffraction studies [61, 62]. In addition, the pulse structures and repetition rates of these facilities vary significantly. Older XFELs, such as the LCLS and SACLA, typically operate at repetition rates of approximately 100 Hz [37, 56]. In contrast, more recent installations, such as the European XFEL and the LCLS-II upgrade, are designed to operate at MHz-level repetition rates, representing a significant leap in data-acquisition efficiency [55, 62]. The higher repetition rates of these newer XFELs enable experiments that require large datasets or increased temporal resolution, particularly in ultrafast time-resolved studies, where multiple snapshots of dynamic processes are captured within a short time window.

Most of these XFELs utilise SASE as their primary operating principle. with the exception of facilities, such as FERMI in Italy and SXFEL in China [57, 59]. Laser-based external seeding has been implemented to achieve better control over the pulse properties. These seeding techniques rely on an external laser pulse to initiate the amplification process, leading to X-ray pulses with a significantly higher longitudinal coherence than those produced via SASE alone. However, laser-based seeding is currently limited to relatively low photon energies, typically up to approximately 400 eV, which restricts these facilities to soft X-ray experiments. LCLS and European XFEL have incorporated self-seeding schemes, and ongoing research is focused on refining this approach to maximise pulse stability and photon flux [37, 55, 62].

While new facilities are being built, existing facilities are also undergoing significant upgrades to remain at the forefront of the XFEL technology. At the European XFEL, upgrades to the undulator systems and improvements in beamline optics are expected to boost both the brightness and stability of the X-ray pulses [55]. Meanwhile, the Athos beamline at SwissFEL pioneered the use of novel undulator layouts, such as transverse-gradient undulators, to provide more precise control over FEL properties, enabling experiments that require fine-tuning of X-ray polarisation or pulse shape [60]. The ongoing development of XFELs not only promises to address existing challenges in photon science, but also opens the door to new research directions. Facilities such as LCLS-II and SHINE have come online, and seeding techniques continue to mature [62, 63].

2.1.3 High Harmonic Generation

While FELs offer several critical advantages, such as generating bright, ultrafast, and tunable XUV pulses, one of their most significant limitations is accessibility. FEL facilities are not only expensive to construct and maintain but also require a highly specialised workforce to operate. These facilities are often large-scale national or international collaborations that make them available to a limited number of research groups. Consequently, access to FELs is competitive and highly regulated, with researchers needing to submit proposals for beam time, which is typically granted for only short, fixed periods. This logistical constraint, combined with high operational costs, significantly limits the widespread use of FELs for experimental research in the broader scientific community.

To address the limitations of accessibility posed by FELs, a promising alternative is the use of HHG sources, which can be implemented in standard laboratory environments. Unlike FELs, HHG-based systems can generate XUV and soft X-ray pulses on a

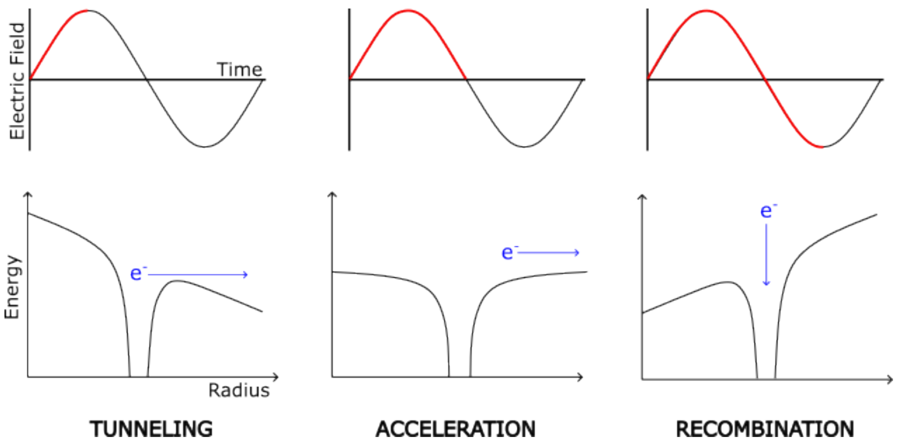

FIGURE 2.2: The three step model of a HHG process. The point of the laser electric field at each step is marked in red, below are the resulting shape of the atomic PES and the position of the electron.

tabletop scale, thereby providing an affordable and scalable solution for time-resolved studies. Although HHG sources generally deliver lower photon flux and energy than FELs, their ability to produce ultrashort coherent light pulses in the XUV range makes them a strong alternative [64].

HHG is a nonlinear optical process in which a femtosecond laser pulse is focused into a medium, typically a noble gas, such as argon or neon. The interaction between the intense laser field and gas results in the emission of light at frequencies that are odd integer multiples (harmonics) of the fundamental input frequency. This process enables the generation of coherent XUV and soft X-ray radiation using a relatively simple laboratory setup.

The HHG mechanism can be understood through the widely accepted ”three-step model” (illustrated in Figure 2.2), which describes the interaction between the laser field and atom as follows [65]:

1. Tunnelling: When the laser’s electric field reaches a magnitude comparable to the atomic field, it distorts the Coulomb potential of the atom, allowing the electron to escape via quantum mechanical tunnelling. This process requires an intense laser field, typically in the range of 10^{13} to 10^{15} W/cm^2. The electron does not gain sufficient energy to fully ionise in a classical sense, but rather tunnels through the barrier created by the laser field.
2. Acceleration: Once an electron escapes the atomic potential, it is accelerated by the oscillating electric field of the laser. Initially, the electron is driven away from the nucleus, but as the laser field changes direction (owing to its oscillatory nature), the electron is pulled back towards the parent ion. This acceleration phase is crucial because the kinetic energy acquired by an electron is directly related to the energy of the emitted high harmonic photons.

3. Recombination: The third step occurs when the returning electron recombines with its parent ion. Upon recombination, the electron releases excess kinetic energy in the form of a photon. The energy of this photon corresponds to the high harmonic of the laser frequency. For this step to be successful, the laser should be polarised linearly, as opposed to circularly, so that the electron returns to the molecule.

The temporal characteristics of the generated harmonics are directly related to the dynamics of the laser field, resulting in extremely short pulse durations. HHG can produce femtosecond pulses, and in some cases, even attosecond pulses (1 attosecond = 10^{-18} seconds), making it a powerful tool for ultrafast spectroscopy [66].

In the HHG process, there are multiple electron trajectories which can lead to the recombination and emission of harmonic radiation. These different electron trajectories arise because of the oscillatory nature of the driving laser field, which influences the energy and path of ionised electrons. Depending on the exact timing of ionisation and subsequent acceleration, electrons follow either short or long trajectories before recombining with the parent ion. Each of these trajectories results in a different kinetic energy at the point of recombination, leading to the emission of photons with varying energies across the high-harmonic spectrum. The average energy that the electron accumulates from the oscillating electric field of the laser is known as the ponderomotive potential, U_p: [64, 65]

$$U_p = \frac{e^2 E^2}{4 m_e \omega^2} \tag{2.1}$$

where e is the electronic charge, E is the strength of the laser field, m_e is the mass of the electron, and ω is the laser frequency. The ponderomotive potential plays a crucial role in determining the cutoff energy of harmonics generated in the HHG process. The maximum photon energy energy a photon can gain is $3.17U_p$. Therefore there is also a cutoff energy for the possible harmonics, E_{max}, which is given approximately by the equation [64, 65]:

$$E_{max} = 3.17 U_p + I_p \tag{2.2}$$

where I_p is the ionisation potential of the medium used. Equations 2.1.3 and 2.1.3 highlight that increasing the laser intensity allows the electron to gain more kinetic energy, which, in turn, leads to the generation of higher-energy harmonics. The harmonic spectrum and energy of the emitted photons can be controlled by adjusting the laser intensity or wavelength. This tunability is a key advantage of HHG in laboratory-based ultrafast spectroscopy.

While solids such as dielectric crystals and liquids such as water or benzene have been used to generate harmonics, noble gases such as argon, neon, and xenon are most often used as the medium for HHG. This is particularly because of their relatively high ionisation potentials. A high ionisation potential is crucial because it contributes to a larger maximum possible harmonic energy as per Equation 2.1.3. The cutoff energy for HHG is determined by both the ponderomotive potential and ionisation potential of the medium, gases with higher ionisation potentials allow for the generation of higher-energy photons at the cutoff. This makes noble gases particularly suitable for producing high harmonics in extreme XUV or soft X-ray regions.

Moreover, the ponderomotive potential depends on the laser frequency, meaning that a lower-frequency driving laser (such as in the infrared range) will result in a higher cutoff energy. This is because the ponderomotive potential increases as the laser wavelength increases (or as the frequency decreases), allowing electrons to gain more energy before recombination. However, this benefit comes with a tradeoff. A lower-frequency driving laser also implies that the electron spends a longer time outside the potential well of the atom after tunnelling. During this time, the electronic wavepacket spreads out, reducing the likelihood of recombination with the parent ion. As a result, while a lower-frequency laser can generate higher cutoff harmonics, it can also lead to a reduced recombination probability and, consequently, a lower overall harmonic yield.

On the other hand, using a higher-frequency laser (shorter wavelength) generally results in a higher intensity of the generated harmonics, provided that the photon energy is below the cutoff. This is because the electron wavepacket experiences less temporal spreading, leading to a higher recombination probability. Thus, there is a balance between selecting the appropriate laser frequency to maximise harmonic yield and photon energy.

An important consideration in HHG is the phenomenon of phase matching, which significantly affects the efficiency and intensity of the generated harmonics. For optimal harmonic generation, the electric field of each newly generated harmonic must remain in phase with the fields of harmonics that have already been produced. This condition leads to constructive interference that enhances the overall harmonic intensity. Conversely, any phase mismatch between these fields results in destructive interference, which can impede the propagation and efficiency of generated harmonics.

There are four key contributions to the phase mismatch in HHG:

- Atomic Phase Shift: This phase shift arises owing to the time delay between the tunnelling ionisation of the electron and its subsequent recombination with the parent ion. During this delay, the phase of the laser field may change, resulting in a phase difference between harmonics generated at different times.
- Neutral Atom Effect: A phase mismatch also occurs because of the different refractive indices of the fundamental and harmonic frequencies in the gas medium. The refractive index is frequency dependent, causing different phase velocities for fundamental and harmonic light waves. The gas pressure influences its refractive index; thus, adjusting the pressure can help optimise phase matching.
- Free Electron Effect: When the gas is ionised, it creates a plasma consisting of free electrons. The refractive index of plasma affects the phase velocity of the fundamental laser field. Although this effect has a more pronounced impact on the fundamental frequency, its influence on harmonics is relatively minor. The free-electron effect can therefore introduce phase mismatches that affect the harmonic yield, but its impact is generally less significant compared to other contributions.
- Geometric Effect (Gouy Phase Shift): The Gouy phase shift arises as the Gaussian laser beam passes through its focus. This phase shift is described by the function $\phi_G(z) = -arctan\left(\frac{z}{z_R}\right)$, where $z_R$is the Rayleigh length of the beam, and z is the distance from the beam waist. Because the Rayleigh length is inversely proportional to the laser wavelength, the fundamental beam is affected more strongly by this phase shift than the higher harmonics. Consequently, the position of the gas cell relative to the beam focus influences the phase matching.

While attempts have been made to model and describe the varying effects, in an experiment they are all very strongly coupled. This means an approach where the controllable parameters are scanned and optimal conditions for a given harmonic of interested are found is usually taken.

2.2 Generating Pump Pulses

2.2.1 Ti:Sapphire Lasers

Generating the pump wavelengths used in the experiments described in this thesis starts with an 800 nm beam of photons produced by a widely adopted Ti:Sapphire laser system. In order to achieve the desired pump wavelength (in the range of 245-262 nm in the experiments designed in this thesis) further non-linear methods are employed.

2.2.2 Non-linear Crystals

Non-linear crystals (NCLs) can be used to generate higher energy photons from the initial 800 nm laser beam. A non-linear crystal is one whose response to incident light does not have a linear dependence on the field strength of the light. An example of such material is commonly used crystalline barium borate (BBO).

When placed in a laser field, the electron distribution of material is distorted creating oscillating dipoles, in those oscillations charge is being accelerated, and therefore light is emitted with the same frequency as the driven oscillations. The dipole moment per unit volume is known as polarization, P, given by:

$$P(t) = \epsilon_0(\chi^{(1)}E(t) + \chi^{(2)}E^2(t) + \chi^{(3)}E^3(t) + [...] + \chi^{(n)}E^n(t)) \tag{2.3}$$

where ϵ_0 is the permittivity of vacuum, E is the electric field of the light and $\chi^{(n)}$ is the nth-order electric susceptibility.

When the laser intensity is low, only the first term of the expansion shows any significant contribution however at high intensities higher order contributions become important.

The electric field of the light with frequency ω may be expressed as:

$$E(t) = E_\omega e^{i\omega t} \tag{2.4}$$

where E_ω is the amplitude and ω is the frequency. Substituting equation 2.4 into equation 2.3 therefore gives:

$$P = \epsilon_0(\chi^{(1)}E_\omega e^{i\omega t} + \chi^{(2)}E_\omega e^{i2\omega t} + \chi^{(3)}E_\omega e^{i3\omega t} + [...] + \chi^{(n)}E_\omega e^{in\omega t}) \tag{2.5}$$

As higher-order terms become significant, emission of light with new frequencies (2ω, 3ω, etc.) becomes possible. When this method is used to obtain the second harmonic of the input wavelength it is known as second harmonic generation (SHG).

Alternatively two different frequencies of light may be incident on the material. In this case the electric field becomes:

$$E(t) = [E_{\omega_1} e^{i\omega_1 t} + E_{\omega_2} e^{i\omega_2 t}] \tag{2.6}$$

where ω_i is used to describe the frequency of the ith wave. Following this the second-order polarization component becomes:

$$\begin{aligned} P^{(2)} &= \epsilon_0 \chi^{(2)} [E_{\omega_1} e^{i\omega_1 t} + E_{\omega_2} e^{i\omega_2 t}]^2 \\ &= \epsilon_0 \chi^{(2)} [E_{\omega_1}^2 e^{i2\omega_1 t} + 2E_{\omega_1} E_{\omega_2} e^{i(\omega_1+\omega_2)t} + E_{\omega_2}^2 e^{i2\omega_2 t}] \end{aligned} \tag{2.7}$$

where the term containing $(\omega_1 + \omega_2)$ describes the emission of light with that frequency. This is called sum frequency generation (SFG).

It should be noted that in order to observe efficient frequency generation the input and out phase must be phase matched in order for them to interfere constructively. The phase of a wave is described using a wave vector given by:

$$k = \frac{\omega n(\omega)}{c} \tag{2.8}$$

where ω is the frequency of light, $n(\omega)$ is the refractive index of the material for light with frequency ω and c is the speed of light in vacuum. In order for wavelengths to be emitted:

$$k_3 = k_1 + k_2 \tag{2.9}$$

In most materials the refractive index increases with frequency and therefore phase matching cannot be achieved. Birefringent material (such as BBO) however have different refractive indices along different axis making phase matching possible. In type-1 nonlinear crystals, such as BBO, the polarisation of the generated light is perpendicular to that of the incident light. Simple adjustment of the angle of the crystal changes the refractive index experienced by the different frequencies allowing for the phase matching condition to be met.

2.2.3 Optical Parametric Amplifiers

Another method of generating pump wavelengths from the 800 nm output of the Ti:Sappfire laser system is using an optical parametric amplifier (OPA). An OPA is a nonlinear optical device used to amplify light and generate tunable wavelengths over a broad spectral range. OPAs operate based on the principle of parametric amplification, which involves the interaction of a strong pump beam with a nonlinear crystal to produce two new beams: a signal and an idler. The process is governed by energy and momentum conservation, often referred to as phase-matching conditions, within the nonlinear medium.

The operation of an OPA begins with the input of a high-intensity pump laser which provides the necessary energy to drive the nonlinear process. The pump beam, with frequency ω_p, interacts with a nonlinear crystal, such as BBO or lithium triborate (LBO), where three-wave mixing occurs. In this process, the pump photon is "split" into two lower-energy photons: one at the signal wavelength and one at the idler wavelength with frequencies ω_s and ω_i, respectively. Due to the energy conservation rules their energies/frequencies are related by the following:

$$\omega_i = \omega_p - \omega_s \tag{2.10}$$

This means that the energy of the pump photon is distributed between the signal and idler photons. The signal photon is typically the desired output, while the idler photon carries the remainder of the energy. Phase-matching is achieved by carefully selecting the angle and orientation of the nonlinear crystal relative to the incoming pump beam.

An OPA generally requires a weak seed pulse at the signal wavelength to begin the amplification process. This seed pulse can originate from spontaneous parametric down-conversion or from another optical source. When the seed pulse enters the nonlinear crystal along with the intense pump beam, the energy from the pump is transferred to the seed pulse, amplifying it to much higher intensities.

As the seed signal beam is amplified, the idler beam is also generated to conserve energy. Both the signal and idler beams emerge from the crystal with increased intensities, but the signal beam is typically used as the desired output due to its tunability and coherence. One of the key advantages of an OPA is its ability to produce tunable output wavelengths. By adjusting the phase-matching conditions, the signal and idler wavelengths can be varied across a broad spectral range, from the ultraviolet to the infrared. The wavelength tuning can be achieved by changing the angle of the nonlinear crystal, varying the pump wavelength, or using different nonlinear materials.

The experiments described in the subsequent chapters make use of either OPAs or NLCs to generate the pump wavelength which is then combined with a specific probe. The specific arrangement used in each case is described in more detail respective chapters.

2.2.4 Data analysis

The following chapters of the thesis present the results acquired using three different experimental methods. In each case raw data was created at the respective facilities, this necessitated advanced data processing and analysis approaches. These were created, optimised and streamlined uniquely for each experimental dataset by me with a mixture of wholly new approaches as well as development and extension of previously applied techniques. A number of programming languages were used in this process including LabView, MATLAB and (predominately) Python. The precise details of the data analysis approaches varied between the experimental techniques so are described in each of the three results chapters individually.

Chapter 3

Time-resolved Coulomb Explosion Imaging Study of Iodothiophene Dissociation Dynamics

This Chapter is based on work published in paper titled: *Exploring the Ultrafast and Isomer-Dependent Photodissociation of Iodothiophenes via Site-Selective Ionization* by Weronika O. Razmus, Felix Allum, James Harries, Yoshiaki Kumagai, Kiyonobu Nagaya, Surjendu Bhattacharyya, Matthew Britton, Matthew Brouard, Phillip H. Bucksbaum, Kieran Cheung, Stuart W. Crane, Mizuho Fushitani, Ian Gabalski, Tatsuo Gejo, Aaron Ghrist, David Heathcote, Yasumasa Hikosaka, Akiyoshi Hishikawa, Paul Hockett, Ellen Jones, Edwin Kukk, Hiroshi Iwayama, Huynh V.S. Lam, Joseph W. McManus, Dennis Milesevic, Jochen Mikosh, Shinichirou Minemoto, Akinobu Niozu, Andrew J. Orr-Ewing, Shigeki Owada, Daniel Rolles, Artem Rudenko, Dave Townsend, Kiyoshi Ueda, James Unwin, Claire Vallance, Anbu Venkatachalam, Shin-ichi Wada, Tiffany Walmsley, Emiliy M. Warne, Joanne L. Woodhouse, Michael Burt, Michael N.R. Ashfold, Russell S. Minns and Ruaridh Forbes.

RF conceived the experiment, the plan for which benefited from further input from FA, MA, JH, RM and KN. The sample delivery and spectrometer were prepared by JH and KN, YK arranged the data acquisition software and SO prepared the beamline. The experiment was conducted onsite by MF, TG, JH, YH, AH, HI, YK, SM, KN and AN with online participation in the experiment by all authors. The data acquisition software was constructed by YK. The experiment was analysed by WR with support from FA. Finally, FA, MA, RF, RM, and WR interpreted the results and wrote the manuscript with input from all the authors. Figures 3.3, 3.5, 3.6, 3.12, and 3.13 are also published in the paper.

3.1 Introduction

Inner-shell ionisation studies have proven to be a highly effective method for investigating photoinduced processes in molecular systems [67–73]. The exceptional capabilities of free-electron lasers (FELs) make it possible to remove inner-shell electrons from a specific site in molecules, the iodine in 2- and 3-iodothiophene (2IT and 3IT), in an ultrafast time-resolved experiment. The appearance time and momentum of the resulting fragments is directly linked to the relaxation pathways they arise from.

The data collected in the experiment described in this chapter has certain similarities with earlier resonance enchanced multiphoton ionisation (REMPI) studies [74–76] as both datasets directly measure the energy of the photofragments created through photodissociation. In the experiment described in this chapter, the signal associated with neutral dissociation can be detected once the inter-fragment distance surpasses a critical distance, and charge transfer between species is no longer allowed. REMPI approaches are also insensitive to detecting neutral dissociation products at the start of bond fission process. In order to satisfy the necessary resonance conditions for detecting the products, the fragment separation must exceed the range of neutral bonding interactions. Although REMPI probing has the potential to provide quantum state specificity, the detection efficiencies are also quantum state dependent, effectively preventing the quantification of product branching ratios. Inner-shell ionisation affects all quantum states of the target site and can result in a more complex and overlapping spectrum, but also presents more opportunities for determining branching ratios when spatial components can be resolved.

Previous literature on the photolysis of 2IT has been introduced in Chapter 1. However, due to the similarities between REMPI and inner-shell ionisation probing, specific attention should be given to the previous REMPI study of 2IT [22]. This study utilised a nanosecond laser and exciation wavelengths ranging from 220-305 nm in conjunction with VMI detection methods. The measurements yielded kinetic energy (KE) information of both I and I* photoproducts, allowing comparisons to be made between the current and previously reported data. The study revealed a two-component total KE release (TKER) distribution. The channel dominant at longer wavelengths peaks close to the maximum available energy allowed by conservation rules with anisotropic recoil velocity distributions. The minor component is centered at much lower TKER values and displays an isotropic velocity distribution. The same trends are observed in the current data and their implications are discussed further in Section 2.4. This chapter's experiment sought to exploit the site-selective properties of XUV-induced ionisation to quantify the time scales associated with the two competing dissociation processes identified in previous nanosecond studies and to explore how these vary depending on the iodine position on the ring.

3.1.1 Principles of Inner-Shell Ionisation

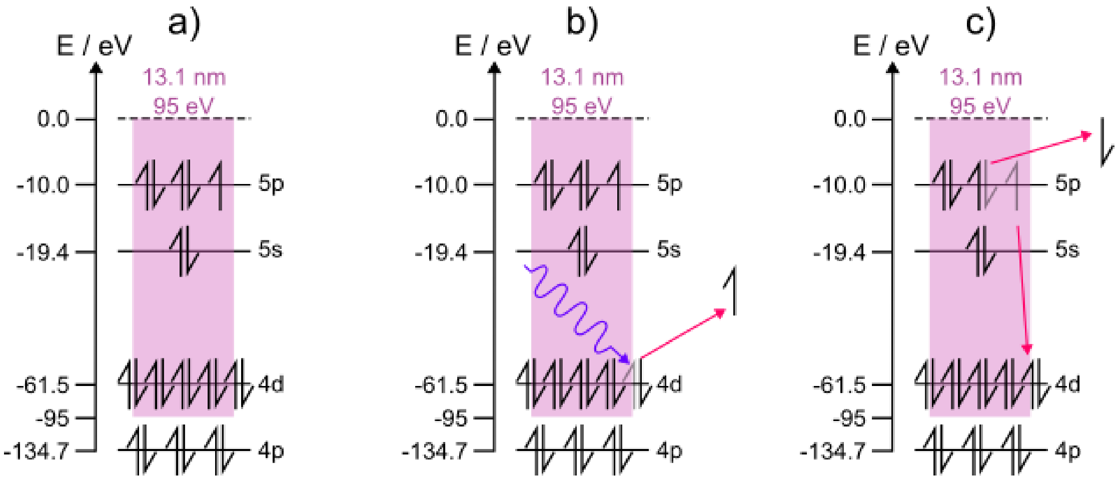

FIGURE 3.1: The energy scheme of the four highest occupied atomic orbitals of iodine Panel a) highlights in purple the orbitals which are energetically accessible with a 95 eV photon. Panel b) shows the creation of a core hole by ionising an electron from the 4d orbital following absorption of the 95 eV photon. Panel c) depicts the Auger-Meitner decay mechanism which sees the core hole filled by a higher lying electron leading to the ejection of a secondary electron from the same orbital.

In the experiment presented in this chapter, the ionisation process was initiated by tuning the FEL energy to maximise the ionisation of the 4d shell of iodine. This results in the creation of core-holes that are filled by rapid Auger-Meitner decay. This decay process, depicted in Figure 3.1, may involve the ejection of additional electrons, leading to the formation of multiply charged ions [77, 78].

To achieve core ionisation, the photon energy must exceed the binding energy of the core electron. A FEL is a unique tool capable of generating laser pulses with the necessary energy and short pulse duration on the femtosecond scale, making it suitable for studying ultrafast processes using inner-shell ionization.

	Iodine	Carbon	Sulfur	Hydrogen
$\sigma_{tot}(Mb)$	9.38	0.61	0.83	0.02
$\sigma_{rel}(Mb)$	1	0.26	0.09	0.006

TABLE 3.1: Calculated total atomic absorption cross section, σ_{tot}, and relative cross sections,σ_{rel}, for photoionisation of all atoms in iodothiophene at the photon energy of 95 eV. Data taken from [79].

In order for the experiment to provide valuable insight into the site-specific changes the atomic absorption cross sections for photoionisation, σ_{abs}, must be dominant at the targeted site. The photon energy used in the experiment described in this chapter was 95 eV (13.1 nm). The calculated total (for all accessible orbitals) atomic photoionisation cross sections, σ_{tot}, for a 95 eV photon across all atoms present in iodothiophene are shown in Table 3.1[79]. Additionally, the absorption cross-section values are multiplied by the number of instances of each atom present, which gives the relative absorption cross-section, σ_{rel}. A relative value for absorption corrects for the increased probability of absorbing a photon at one of the multiple instances of an atom. This is presented as a ratio in Table 3.1. The values clearly show that an iodine atom is ~ 11 times more likely to absorb a 95 eV photon than any other atom in the molecule and that overall, the photon is $\sim$4 times more likely to remove an electron from iodine than anywhere else in the molecule.

	4d	5s	5p
$\sigma_{abs}(Mb)$	9.10	0.13	0.14

TABLE 3.2: Calculated atomic absorption cross section, σ_{abs}, for all energetically accessible iodine orbitals at 95 eV. Data taken from [79]

Similarly, the specific atomic orbital from which the electron is ejected can be determined by examining the calculated absorption cross sections for the accessible orbitals. These are shown in Table 3.2. Atomic orbitals which are not energetically accessible at this photon energy were omitted as electrons cannot be ejected from them. From these data, it can be deduced that ionisation occurs predominantly from the I 4d orbital as the cross section is ~ 70 times larger than for any other orbital. A 4d electron is more strongly bound than other electrons. More strongly bound electrons that are not involved in molecular bonding are typically the best targets for inner-shell ionisation.

In summary, irradiation with 95 eV electrons is expected to preferentially produce a localised hole in the I(4d) orbital. This is illustrated in panel b) of Figure 3.1. Following ionisation, the dissipation of energy and filling of the core vacancies can occur via radiative or non-radiative processes.

Fluorescence decay is a typical radiative relaxation process in which the hole is filled by a higher-lying electron, leading to the emission of a photon. The emitted photon has an energy (E_{hv}) that is characteristic of the energy difference between the initial (E_1) and final (E_2) energies of the atomic orbitals occupied by the electron before and after filling the core-hole.

$$E_{hv} = E_1 - E_2 \tag{3.1}$$

In this instance, the charge of the atom remains constant and charged fragments are not formed. Consequently, fluorescence decay is not a relevant topic for discussion in this chapter.

Auger decay presents a non-radiative alternative in which core-holes can be filled. The removal of a core electron causes an electron from a higher-lying state (with binding energy, E_3) to transition to the 4d orbital to fill the vacancy. The excess energy is then carried away by a second electron, referred to as the Auger electron, in the form of KE (E_{KE}) given by:

$$E_{KE} = E_1 - E_2 - E_3 \tag{3.2}$$

This process is depicted in panel c) of Figure 3.1. The end result is that there are two vacancies in the outer shell of the ion, leading to an increase in its charge by one. The initial Auger-Meitner decay may result in a molecular dication trapped in an excited state, which could subsequently undergo a second Auger decay as part of an Auger cascade.

Alternatively, a second 95 eV photon has the potential to remove the electron that has filled the inner shell, also causing a second Auger decay. Comparison with synchotoron measurements of single-photon ionisation of Xe, which is isoelectronic with I^- and thus likely exhibits similar Auger-Meitner decay pathways, suggests that ionisation with a single 95 eV photon produces charge states below 3+. The highest yield is observed for ions in the 2+ charge state [78].

3.1.1.1 Charge Transfer in pump-probe measurements

If the molecule has not dissociated at the time of inner-shell ionisation, the charge can be quickly redistributed around the system (especially an aromatic one), leading to a highly unstable polycation. This species experiences intense intramolecular Coulombic repulsions. The chemical bonds within the molecule are significantly weakened, thereby decreasing their binding energy. The repulsive forces that arise between the fragments surpass this energy, leading to molecular fragmentation known as Coulomb explosion (CE) [80–82].

However, when 2IT is exposed to UV radiation prior to the FEL photons, photodissociation will produce two neutral fragments. Charge redistribution, leading to classical CE, shows a strong distance dependence and prevails when the dissociating fragments are at sufficiently low separations. This dependence has been investigated and reliably described using a classical over-the-barrier (OBT) model [67, 69–73]. This model states that charge may be transferred if the Coulombic barrier to electron transfer is lower than the ionisation energy of the site ”donating” the electron. The magnitude of this barrier increases with the intermolecular separation. The distance past which charge transfer (CT) is forbidden is known as the critical distance (R_{crit}) and is given, in atomic units, by:

$$R_{crit}(q) = \frac{(p+1) + 2\sqrt{(p+1)q}}{E_i} \tag{3.3}$$

where p and q are the charges of the two fragments, and E_i is the ionisation energy of the radical co-fragment. In this experiment the radical co-fragment is assumed to remain neutral, that is, its charge is zero (p = 0). This simplifies Equation 3.3 to:

$$R_{crit}(q) = \frac{1 + 2\sqrt{q}}{E_i} \tag{3.4}$$

Where q is the charge of the iodine atom fragment.

At early pump-probe delays, where the separation between the fragments is less than R_{crit}, CT may lead to the formation of two charged fragments. These fragments then repel each other, increasing their KE. Inversely, once a separation greater than R_{crit} is achieved, CT cannot occur. This is characterised by the appearance of iodine products with low kinetic energies which remain constant. The low KE features and their temporal profiles, thus, encode information solely of the neutral UV photodissociation. This behavior was previously observed for example in photolysis of CH_3I [67]. Absorption of a 201.2 nm photon led to photodissociation into a CH_3 radical and I atom. The characteristic low and constant KE feature was observed 30 fs after time zero in the case of I^{2+} fragments. A steady increase in appearance time was observed for iodine fragments in higher charge states consistent with the values calculated using the OBT model with I^{6+} ions appearing 100 fs after I^{2+} was observed.

3.2 Experimental details

The specifics of the experimental apparatus used in this Chapter are introduced in Chapter 2. The objective of this section is to outline the primary parameters used in the experiment presented in this Chapter.

The experiment was performed at the eXtreme UltraViolet (XUV) beamline (BL1) of Spring-8 Angstrom Compact free electron LAser (SACLA) in Japan [83]. XUV pulses were generated at a repetition rate of 60 Hz, with an estimated duration of $\sim$ 35 fs and an energy of 95 eV (13.1 nm) [84]. A 0.5 μm thick Zr filter was used to attenuate the XUV pulse prior to focusing to a spot size of $\sim$ 10 μm at the interaction point. The shot-to-shot XUV pulse energies were measured upstream of the interaction region by using a gas intensity monitor, with a recorded mean value of 30 μJ [85]. The expected transmissions of the beamline and Zr filter are $\approx$ 90% and $\approx$ 19%, respectively. Using these values, the estimated on-target energy is 5.1 μJ with a peak intensity of $\sim 4.4x10^{14}$ W/cm^2.

The generation of UV pump pulses (261.5 nm) was achieved by frequency tripling the output of the BL1 optical laser system. This system comprised a Ti:sapphire oscillator, a chirped-pulse regenerative amplifier, and a home-built multipass amplifier [83].

Prior to the frequency tripling, the fundamental signal was attenuated using a variable neutral density filter in order to attain UV pulse energies of approximately 2 μJ. The resulting UV pulses were then focused and directed towards the interaction using a 2-metre focusing lens.

The UV and XUV pulses were overlapped in a near-collinear geometry using a right-angled prism. The time delay between the UV and XUV pulses was controlled using a motorised delay stage. The pump-probe delays were systematically scanned from -2 to 6 ps in variable step sizes. The initial time zero was estimated, during the experiment, based on the appearance of low KE pump-probe features in the data and refined later, as described in Section 3.3.3. The time jitter between the two pulses was measured, on a shot-to-shot basis, using an arrival time monitor [86].

Room-temperature 2IT and 3IT molecules were expanded using a pulsed General Valve without a seed gas. The molecular beam was skimmed before entering the chamber, where it crossed the UV and XUV laser pulses at an angle of $\sim$ 45 degrees.

The generated ions were accelerated by a series of electrodes under VMI conditions onto a time- and position-sensitive detector comprising dual MicroChannel Plates (MCPs) and a hexanode delay line [87, 88]. Due to the random orientation of molecules in the gas phase, photofragments released with the same recoil veolcity form a sphere around the interaction region. The radius of this sphere is dependent on the KE and time-delay following dissociation. In VMI conditions a series of electrodes is used to accelerate the photofragments of intrest towards a 2D detector in such a way that each particle with the same velocity vector is mapped onto the same point on the detector regardless of their differing points of origin. The result is an image containing concentric rings, corresponding to different momenta. The arrival times (τ) and hit positions (x, y) of the photofragments were recorded. The values of x, y, and τ for ions hitting the detector obtained in this experiment were converted into momentum through ion trajectory simulations conducted using the SIMION 8.1 software package by collaborator Felix Allum.

3.3 Data Treatment

3.3.1 FEL flutations

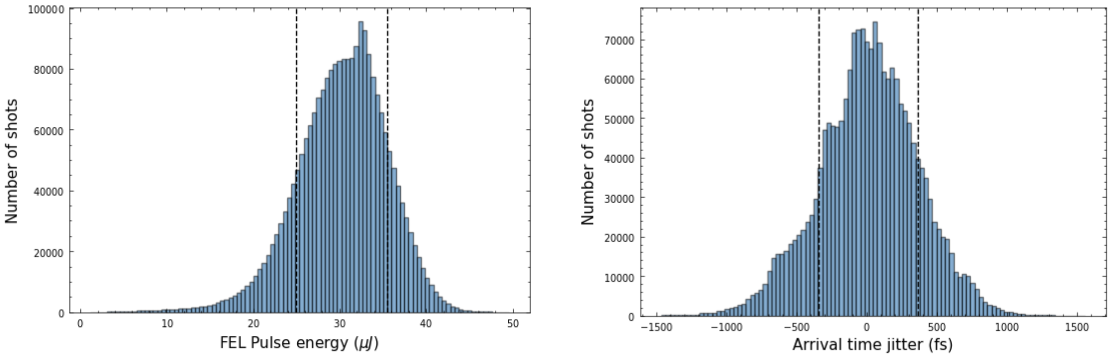

(A) (B)

FIGURE 3.2: A histogram of A) FEL pulse power and B) FEL arrival time jitter of all shots recorded as part of the analysed dataset. Dashed vertical lines mark the subset of data carried forward for analysis.

The inherent fluctuations in the FEL pulse energy and arrival time have a negative effect on the temporal resolution of the experiment and potentially lead to intensity artefacts. The first step in the data treatment process is to use the collected metadata to correct these issues.

The histograms of FEL pulse energy and timing jitter for all shots collected during the experiments are shown in Figure 3.2 A) and 3.2 B), respectively. Shots were discarded where the values of the parameters are outside a narrow range. This is defined as one standard deviation outside the mean, marked as dashed vertical lines in Figure 3.2, in both cases.

A correction for the arrival-time jitter (t_{jitter}) is applied to the nominal delay stage position ($t_{nominal}$) on a shot-to-shot basis to obtain the actual pump-probe delay (t) according to:

$$t = t_{nominal} + t_{jitter} \tag{3.5}$$

The time-tool has the temporal resolution of approximately 20 fs [86]. Following the correction the delays are binned into 50 fs bins from -2 ps to 2 ps and 200 fs bins from 2 ps to 6 ps in order to equalise the number of shots which make up each bin. Additionally, the signal in each time bin was subsequently normalised to the number of shots in the bin.

3.3.2 Time-of-flight calibration

A time-of-flight spectrum was produced by plotting a histogram of the recorded ion arrival times τ. When investigating ions (as opposed to electrons) it is desirable to convert the time-of-flight to a mass-to-charge ratio, thus producing a mass spectrum. All ions are accelerated across the same distance by the same force; they are provided with the same KE ($E_{kinetic}$):

$$E_{kinetic} = \frac{1}{2}mv^2 \tag{3.6}$$

where m is the mass of the ion, and v is the velocity. This $E_{kinetic}$ is determined by the acceleration voltage (V) and charge of the ion ($e \times\ z$).

$$E_{kinetic} = ezV \tag{3.7}$$

Equations 3.6 and 3.7 can be set equal and rearranged to describe the velocity of an ion as a function of its m/z value as follows:

$$v = \sqrt{\frac{2V \times e}{m/z}} \tag{3.8}$$

The ions drift for length L at this velocity. The time delay (τ) from the formation of the ions to the time they reach the detector can be described as:

$$\tau = \frac{L}{\sqrt{2V \times e}} \times \sqrt{m/z} \tag{3.9}$$

Because L, V, and e are constants, Equation 3.9 can be simplified to:

$$\tau = C \times \sqrt{m/z} \tag{3.10}$$

where $C = \frac{L}{\sqrt{2Ve}}$, a first-order polynomial can be fitted to Equation 3.10 using time-of-flight points with a known m/z values within the spectrum.

3.3.2.1 UV only mass spectrum

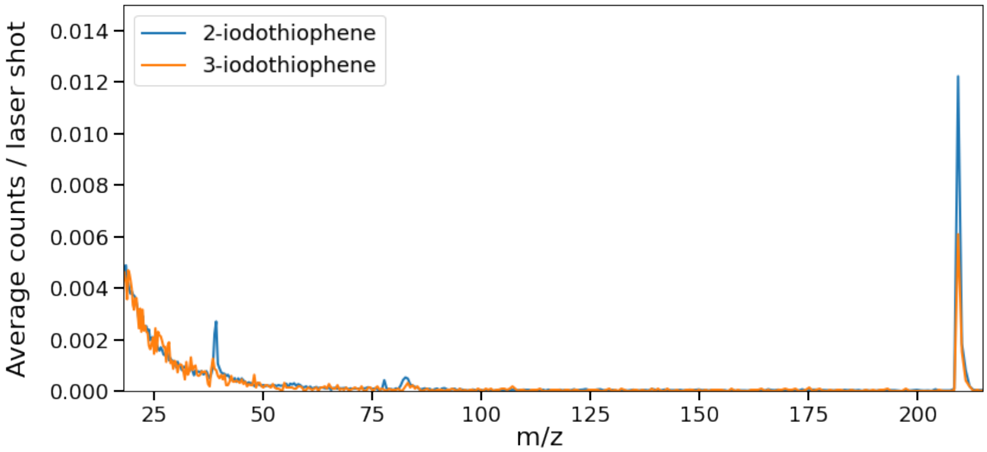

FIGURE 3.3: Mass spectra obtained following ionisation of 2IT (blue) and 3IT (orange) with 2 μJ of 262 mn UV pump alone. Both spectra are normalised to the total number of shots combined to produce them.

As outlined in Section 3.1.1.1, it is essential to maintain a low power for the UV pump laser to prevent the formation of charged products by the pump. In order to maximize the number of molecules undergoing neutral photodissociation, the UV power should be set just below the threshold for creating charged parent ions. To confirm this is the case, the mass spectra obtained upon ionisation of 2IT and 3IT solely with the pump pulse, with 2 μJ of power, are presented in Figure 3.3 ,where some discernible structures are observed. A prominent peak at approximately 40 m/z is attributed to the ionisation of the background gas, such as CO_2 (m/z = 44). Furthermore, small peaks connected to the parent molecule (m/z = 210) and the ring product (m/z = 83) are also evident.

The typical heights of the peaks noticed in these spectra were negligible, providing less than 0.005 counts per laser shot. Equivalent pump-probe (where the probe pulse generates ions) spectra are presented in Figure 3.6 where the average intensity observed is approximately 0.7 counts per laser shot. Given this context, any effect from UV-only ionisation can be considered insignificant when compared to the pump-probe signals that are of main interest of investigation and the UV power remained set to 2 μJ for the rest of the experiment.

3.3.3 Determination of time-zero

As mentioned in Section 3.2, the time zero (i.e. the time when the pump and probe pulses temporally overlap) was initially estimated to be the point at which the low-kinetic-energy features emerged during the experiment. Although this estimation

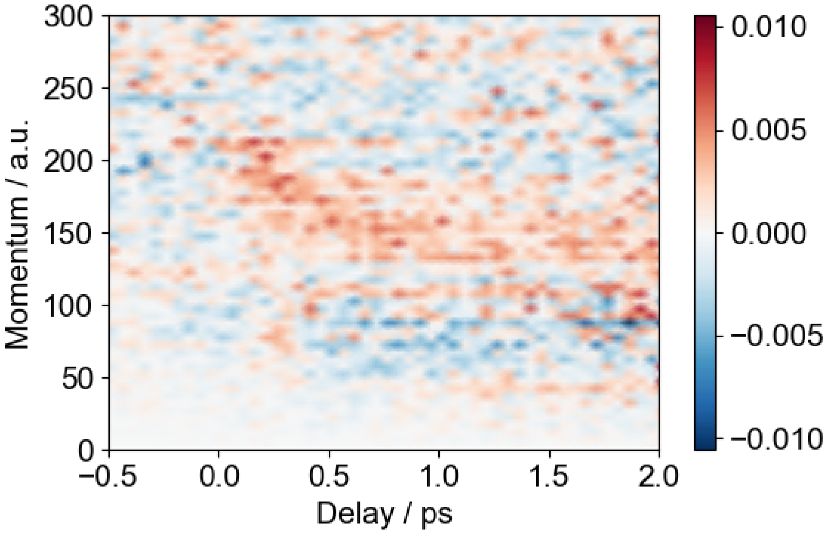

FIGURE 3.4: Residual difference between experimental data and the fit described in Section 2.4.4 of I^{2+} obtained following photolysis of 2IT. Illustrating the characteristic "hockey-stick" signal (red) associated with classic Coulomb Explosion.

was sufficient at that time, it does not provide an accurate approximation for further analysis. These low energy features are indicative of products resulting from neutral UV photodissociation, which have reached a separation greater than the critical distance for charge transfer and have not gained any additional energy from Coulomb repulsion. Because time is required to reach this distance, it is expected that there will be a delay between the time of laser overlap and their appearance. Furthermore, the validity of this estimate is hindered by the unknown dynamics that occur on excited potential energy surfaces.

To obtain a more precise estimate of time-zero, the non-zero probability of ionising atoms other than iodine was leveraged. As per the information presented in Table 3.1, the next most likely site in the molecule to be ionised is carbon. When two XUV photons interact with the photolysis products, one ionising iodine and the other a carbon on the thiophene ring co-fragment, two charged species are generated. This leads to Coulomb repulsion between the fragments, providing additional KE. The extent of repulsion is dependent on the intermolecular distance and decreases as the ions move apart, which results in the typical "hockey-stick" Coulomb curve. Further analysis of this data includes a simulation which will be described in detail in Section 3.4.4. This is mentioned here as the simulation does not consider the processes which lead to the presence of the Coulomb curve. Consequently, the Coulomb curve was isolated in the residual between the simulation and experimental data, this is shown in Figure 3.4.

The integrated ion yield from the residual between data and simulation associated with the Coulomb curve as a function of the pump-probe delay is shown in Figure 3.5.

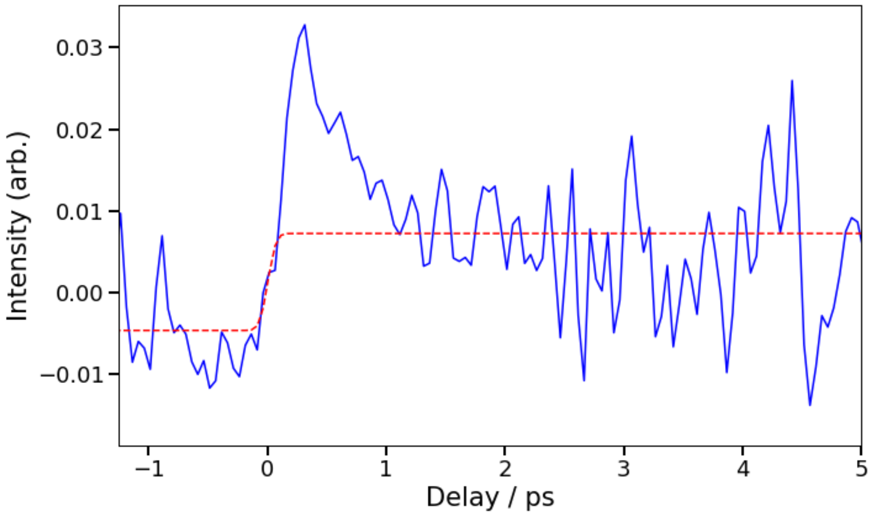

FIGURE 3.5: Integrated intensity between 150-200 arb. units of the residual between simulated and experimental data as a function of pump-probe delay(blue). An error function was fit using pre-time zero baseline and asymptotic intensity, the result is shown in red.

Due to the ”hockey-stick” shape caused by the KE decreasing with time, the wider the integration limits, the broader (in time) the feature appears. To obtain the most accurate estimate of time zero, the integration limits should be set as narrow as possible, while maintaining a curve with good contrast. To further avoid errors associated with the broadening, the onset of the CE is modelled by fitting an error function to the pre-time zero baseline and asymptotic intensity. The result of this fit is shown in red in Figure 3.5. Time zero was defined as the midpoint of the error function. All pump-probe delay plots presented in this chapter are in reference to this. The absolute value of this parameter is still influenced by the molecular dynamics and cross-correlation of the two laser pulses, and thus serves as an upper limit for both time zero and the full width at half maximum (FWHM) of the cross-correlation. The position of time zero changes by approximately 40 fs when the integration limits are shifted, therefore a cautious error of ± 50 fs is used. The FWHM value for cross-correlation is 175 fs.

3.4 Results and Discussion

3.4.1 Pump-probe mass spectra

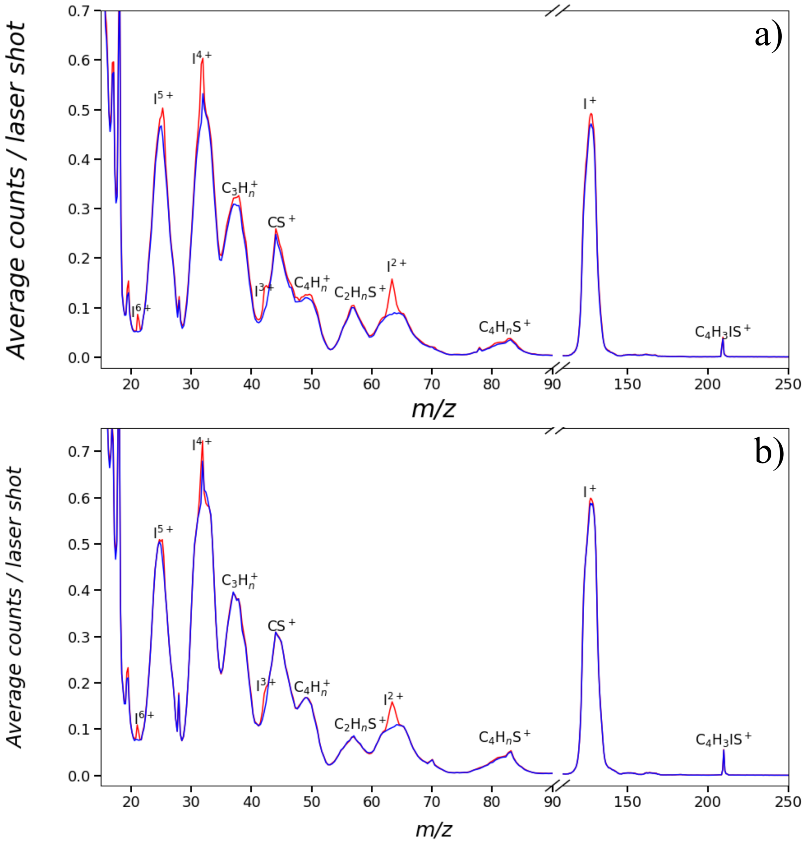

FIGURE 3.6: Mass spectra obtained from ionisation of 2IT a) and 3IT b) by UV + XUV pulses (red) and by XUV pulses only (blue). Each spectrum has been normalised by the total number of shots. The UV + XUV signal has been summed over all positive pump-probe delays (i.e. with the UV pulse preceding the XUV pulse).

Two sets of two mass spectra, obtained from photoionisation of 2IT and 3IT, are presented in Figure 3.6, as a function of average ion count per laser shot, integrated over two pump-probe delay regions. The UV early mass spectrum, shown in blue, is the one in which the UV pulse arrives first. The UV late mass spectrum, shown in red, represents the combined contribution from both the UV and XUV pulses. The UV late spectrum has been integrated at all positive pump-probe delays. The mass spectra obtained from both isomers have similar fragmentation patterns. Both UV early and UV late spectra of both isomers show peaks associated with atomic iodine in charge states up to 6+, as well as various carbon and/or sulfur-containing fragments. These observed peaks are relatively broad, which is indicative of ions being produced with a wide range of recoil velocities following ionisation and CE.

The consequences of preceding XUV with the UV pump pulse are most noticeable in atomic iodine peaks. The interaction with UV results in an increase in intensity of the I^{n+} peaks, which is observed over a narrow range of m/z values, indicating a narrowing of the KE carried by the iodine atom. This effect is most apparent in the I^{2+} peak. As previously stated, ionisation with a single 95 eV photon is expected to generate primarily iodine ions in the 2+ state, and this peak appears in the region of the spectrum otherwise unoccupied by signal from other ions. Therefore, the features and temporal changes associated with the I^{2+} ion provide the clearest time-dependent changes.

3.4.2 Ion images

The UV-induced changes in the energy distribution of various I^{n+} ions can be more effectively examined by analysing the corresponding ion images. In Figure 3.7 and Figure 3.8, the images of iodine in charge states from 2+ to 5+, which were generated from the ionisation of 2IT and 3IT, are displayed. These images were divided into three pump-probe delay regions to demonstrate the progression of events over time. The delay regions include pre-time zero, which represents the CE of the ground state equilibrium molecule contribution; early pump-probe delays, which illustrate the onset of pump-probe features over the first 500 fs; and late pump-probe delays, which show the change in pump-probe features as the reaction proceeds >3ps. The experiment was conducted under VMI conditions, where the intensity at a higher radius in the images corresponds to ions with a higher recoil velocity and, consequently, higher energy.

Focusing initially on images associated with I^{2+}, three clear features were observed in images related to both isomers. First, a diffuse ring is present at large radii (indicative of high-energy ions) in all images, marked as i) in Figures 3.7 and 3.8. This feature is attributed to the CE of the intact molecule. Prior to the interaction of UV with the molecule, the FEL ionises iodine, while it is a part of the intact molecule. The resulting charge then spreads throughout the system, resulting in a CE. The repulsive Coulomb forces generated by this high charge provide additional energy to the recoiling fragments, resulting in the formation of a diffuse ring at the largest radii. This ring is evident at all time delays, although its intensity may decrease due to a reduction in the number of intact molecules undergoing CE.

The second in energy feature is the first pump-probe signal, which is evident at early and late pump-probe delays with lower radius relative to the CE signal, marked as ii). This feature has anisotropic character, with increased intensity parallel to the UV laser polarization axis. This suggests a dissociation of a bond with a transition moment dipole parallel to the UV laser. The anisotropy also implies that the bond dissociates quickly, prior to the molecule undergoing rotational dephasing following excitation by

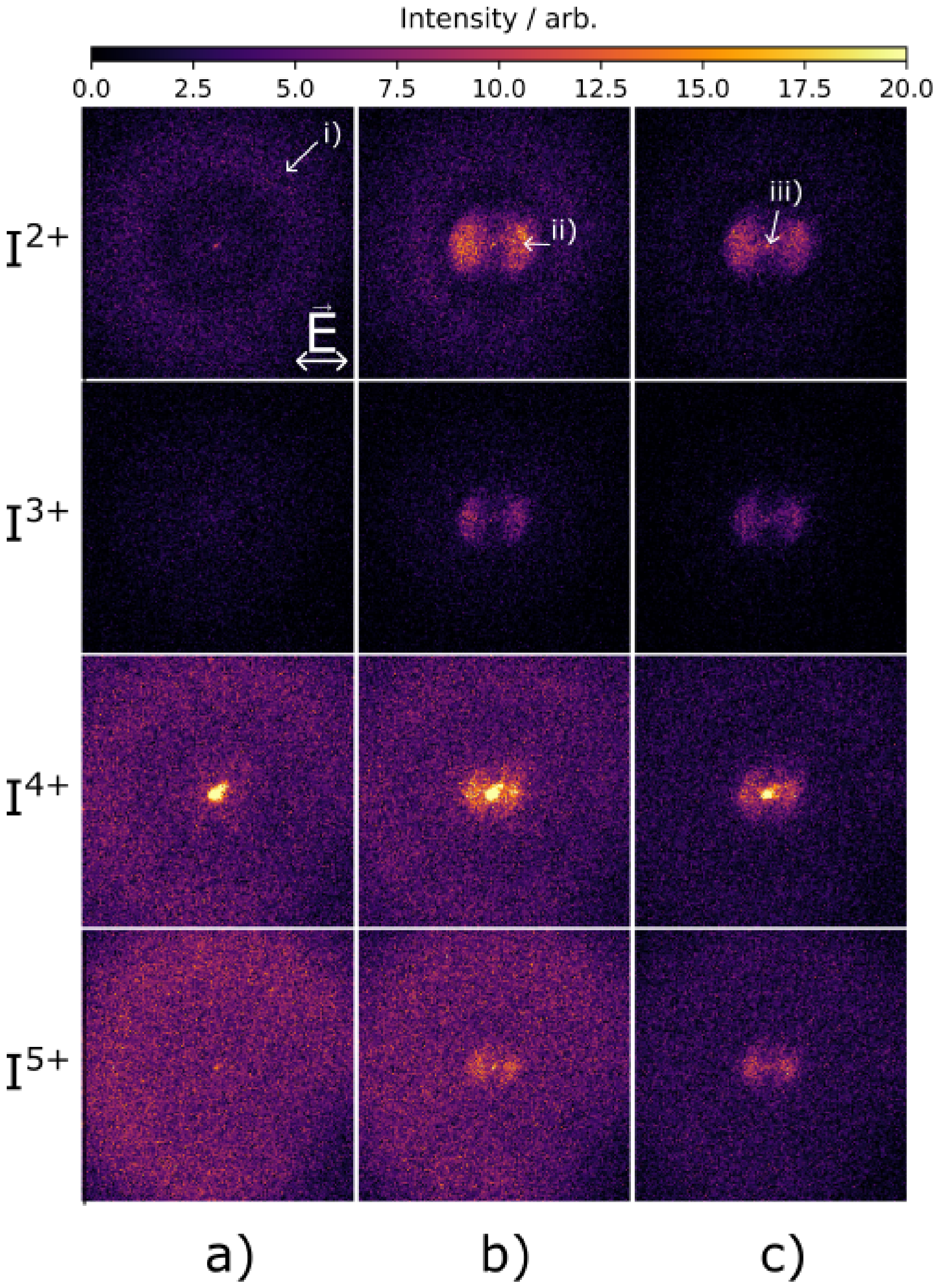

FIGURE 3.7: Ion images of iodine photoproducts in charge states from 2+ to 5+ following ionisation of 2IT by XUV only (column a)), pumped by UV and subsequently ionised: summed over 200-500 fs (column b) and at all delays >3 ps (column c)).

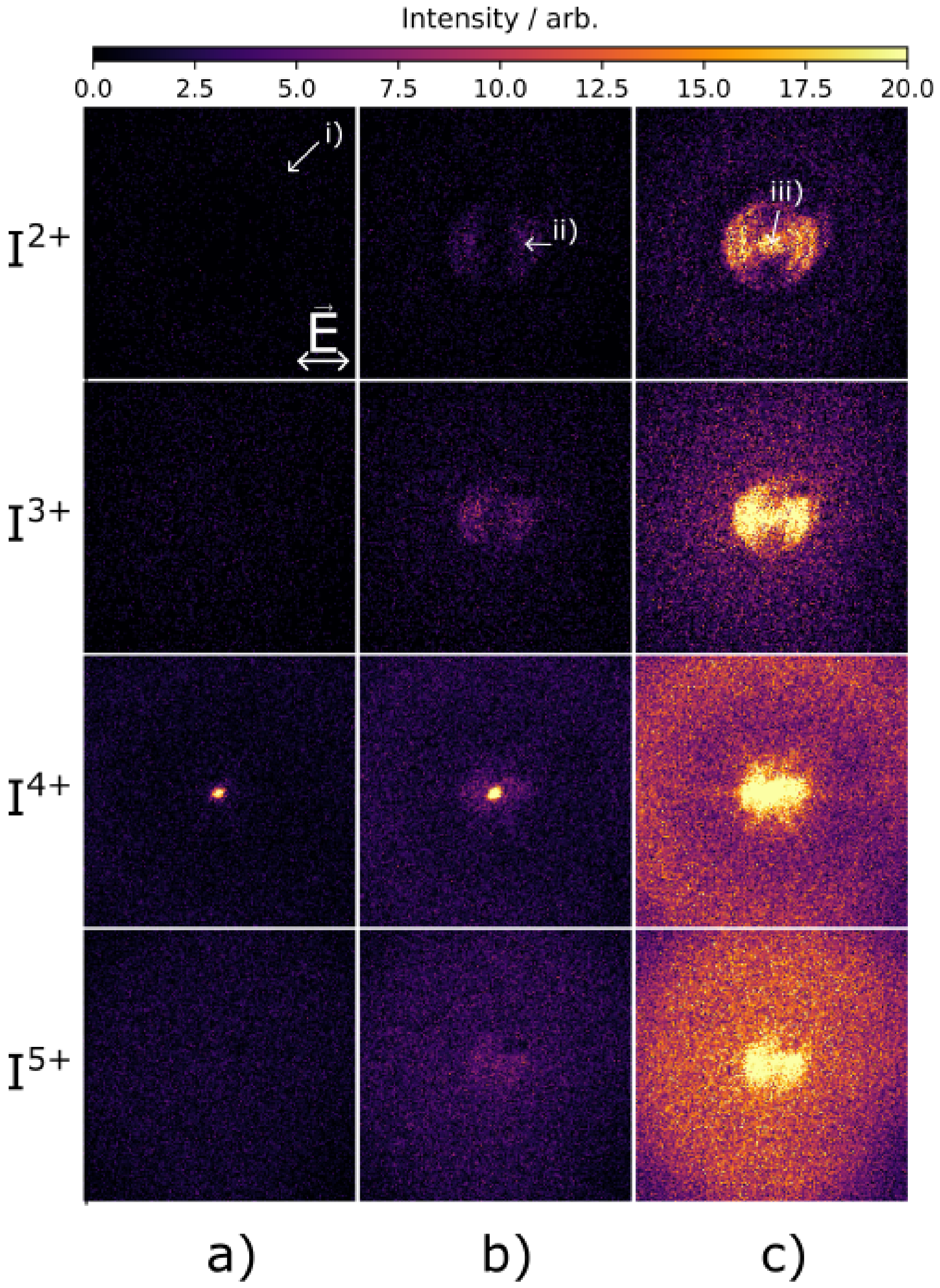

FIGURE 3.8: Ion images of iodine photoproducts in charge states from 2+ to 5+ following ionisation of 3IT by XUV only (column a)), pumped by UV and subsequently ionised: summed over 200-500 fs (column b) and at all delays >3 ps (column c)

a UV photon. There is a discernible difference in the appearance of this feature between the two isomers. Specifically, more structure is visible in this region when examining ion images resulting from photolysis of 3IT. This is most apparent in the I^{2+} ion, and faintly detectable in the I^{3+} ion. For ions in higher charge states, this feature is not expected to disappear, but rather the experimental resolution may not permit full structural determination.

The third feature is an isotropic ring situated at a small radial distance from the centre of the image, which becomes apparent only at late pump-probe delays and is marked as iii). Both of the pump-probe features show the same characteristics as those previously reported in the nanosecond REMPI study [22].

The three features are present in images associated with iodine in higher charge states however, an additional prominent peak is apparent in all images connected to I^{4+} at all time delays of both isomers. This is likely not connected to the molecule and its motions, but rather the result of scattered beams from the sides of the experimental chamber striking the detector or ionisation of background gas such as O_2^+ which overlaps with I^{4+} in terms of its m/z value ($m/z = 36$).

3.4.3 Time-resolved Momentum Distributions

The momentum distribution of the atomic iodine products in charge states ranging from 2+ to 4+ is depicted in Figure 3.9 using atomic units (a.u.). The plot illustrates the distribution as a function of pump-probe delay, with the pump induced changes shown as difference spectra for clarity. The pre-time-zero, where the XUV laser pulse arrives before the UV pulse, momentum distribution has been averaged and used as the ground state signal. This was subtracted from the spectra at each time delay to generate the difference spectra. In the figures, red indicates an increase in the signal relative to the ground-state signal, while blue indicates a decrease.

The three features identified in the images presented in Section 3.4.2 are clearly visible in Figure 3.9. After time zero, a significant depletion of the ground state can be seen as a broad blue feature at momentum values extending above 120 a.u., whereas the low-energy products of the UV-induced dissociation are visible as red enhancements below 120 a.u.. The momentum of these features is constant with time indicating these correspond to neutral dissociation products. The average momentum distributions at early (200-500 fs) and late (>3ps) pump-probe delays are shown to the right of the figures. The two pump-probe features described in Section 3.4.2 are seen here as significantly overlapping peaks with distinct appearance times. The higher energy peak is centred at approximately 90 a.u. and is close to time zero. The intensity of this peak continues to rise as the second, less intense peak, centred at approximately 30 a.u., appears at later pump-probe delays. Both these features appear after time zero,

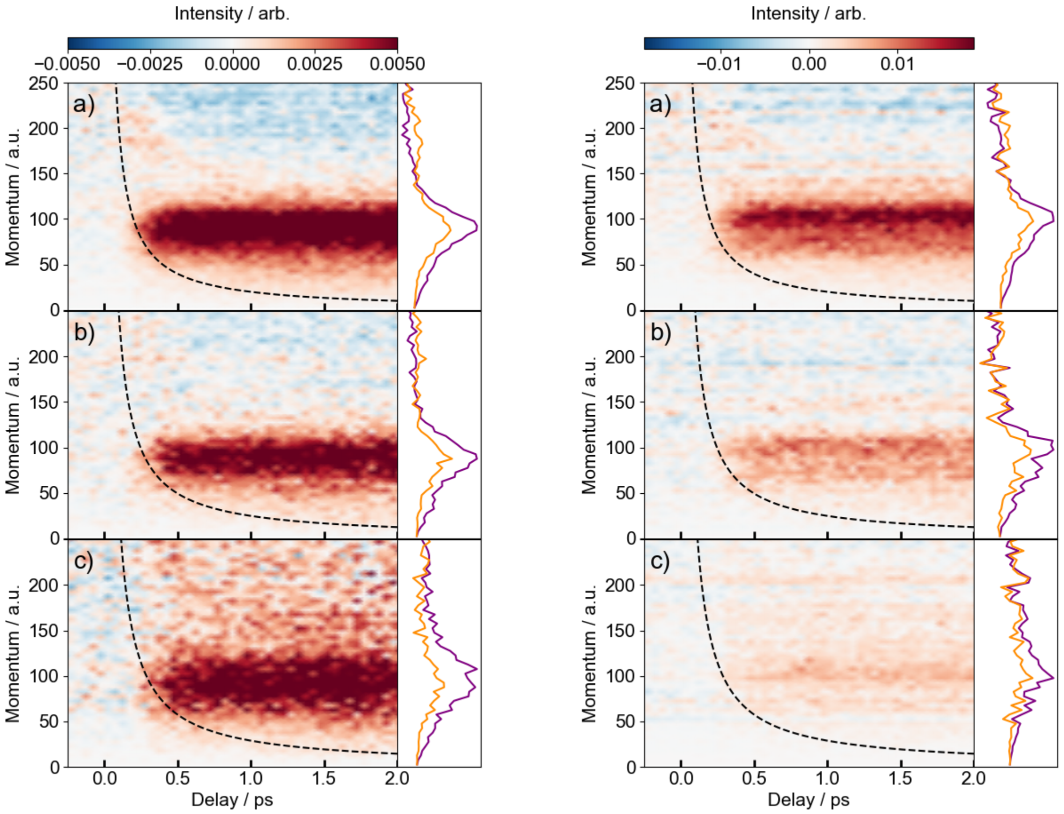

(A) 2IT

(B) 3IT

FIGURE 3.9: Time-resolved difference maps of the momentum distributions of the a)I^{2+}, b) I^{3+}, c) I^{4+} fragments formed followed by 262 nm photolysis of A) 2IT and B) 3IT and subsequent ionization with XUV probe. The ground state contribution (UV arriving after XUV) was subtracted. The momentum distributions at early (200-500 fs) and late (>3 ps) pump-probe delays are projected on the right-hand side of the panels as orange and purple lines respectively. The black dashed lines depict the expected appearance times of the fragments based on the OBT model.

and their momentum is unaffected by the pump-probe delay. This confirms that these signals are connected to two neutral dissociation pathways that occur after the absorption of the UV photons.

While these features can be seen in all charge states, there is a notable decrease in the signal-to-noise ratio with increasing charge. This is due, in part, to a decrease in the yield of higher charge state iodine ions following ionisation with the XUV, as well as increased overlap with other fragments.

The delayed appearance of lower-energy peaks, even in the scenario where fragmentation from both pathways occurs simultaneously, is expected due to the increased time taken by the fragments with lower velocity to reach critical separation, where CT is no longer allowed. If we assume instantaneous bond breaking and acceleration to asymptotic velocities, we can calculate the time taken to reach the critical distance using the OBT model described in the Introduction of this chapter. Any significant difference from this value and the measured appearance times of the fragments suggest a mechanism that leads to delayed bond fission.

The calculated appearance times of all the presented iodine fragments, obtained using equation 3.4 are shown in Figure 3.9 as dashed black lines. There are no direct measurements of the radical's ionisation energy. However, it can be estimated using Hess' Law and previously reported values for: IP of thiophene (8.87 eV)[89], appearance threshold for forming $C_4H_3S^+$ + H (13.05 ± 0.05 eV) [89, 90], and C-H bond strength in thiophene (4.99 ± 0.13 eV)[91, 92]. This gives an $IP_{C_4H_3S}$ value of approximately 8.06 eV. A study on furan (the oxygen analogue of thiophene) found the difference between $\alpha-$ and $\beta-$C-H bond strengths to be negligible[93], therefore the same IP value is used for both isomers. To further confirm the value of IP the Gaussian computational package [94] was used with the second order perturbation theory (MP2) and Dunning's contracted cc-pVDZ basis set [95] which yielded an IP value of 8.3 eV for a closed-ring co-fragment. An approximate value of 8 eV was used.

The clear dependence of the appearance time on the momentum can also be leveraged to aid in the deconvolution of the spectrum, which is particularly helpful in cases such as the one presented in this chapter where the peaks of interest significantly overlap. This procedure is described in the following section.

3.4.4 Data Fitting

The strong overlap of the pump-probe features makes it challenging to differentiate the individual contributions. Despite this challenge, it is important to distinguish them to obtain information about the timescales related to the two distinct neutral dissociation pathways.

Without considering the minimal signal from the Coulomb curve, the total momentum distribution can be viewed as composed of three elements: high-energy XUV-induced CE of the ground state molecule, prompt signal associated with UV induced dissociation observed at intermediate momentum, and delayed signal associated with UV induced dissociation at low momentum. All these components are heavily overlapped; however, owing to their distinct temporal properties, a basis function can be derived to represent each component individually. Individual basis functions were derived for each isomer and charge state.

The basis function related to the XUV-induced Coulomb explosion was defined as the pre-time-zero averaged spectrum. At negative time delays, iodothiophene interacts with XUV prior to UV, resulting in momentum distributions that reflect only the fragmentation of the ground state molecule. The basis function for the XUV-induced

CE of the ground-state molecule is shown in green in panels a) of Figures 3.10 and 3.11.

At early pump-probe delays (200-500 fs), the spectrum is composed of contributions from the depletion of the ground state signal, as well as the prompt higher-energy UV-induced dissociation signal. The signal associated with low-energy UV-induced dissociation is not present, as the fragments have not yet reached the critical distance. A scaled subtraction of the ground-state signal was performed to obtain a spectrum free of the ground-state depletion contribution. The portion of the momentum distribution where no pump-probe features were present ($>$ 120 a.u.) was utilised, and the ground state basis function was then scaled using a least-squares fitting algorithm to bring the intensity in this region close to zero. The scaled ground-state signal was then subtracted from the momentum distributions at all delays. This scaling is necessary because extracting the basis function of the UV-induced dissociation from the unscaled difference momentum distribution would result in double weighting of the ground state depletion in the area where the distributions overlap. Following subtraction, the basis function was obtained by integrating the early time signal and is shown in blue in panel a) of Figures 3.10 and 3.11.

The final necessary basis function is related to the delayed low-energy UV-induced dissociation. The momentum distribution spectrum, obtained through scaled background subtraction, is formed from the contributions of both UV-induced dissociation channels at late times ($>$ 3ps). To isolate the signal from the delayed channel, the early time spectrum was subtracted from the late-time spectrum. During this analysis, it became evident that the decreasing signal-to-noise ratio at higher iodine charge states was insufficient to isolate this signal. As a result, this signal was utilised to describe the I^{2+} spectrum (of both isomers) and omitted in the fitting process for all other charge states. Instead, these were described as a combination of the depletion of the XUV-induced ground state and prompt UV-induced neutral dissociation. Where it is used, the basis function describing the delayed channel is shown in red in panel a) of Figures 3.10 and 3.11.

The relationship between the appearance times of the high momentum pump-probe signal connected to prompt UV-induced dissociation and ground-state depletion is inherently linked. The emergence of the pump-probe signal signifies the moment when the fragments are separated by more than the critical distance, and CT is no longer allowed. Because CT leads to CE of the molecule, once it stops, the XUV-induced CE signal will deplete. Consequently, the changes in the intensity profiles related to the basis function representing these processes will exhibit the same temporal characteristics, but with opposite signs. The delayed dissociation signal (in the case of I^{2+}) has its own distinct set of parameters, and is expected to cause further depletion of the ground state signal. However, as the delayed dissociation forms a much weaker channel and the depletion is spread over such a wide momentum range,

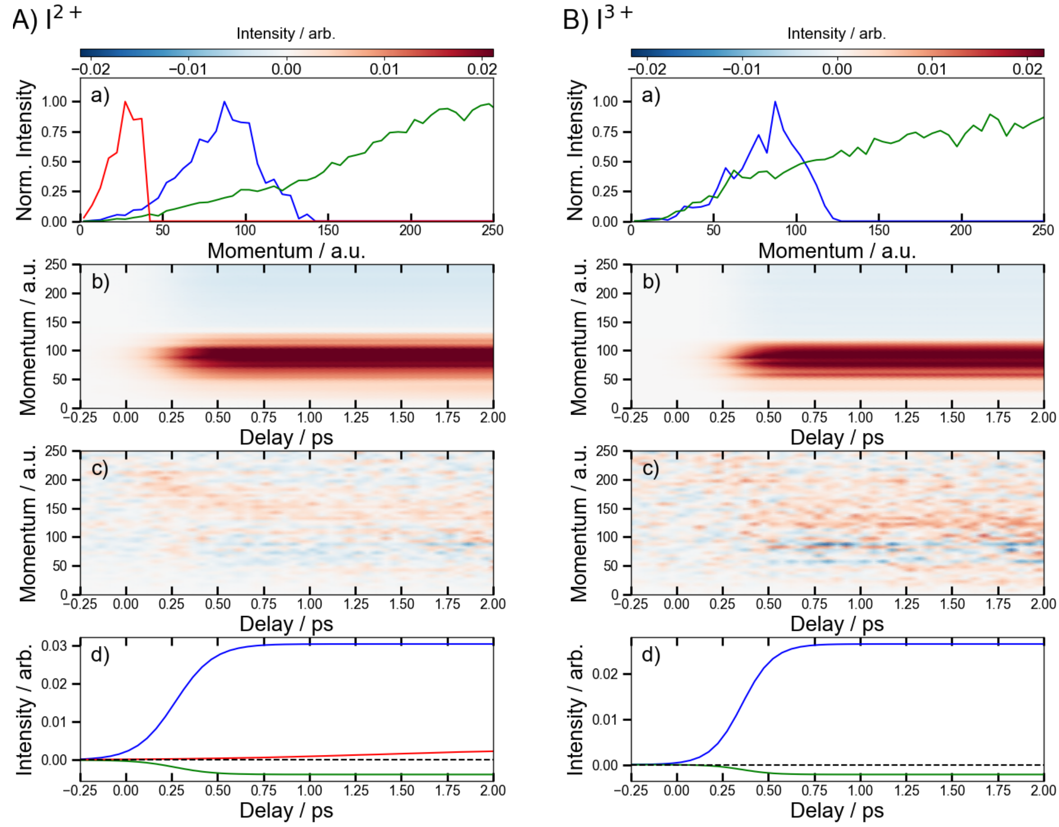

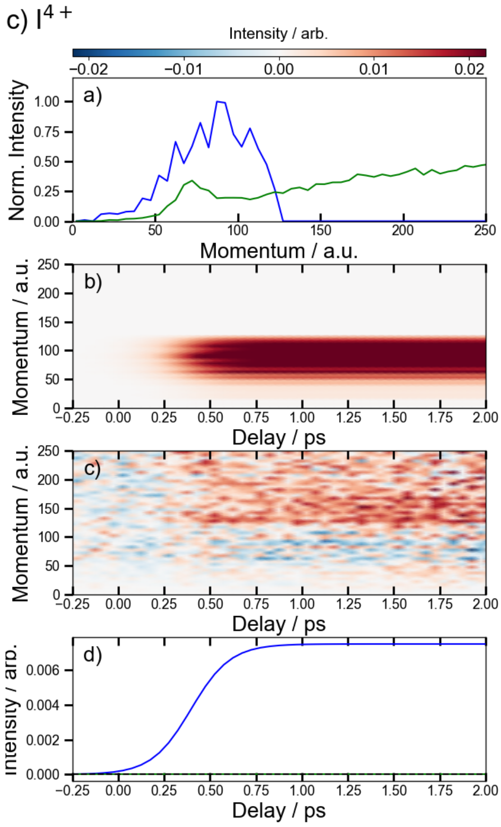

FIGURE 3.10: Figures summarizing the fitting procedure described in text of the momentum distributions of the A)I^{2+}, B) I^{3+}, C) I^{4+} fragments formed followed by 262 nm photolysis of 2IT. a) Momentum basis functions depicting the ground state (green), prompt dissociation (blue) and delayed dissociation (red) momentum distributions. Shown with common peak intensity. b) Fit to the experimental data using a time-varying sum of the three basis function as per Equation 3.12 c) Residual error between the experimental and fitted data . d) Time-dependent amplitudes of the basis functions obtained from the fit using the same color scheme as panel a).

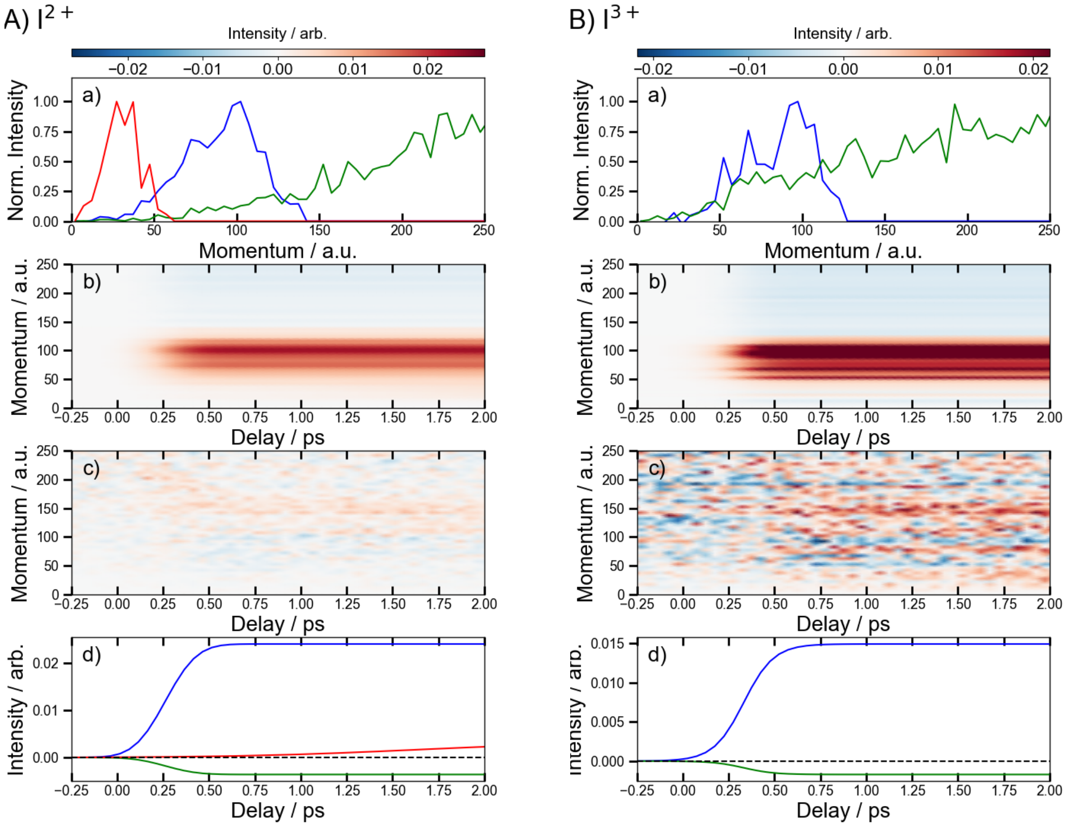

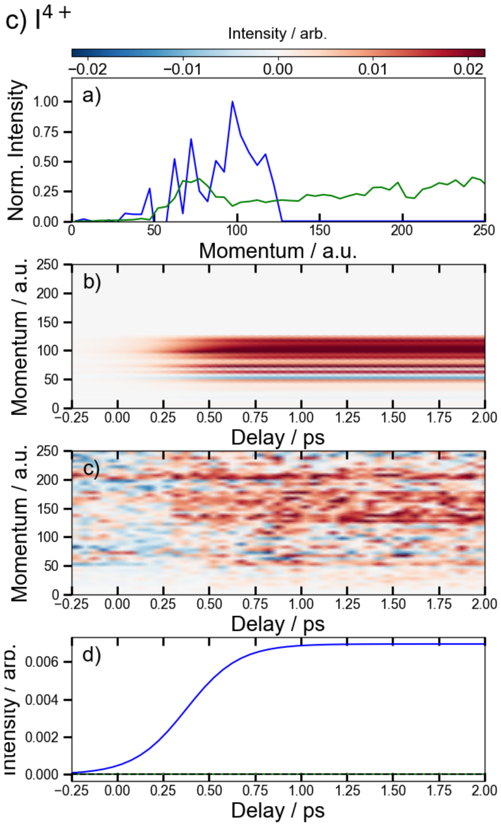

FIGURE 3.11: Figures summarizing the fitting procedure described in text of the momentum distributions of the A)I^{2+}, B) I^{3+}, C) I^{4+} fragments formed followed by 262 nm photolysis of 3IT. a) Momentum basis functions depicting the ground state (green), prompt dissociation (blue) and delayed dissociation (red) momentum distributions. Shown with common peak intensity. b) Fit to the experimental data using a time-varying sum of the three basis function as per Equation 3.12 c) Residual error between the experimental and fitted data . d) Time-dependent amplitudes of the basis functions obtained from the fit using the same color scheme as panel a).

this cannot be resolved within the scope of this experiment. The temporal characteristics of the changes associated with each basis function were described using a logistic function. A weighted sum of these functions was fitted to the experimental momentum distribution map according to:

$$\begin{aligned} S(\epsilon_k, t) = A_{\mathrm{gs}} D_{\mathrm{gs}}(\epsilon_k) \left[\frac{1}{1 + e^{-k_{\mathrm{prompt}}(t - t_{\mathrm{prompt}})}}\right] + \\ A_{\mathrm{pd}} D_{\mathrm{pd}}(\epsilon_k) \left[\frac{1}{1 + e^{-k_{\mathrm{prompt}}(t - t_{\mathrm{prompt}})}}\right] + \\ A_{\mathrm{dd}} D_{\mathrm{dd}}(\epsilon_k) \left[\frac{1}{1 + e^{-k_{\mathrm{delayed}}(t - t_{\mathrm{delayed}})}}\right] \end{aligned} \tag{3.11}$$

where $S(\epsilon_k, t)$ is the signal intensity dependent on the pump-probe delay time, t, and momentum, ϵ_k. The momentum-dependent basis functions obtained from the experiment are given by $D_{\mathrm{gs}}(\epsilon_k)$, $D_{\mathrm{pd}}(\epsilon_k)$ and $D_{\mathrm{dd}}(\epsilon_k)$ for the ground-state depletion, prompt dissociation, and delayed dissociation signals, respectively. The centre of the rise of the logistic functions in time is defined by t_{prompt} for the ground-state depletion and prompt dissociation signal, and t_{delayed} for the delayed signal. k_{prompt} and k_{delayed} are the rate constants associated with prompt and delayed signals, respectively. The amplitude of each term in the sum is then given by the constant, A_i, which controls the relative contributions of the basis functions to the overall signal. For charge states higher than 2+, only the first two terms are used and the equation becomes:

$$\begin{aligned} S(\epsilon_k, t) = A_{\mathrm{gs}} D_{\mathrm{gs}}(\epsilon_k) \left[\frac{1}{1 + e^{-k_{\mathrm{prompt}}(t - t_{\mathrm{prompt}})}}\right] + \\ A_{\mathrm{pd}} D_{\mathrm{pd}}(\epsilon_k) \left[\frac{1}{1 + e^{-k_{\mathrm{prompt}}(t - t_{\mathrm{prompt}})}}\right] \end{aligned} \tag{3.12}$$

The optimisation of the values for k_{prompt}, $k_{delayed}$, t_{prompt}, $t_{delayed}$, and A_{gs}, A_{pd}, and A_{dd} for the 2IT and 3IT data was achieved through least-squares fitting of experimental data to the spectrum described by Equation 3.12. The optimised fit parameters are presented in Table 3.3, and the calculated signal and residual maps are depicted in panels b) and c) of figures 3.10 and 3.11 for 2IT and 3IT, respectively. The time-dependent contributions are illustrated in panel d) of the figures. In the case of I^{2+}, this emphasises the delayed appearance and significantly reduced contribution of delayed dissociation. The model provides a good match to the experimental data for the neutral dissociation signal. The contribution from the Coulomb curves resulting from the non-negligible ionisation of the ring cofragment by the XUV, which was not included in the model, is more apparent in the residual plots.

Isomer	2IT			3IT		
Iodine charge state	I^{2+}	I^{3+}	I^{4+}	I^{2+}	I^{3+}	I^{4+}
k_{prompt} / ps^{-1}	10 ± 0.4	11 ± 1.0	9.5 ± 1.5	12 ± 0.9	12 ± 4	7.0 ± 2.8
$k_{delayed} / ps^{-1}$	2.0 ± 0.9	-	-	1.9 ± 0.7	-	-
t_{prompt} / fs	267 ± 50	297 ± 50	338 ± 50	264 ± 50	268 ± 50	305 ± 50
OBT_{prompt}	248	290	338	248	290	338
$t_{delayed} / ps$	1.4 ± 0.1	-	-	1.6 ± 0.1	-	-
$OBT_{delayed} / fs$	660	-	-	660	-	-

TABLE 3.3: Values of k_i, and t_i obtained from fitting the experimental data to equation 3.12 as well as the expected apperance times calculated using Equation 3.4 assuming instantaneous bond breaking and acceleration to asymptotic velocities.

The results of the calculations using the OBT model for the prompt dissociation channel are listed in Table 3.3 as OBT_{prompt}, they are also plotted for all momentum values as black dashed line all panels in Figure 3.9. This model was utilised to determine the critical distance beyond which CT is prohibited, as defined by Equation 3.4. With the distance and momentum (and subsequently, the velocity) of the fragments known, the appearance time can be easily calculated under specific assumptions. These assumptions include that the molecule dissociates promptly into an I atom and a thiophenyl radical partner and that the fragments reach asymptotic recoil velocity instantaneously. It should be noted that this assumption may affect the very early time signal most significantly. Nonetheless, previous studies have shown that this velocity is likely attained within a few tens of femtoseconds, assuming ballistic motion along a repulsive potential surface, which is expected for a prompt dissociation [96, 97]. Therefore, this approximation should fall within the experimental error range and have little to no impact on the conclusions of this analysis. Because the critical distance increases with increasing charge state, the appearance time is expected to shift towards longer pump-probe delays.

The appearance time obtained from the fit corresponds to the average time taken to reach the critical distance because the fragments possess a range of momenta. The agreement between the observed and calculated appearance times of the prompt dissociation feature is generally good, showing the expected increase in appearance time with increasing charge state. This trend is evident for all charge states derived from both isomers. This result supports the proposed hypothesis that the higher-momentum neutral dissociation fragments arise from a prompt and direct photodissociation process.

The investigation of the delayed channel's values was limited to the I^{2+} fragments. Based on the fit, the extracted appearance times were $\sim$ 1.4 ps for the 2IT isomer and 1.6 ps for the 3IT isomer. The peak of the delayed momentum distribution for both isomers was $\sim$ 30 atomic units, which, assuming prompt dissociation and constant recoil velocity, would result in an appearance time of approximately 660 fs according to the OBT model. The 1 ps difference between these values is beyond the expected experimental error and can potentially be attributed to a delayed dissociation process involving surface crossings, as further discussed in later sections.

During the fitting process, another parameter, known as the rate constant (k), was extracted, which dictates the rate at which signals rise and has an inverse relationship with the respective time constants. These time constants are interpreted here as being directly proportional to the momentum spread of the features. The velocity of the fragment has a direct impact on its appearance time, with the signal starting to rise when the fastest fragment reaches its critical separation and eventually approaching its asymptotic value once the slowest fragment has done the same. The momentum distributions of the prompt dissociation feature, shown in blue in panels a) of Figures 3.10 and 3.11, display full width half maximum (FWHM) values spanning approximately 65-110 atomic units (a.u.) range for all iodine charge states of both isomers. The OBT model predicts a narrow range of appearance times at this momentum, which is evident as the steep gradient of the black dashed line in Figure 3.9. The model, assuming prompt dissociation, predicts a spread of appearance times of approximately $\sim$120 fs, a value similar to but not negligibly longer than the respective $1/k$ values. This difference is likely attributable to the presence of the Coulomb curve on the high-momentum side of the distribution, resulting in a broadening of the peak that is not accounted for within the OBT model.

Further study of rise time constants, associated with iodine in the 2+ charge state, offers valuable insights into the time constants related to the delayed dissociation process. The observed rise time is consistent with that calculated using the OBT model, which is approximately 500 fs for both isomers. This further supports the notion that time constants are mainly influenced by the spread of recoil velocities, whereas time offsets describe the time taken to reach a critical separation. Moreover, it is noteworthy that the kinetic parameters obtained for the two isomers are very similar.

The ability to resolve the momentum distributions of the prompt and delayed channels, which contribute to the overall I^{2+} signal, enables estimation of their relative contributions. The relevant basis functions are multiplied by the amplitude obtained from the fit (providing the distribution at asymptotic times), and the area under the resulting curve is proportional to the yield of the I atoms produced through the respective processes. The ratio of these areas provides the branching ratio, BR, which is 23 ± 2 and 16 ± 3 for 2IT and 3IT, respectively. This demonstrates that prompt dissociation is the major channel of the neutral UV-induced photodissociation process, but that the delayed channel is more significant in 3IT than in 2IT.

3.4.5 Energy partitioning in the fragments

To further explore the difference between the contributions of the two channels to the momentum distribution of the two isomers the asymptotic TKER distribution was calculated. The TKER distributions are obtained from the asymptotic momentum distributions obtained from the I^{2+} channel, assuming the co-fragment is the thiophenyl radical. The TKER is derived, using equation 3.13, from the dissociation products of the two isomers, obtained from the pump-probe data collected at delays of over 3 ps and assuming a mass of 83 amu for the partner fragment. They have been plotted in Figure 3.12. Equation 3.13 is derived using the law of momentum conservation.

$$TKER = \frac{p_{I^{2+}}^2}{2}\left(\frac{m_2 + m_1}{m_1 m_2}\right) \tag{3.13}$$

where $p_{I^{2+}}$ is the measured momentum of the I^{2+} fragment, and m_1 and m_2 are the known masses of the iodine (127 amu) and the thiophenyl radical (83 amu) fragments.

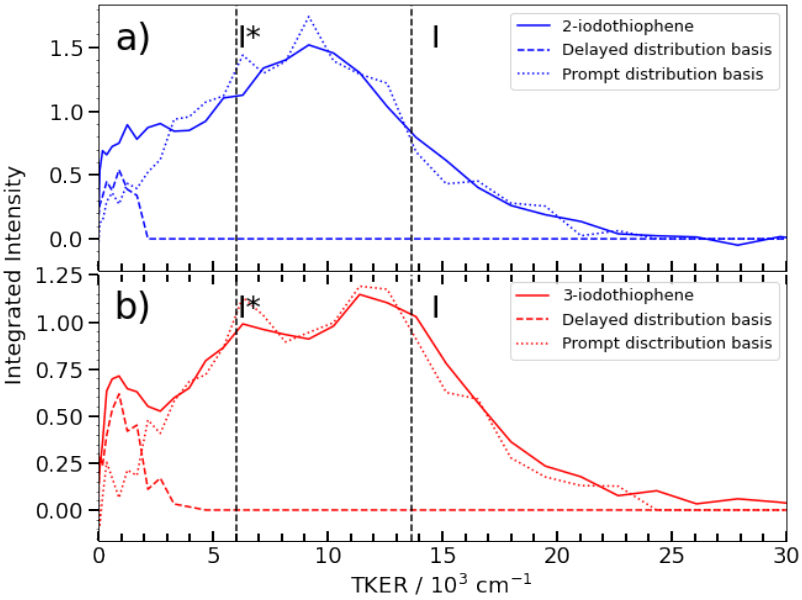

FIGURE 3.12: TKER distributions obtained from the I^{2+} asymptotic velocity distributions from 262 nm photolysis of (a) 2IT (blue) and (b) 3IT (red), assuming two-body dissociation into I + C_4H_3S. The dashed curves show the TKER distributions associated with the 'prompt' and 'delayed' dissociation channels (derived from the respective momentum basis functions), while the dashed vertical lines show the maximum TKER values associated with forming I and I* photoproducts, given $D_0(\mathrm{R-I}) = 24,500\ \mathrm{cm}^{-1}$.

Using the reported C-I bond strength in 2IT ($D_0(\mathrm{R}-\mathrm{I}) = 24,500\ \mathrm{cm}^{-1}$) [22], the maximum TKER ($TKER_{max}$) for the ground state I fragment was calculated using also via energy conservation rules:

$$TKER_{max} = E_{photon} - D_0(R-I) \tag{3.14}$$

where E_{photon} is the energy of the ionising photon (13.2 nm). The values of TKER produced by this calculation are shown by the rightmost dashed vertical lines in Figure 3.12. The equivalent $TKER_{max}$ value for forming spin-orbit excited iodine products (I*) is calculated by further subtracting the spin-orbit energy (E_{so} = 7603 cm^{-1}) from Equation 3.14[22]. This is shown as the leftmost vertical dashed line in Figure 3.12. Figure 3.14 shows intensity at TKER values above the calculated maximum, this is explained by a mixture of finite experimental resolution and the contribution of the Coulomb curve in the high TKER side.

The strength of the C-I bond in the 3IT isomer has not been previously reported, but previous studies of Br and Br* fragments arising from 267 nm photolysis of 2BrT and 3BrT have assumed identical C-Br bond lengths [23]. Moreover, recent threshold photoelectron studies of the furan anion (the oxygen analogue of bare thiophene) revealed essentially identical bond strengths for the alpha and beta C-H bonds [93]. In light of these studies, identical D_0 values were used for both 2IT and 3IT.

In panel b) of Figure 3.12, it is apparent that the TKER distribution following 262nm photolysis of 3IT peaks approximately 2500 cm^{-1} higher in energy compared to 2IT. The peak also appears more defined and is clearly divided into two maxima with a spacing consistent with the formation of both I and I* products. No such splitting is evident in the 2IT data. Previous research has revealed the formation of both I and I* photoproducts when 2IT is excited at similar wavelengths. Unlike the experiment presented in this chapter, the previous experiment was sensitive to the I or I* products separately. Thus, the difference can be explained by assuming that the partner ion in the photodissociation of the 2IT isomers is formed in a broader range of internal energy states. The present data for both isomers indicate a strong tendency to direct the UV photon energy in excess of that required for C-I bond fission into product translation, but they also show relatively greater internal excitation of the partner fragment in the case of 2IT photolysis.

3.4.6 Discussion of the dissociation dynamics

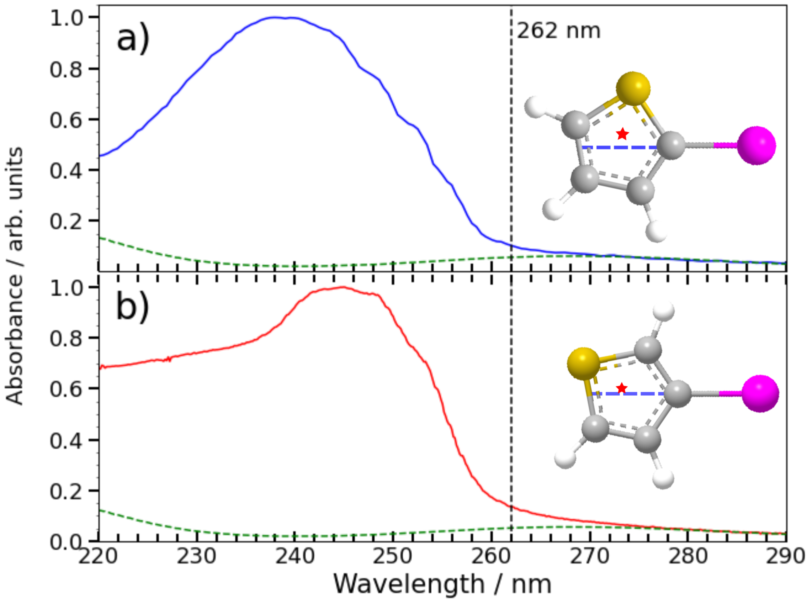

FIGURE 3.13: Gas phase absorption spectrum of 2IT a) and 3IT b) are plotted as solid lines along with a scaled absorption spectrum of CH_2BrI (dashed line) to emphasise the weak long wavelength absorption attributable to $n\sigma^*$ excitation in both 2- and 3-iodothiophene. The intensity scale has been normalized to the maximum measured for each isomer to show relative changes in the shape. The structure of the two isomers are plotted as insets with the C-I bond vector highlighted as a dashed blue line and the center of mass of the thiophenyl radical marked by a star. Measured by collaborator Felix Allum.

An in-depth understanding of dissociation dynamics requires knowledge of the number and nature of excited states that contribute to the parent absorption at the wavelength of interest. Although high-level calculations of potential energy surfaces are not currently available for these systems, an absorption spectrum can provide valuable insights in their absence. Figure 3.13 shows the room-temperature absorption spectra for 2IT and 3IT in panels a) and b), respectively. Each spectrum was normalised to its maximum absorbance. The spectrum of 2IT aligns well with that reported in a previous study [22]. The spectra of the two isomers are generally similar and can be viewed as a combination of two distinct types of excitation into: i) one or more directly dissociative $(n/\pi)\sigma^*$ states localised on the C-I bond, reminiscent of the A-band absorptions of alkyl iodides [98, 99]; and ii) a ring-centred, diabatically bound $\pi\pi^*$ state with significantly larger absorption cross-section, the potential energy surface (PES) for which favours ring expansion/distortion [22, 100].

To aid in visualising the contribution of $(n/\pi)\sigma^*$ excitations to the overall spectrum, a scaled version of the absorption spectrum of CH_2BrI is plotted in Figure 3.13 as a green dashed line. The spectrum of CH_2BrI functions as an illustrative example of the absorption envelope of $(n/\pi)\sigma^*$ states, which are observed in the A-bands of many alkyl iodides, and exhibit continuous absorption spanning approximately 40–50 nm (FWHM) with a Gaussian profile [98].

The CH_2BrI spectrum shows that the majority of the absorption at 262 nm is attributed to $\sigma^* \leftarrow (n/\pi)$ transitions. The populated states are repulsive with respect to the C-I bond expansion and have been previously correlated with I* products [22]; however, efficient nonadiabatic coupling to other $(n/\pi)\sigma^*$ states provides an efficient route for the production of ground state I products. This is consistent with the features observed within the data, namely, the high momentum I and I* products appear promptly with predominately parallel recoil anisotropy (consistent with direct excitation to a repulsive PES), and most of the photon energy in excess of that required for bond fission is released as product translational energy. The relatively greater internal excitation of the radical fragment from 2IT photolysis can be attributed to the increased product rotation. The structures of the two isomers are shown in the insets of Figure 3.13. The C-I bond vector is highlighted by a blue dashed line, and the centre of mass of the departing thiophenyl radical is marked with a star. From a simple ballistic point of view, the impulse from the recoiling I atom is expected to lead to higher rotational energy in the radical fragments from 2IT photolysis.

The $\sigma^* \leftarrow (n/\pi)$ transitions have not been considered in recent transient absorption spectroscopy studies on 2IT photolysis [24]. The supporting TD-DFT (focusing on singlet states only) presented in that study predicted that they should have negligible cross-sections [24]. However, the calculations revealed an efficient nonadiabatic coupling pathway between the $\pi\pi^*$ state and the $(n/\pi)\sigma^*$ continua, which in this chapter are thought to be responsible for the observed delayed low-momentum products. The $\pi^* \leftarrow \pi$ excitation facilitates ring bending motions, which are amplified during nonadiabatic coupling to the$(n/\pi)\sigma^*$ continua [24]. The observed delay of approximately 1 ps observed in the experiment is consistent with the TD-DFT calculations, and the activation of nuclear motions orthogonal to the C-I bond dissociation coordinate explains the lower product recoil velocities. The fact that the basis function used to describe the delayed dissociation peaks at a non-zero momentum is consistent with the eventual bond fission occurring on a repulsive potential energy surface. Comparing the absorption spectra of 2IT and 3IT, the red shift of the absorption maximum of 3IT suggests an increased relative contribution from $\pi^* \leftarrow \pi$, consistent with the greater relative yields of delayed dissociation products.

The findings of these studies lead to several conclusions. The absorption cross-sections for $\sigma^* \leftarrow (n/\pi)$ and $\pi^* \leftarrow \pi$ excitations depend on the wavelength of light used. At wavelengths greater than 262 nm, it is expected that the excitation of 2IT and 3IT will result in larger branching ratios owing to increased prompt dissociation. Photochemistry is predicted to be dominated by direct dissociation following excitation to one or more $(n/\pi)\sigma^*$ states, which leads to the formation of translationally excited I and I* fragments with anisotropic recoil velocities. Conversely, the cross-sectional area for $\pi^* \leftarrow \pi$ excitation should dominate at shorter wavelengths. Based on the current analysis, this should increase the relative yield of the delayed C-I bond fission channel, which is made possible by non-adiabatic coupling to the $(n/\pi)\sigma^*$ continuum and the formation of less translationally excited I and I* products. This predicted energy disposal is generally consistent with the imaging data for the dominant ground state I atoms in earlier nanosecond VMI studies on 2IT photolysis at shorter UV wavelengths [22]. Finally, comparisons with analogous thiophene and thiophenone photochemistry suggest that $\pi\pi^*$ excitation in 2IT and 3IT could also enable a rival ring-opening channel through nonadiabatic coupling to the ground state and subsequent dissociation of ”hot” cyclic or acyclic ground state molecules [25, 28, 30]. Such dynamics were not detected here. The current experiment was unable to observe bonding within the co-fragment. Furthermore, the 262 nm wavelength provides insufficient energy to induce both C-S and C-I bond fission without an H atom transfer within the initial biradical species [22, 24]. Nevertheless, the ring-opening process when exciting 2IT and 3IT at shorter wavelengths within the $\pi\pi^*$ absorption band is still a potential competing pathway worth investigating.

3.5 Conclusions

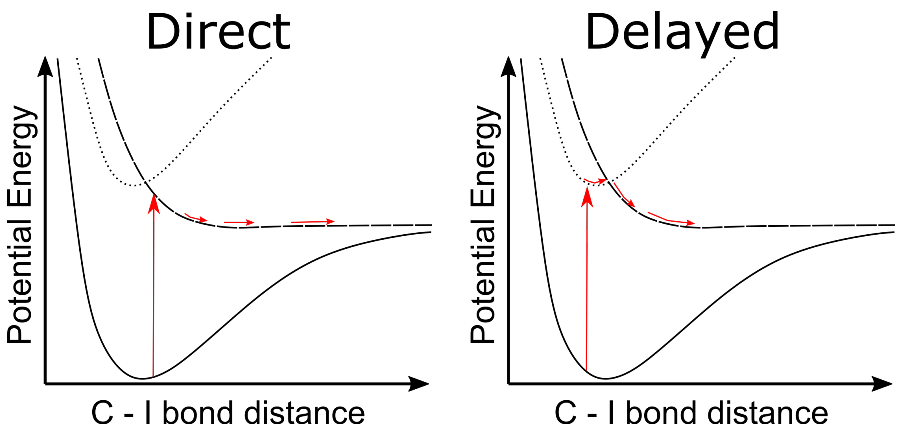

FIGURE 3.14: A schematic representation of the main PESs involved in photodissociation dynamics observed in 2IT and 3IT following excitation at 262 nm including: the ground state (solid line), the $(n/\pi)\sigma^*$ state (dashed line) and the $\pi\pi^*$ state (dotted line). Constructed with the aid of calculations from [22]. Proposed pathways as described in text marked by red arrows.

In this chapter, the fragmentation dynamics of 2IT and 3IT following excitation at 262 nm were investigated through time-resolved VMI measurements following site-selective XUV ionisation at the I 4d edge. Two C-I bond fission channels were identified in both the isomers, for illustration they are represented on the schematic interpretation of iodothiophene PES in Figure 3.14. The dominant process in both cases at this wavelength is direct dissociation, yielding transitionally excited I atom fragments with anisotropic recoil velocity distributions. The second, relatively weaker channel, involves the delayed formation of iodine fragments with an isotropic and much lower momentum distribution. Energy conservation requires the radical fragment arising via this second channel carries a much higher level of internal energy. The relative importance of the delayed channel was found to be greater in the case of the 3IT isomer.

The dominant process in both isomers was assigned to direct dissociation following excitation to one or more repulsive $(n/\pi)\sigma^*$. This excitation is represented by a vertical red line in Figure 3.14 under the "direct" heading, following excitation the molecule quickly dissociates along the negative gradient of this initially excited surface. The photolysis data of 3IT clearly demonstrated the formation of translationally excited I and I* products, as previously observed in nanosecond studies of 2IT at similar wavelengths [22]. The ultrafast appearance time of these prompt products agrees well with that determined in a recent transient XUV absorption study of 2IT photolysis at 268 nm [24]. The present findings confirm that 262 nm excitation of both 2IT and 3IT populates one or more $(n/\pi)\sigma^*$ PESs directly, contrary to the conclusions reached in the recent 268 nm ultrafast transient absorption study [24]. It is worth noting that the absorption study was less sensitive to the appearance of the delayed component, which can be identified here. This is because the two channels are strongly overlapped spectroscopically, and the much weaker delayed dissociation signal is likely overshadowed by the dominant direct dissociation. These limitations are not present in the experiment described in this chapter as it examines the two significantly different KEs of the products generated through the proposed mechanisms. The alternative mechanism suggested in this study, which involves initial excitation from the π to π^* state followed by efficient nonadiabatic coupling to the $(n/\pi)\sigma^*$ continua, is inferred to be responsible for the observed delayed channel and is visualised in Figure 3.14 under the "delayed" heading. The significance of these two channels is predicted to vary considerably with excitation wavelength. The latter process is expected to be dominant at shorter wavelengths, where the parent absorption is primarily attributed to $\pi^* \leftarrow \pi$ transitions, but may compete with the unimolecular decay of "hot" ground state species resulting from radiationless transfer driven by ring-opening or ring-puckering motions in the photoexcited parent molecule, as observed for bare thiophene and thiophenone [25–30].

Chapter 4

Time-resolved X-ray Scattering Study of Iodothiophene Dissociation Dynamics

4.1 Introduction

Time-resolved X-ray scattering (TRXS) is a highly effective method for probing the structural dynamics of molecules at ultrafast timescales [101, 102]. This technique utilises the ability of X-rays to penetrate matter and interact with electronic clouds of atoms. This allows for a detailed examination of the molecular configurations and their temporal evolution. TRXS is structural probe that is sensitive to changes in bond lengths rather than fragment kinetic energies as discussed in the previous chapter.

The X-ray scattering experiment described in this chapter was performed at one of the leading facilities for TRXS, the Linac Coherent Light Source (LCLS), located within the SLAC National Accelerator Laboratory in the United States [37, 103]. LCLS is widely known for its capacity to deliver extremely bright and coherent X-ray pulses, making it ideal for conducting time-resolved studies. The objective of applying TRXS to the study of iodothiophene photodissociation dynamics is to gain insights into the structural rearrangement of the molecule following excitation with a UV photon. TRXS has the potential to observe geometry changes associated with prompt C-I bond fission as well as signatures of the suspected C-S bond expansion, indicative of ring-opening dynamics, as previously postulated in the scientific literature [22–24].

The pump–probe technique is again employed, with X-ray scattering serving as the probe. The target molecule, 2-iodothiophene (2T), is excited from its ground state to an excited state using a 252 nm ”pump” laser. Following a specified time delay, the ”probe” pulse of 15 keV photons is incident on the sample, and the resulting scattering pattern is recorded. By recording the scattering patterns at various pump-probe time delays, a ”molecular movie” of the dynamics following excitation can be constructed.

The pump wavelength used in this chapter is shorter and, therefore, has higher photon energy than that employed in the previous chapter. Excitation using a 252 nm photon is close to the peak absorption into the $\pi\pi^*$ orbital. As speculated in the last chapter, the two channels observed in the photodissociation of iodothiophene arise from the excitation into superposition of both $(n/\pi)\sigma^*$ and $\pi\pi^*$ orbitals. Dissociation from the $(n/\pi)\sigma^*$ excited potential energy surface is prompt, with the iodine product carrying most of the energy in excess of that required for bond breaking as translational energy. In contrast, the $\pi\pi^*$ excited state surface is not directly dissociative, and eventual bond fission is presumed to occur following nonadiabatic coupling to dissociative $(n/\pi)\sigma^*$ states. This results in delayed formation of iodine fragments which carry significantly less translational energy. Exiting 2IT with a 252 nm photon is expected to increase the yield of the latter channel due to increased absorption cross-section into the $\pi\pi^*$ state. This could be beneficial in the analysis of the data. The two pathways result in the fission of the same bond, therefore the pump-probe signal associated with each channel will appear in the same region of the recorded spectrum. The increased contribution from $\pi\pi^*$ dissociation may make the signatures of the minor channel more easy to distinguish on top of the dominant $(n/\pi)\sigma^*$ pump-probe signal.

4.1.1 Principles of X-ray scattering

When an X-ray photon is incident on an atom, it has the potential to be scattered by an electron within the atom’s electron cloud. The incident X-ray photon possesses a sinusoidal electromagnetic field. As the photon approaches the atom, its electromagnetic field exerts a force on the electrons within the atom. Since electrons are charged particles, they respond to this electric field component of this field by oscillating at the same frequency as the incident X-ray photon. This interaction results in the formation of an oscillating dipole within the atom [104].

As the dipole continues to oscillate, it re-emits the absorbed energy in the form of scattered electromagnetic radiation. This scattered radiation can vary in direction and energy relative to the original incident X-rays, depending on the specific interactions that occur within the atom. The scattered X-rays contain valuable information about the structure of the molecule they have interacted with, as the pattern of scattering is directly influenced by the spatial arrangement of atoms within the molecule. By analysing the intensity and angular distribution of the scattered X-rays, information about the atomic and molecular structure of the target species can be inferred. This process allows for the reconstruction of the three-dimensional arrangement of atoms, providing insights into the molecular geometry and electronic environment [104].

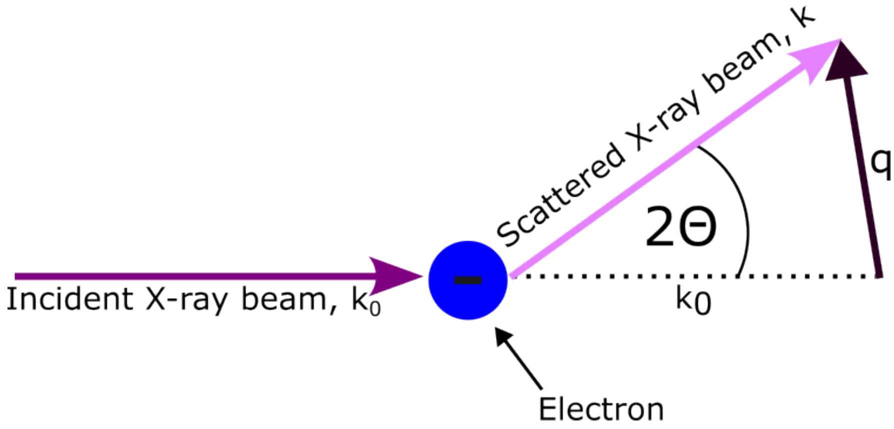

FIGURE 4.1: A schematic representation of an incident x-ray beam being scattered by an electron within an atom's electronic cloud.

4.1.2 Elastic scattering

Elastic scattering is a process that involves a completely elastic collision, where no energy is transferred from the photon to the electron. This scattering mechanism is often referred to as Thomson scattering. The scattered photon has the same energy as the incident photon, but its direction of propagation is altered.

Thompson scattering is predominantly observed when the energy of the X-ray photon is significantly higher than the binding energy of the electrons in the atom. In such cases, the electrons are not excited to higher energy levels or ejected from the atom, allowing the X-ray photon to scatter without energy loss. The process of Thomson scattering is illustrated pictorially in Figure 4.1. The figure depicts an incident X-ray beam approaching an atom, interacting with one of its electrons, and subsequently being scattered in a different direction. The angle between the incident and scattered X-rays is traditionally denoted as 2θ in TRXS experiments [104].

The change in momentum following scattering, marked by an arrow in Figure 4.1, is commonly represented as the momentum transfer vector q,

$$q = \frac{4\pi}{\lambda} sin\theta \tag{4.1}$$

where λ is the wavelength of the incident X-ray beam.

The intensity of elastic X-ray scattering from a single free electron is given by the Thomson scattering equation [104–106]:

$$I_e = I_0 \frac{e^4}{m_e^2 c^4 R^2} \alpha_{pol} \tag{4.2}$$

where I_e and I_0 are the intensities of the incident and scattered radiation, respectively, e is the charge of an electron, m_e is its mass, c is the speed of light and R is the distance between the scattering origin point and the point of detection. The term α_{pol} is determined by the polarization of the incident laser beam [104]. For a linearly polarised X-ray source, such as the one employed in the experiment described in this chapter, the polarization term is defined as:

$$\alpha_{pol} = sin^2\phi + cos^2\phi cos^2 2\theta \tag{4.3}$$

where ϕ is the azimuthal angle (of detected photon relative to laser polarization), and 2θ is the angle of momentum transfer of the scattered radiation relative to the incoming beam [105].

Thus far, these equations describe scattering by a single electron. To describe the scattering from a multi-electron atom, the spatial distribution of the charge density, $\rho(r)$, must be considered. The process of scattering is described by atomic form factors, f, which represent the Fourier transform of the electron density distribution, $\rho(r)$, around an atom:

$$f(q) = \int \rho(r) e^{iqr} d^3 r \tag{4.4}$$

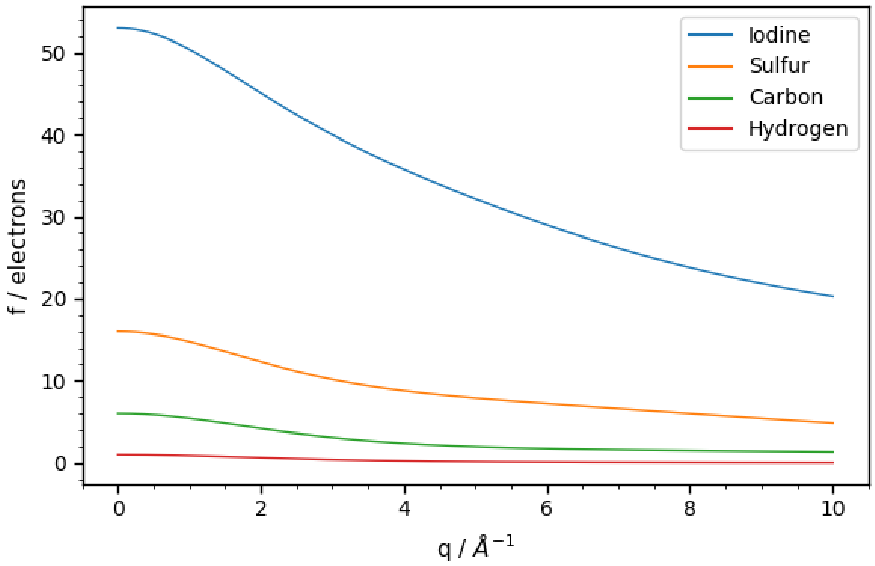

FIGURE 4.2: Theoretical form factors of iodine (blue), sulfur (orange), carbon (green), and hydrogen (red).[107]

where q is the scattering vector, and $\rho(r)$ is the electron density at position r within the atom. The value of $\rho(r)$ depends on the electronic structure of an atom. Determination of electronic structure requires complex mathematical calculations and significant computational resources, making the determination of form factors a challenge. However, for practical use, the atomic form factors for all atoms in the periodic table are tabulated based on experimental data and theoretical calculations derived from relativistic wavefunctions. The form factors of the atoms present in 2IT have been plotted in Figure 4.2[107].

4.1.3 Inelastic scattering

In inelastic scattering, the incident X-ray photon transfers part of its energy to the electron, resulting in a scattered photon with a lower energy compared to incident radiation. This phenomenon was extensively studied by A.H. Compton in 1923; thus, this process become known as Compton scattering. During inelastic scattering, when an X-ray photon collides with an electron, it imparts some energy to the electron, causing the electron to be ejected or elevated to a higher energy state. Consequently, the scattered photons have reduced energy (and a longer wavelength) compared to the incident photons. The extent of this energy loss (and the corresponding scattered photon wavelength increase) depends on the angle at which the scattering occurs. This angle is crucial because it directly influences the amount of energy transferred from a photon to an electron. Compton's equation mathematically describes the relationship between the change in the wavelength $\delta\lambda$ of the scattered photons and scattering angle θ. The equation is given by:

$$\Delta\lambda = \lambda' - \lambda = \frac{h}{m_e c}(1 - cos\theta) \tag{4.5}$$

where λ and λ' are the wavelengths of the incident and scattered photons, respectively, h is Planck's constant, m_e is the mass of an electron and c is the speed of light.

In contrast to elastic scattering, in which scattered waves can interfere constructively or destructively to produce a pattern, Compton scattering is inherently incoherent. Inelastic scattering events are independent of each other and do not produce a coherent interference pattern; therefore, they do not contain structural information. The magnitude of inelastic scattering is influenced by several factors such as the total number of electrons, X-ray wavelength, and q range being investigated. Relative to elastic scattering, inelastic scattering is more significant for heavier atoms which have more electrons [108].

Similar to elastic scattering, in which the atomic form factor $f(q)$ is used to describe the scattering amplitude as a function of momentum transfer, total incoherent scattering from an atom is commonly approximated using an interpolated form factor S_i [107].

4.1.4 Scattering from molecules

Scattering from a molecule is often described using the Independent Atom Model (IAM). The IAM treats the molecular electron density as the sum of the electron densities of individual atoms. In this model, the complex electron cloud of a molecule is approximated by considering each atom independently, and then summing their individual contributions. This simplification allows the molecular form factor, which describes how the molecule scatters X-rays, to be approximated as the sum of atomic form factors.

For a gas of molecules, the detected scattering pattern is the sum of scattering from many randomly oriented molecules. Because the molecules in the gas phase are free to rotate and translate, their orientations with respect to the incident X-ray beam are random. Therefore, the observed diffraction pattern is the average of all the possible orientations of the molecules. This randomness must be considered to accurately interpret the scattering data.

In the IAM model there are several components that contribute to the total scattering pattern. The individual atoms produce patterns, but there are also interference terms related to the separation of atoms. In analysis of this experiment, this is limited to include only the pairwise interference term that can be described by the Debye's scattering equation [104, 109]:

$$I(q) = \sum_{i \neq j}^{N_{atom}} f_i(q) f_j(q) \frac{sinqr_{ij}}{qr_{ij}} \tag{4.6}$$

where $I(q)$ is the scattering intensity as a function of the scattering vector q; f_i and f_j are the atomic form factors of atoms i and j,respectively; r_ij is the distance between them; and N is the total number of atoms in the molecule. This equation provides a method to calculate the intensity of scattered X-rays based on known distances between pairs of atoms within a molecule. It considers the interference effects that arise from the different possible orientations of the molecules in the gas phase, leading to an averaged scattering pattern that can be compared to experimentally observed data [104, 109].

The IAM omits the effect of binding on the electron density distribution of valence electrons; this would be particularly impactful for small molecules, where the number

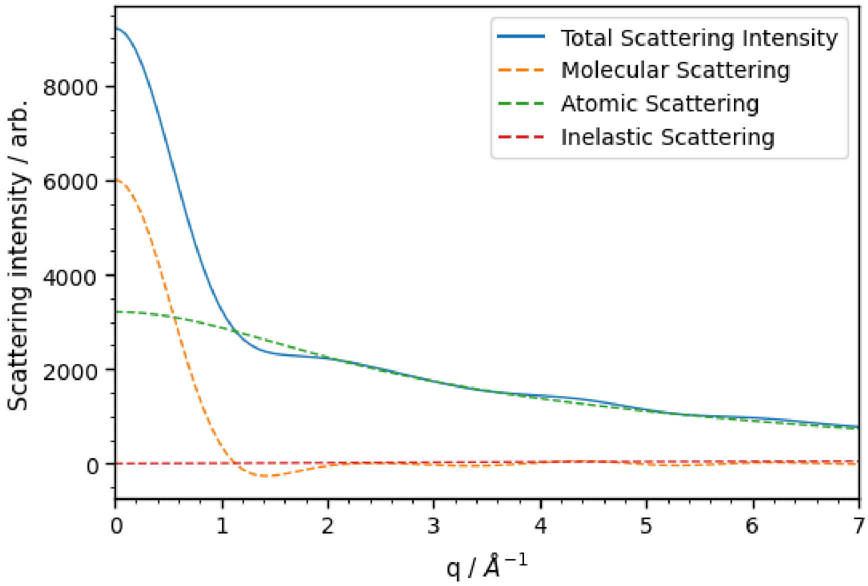

FIGURE 4.3: Theoretical scattering pattern for 2IT calculated using Equation 4.1.4, showing the total scattering pattern (blue solid line) as well as the molecular (orange), atomic (green), and inelastic (red) scattering components as dashed lines. The atomic scattering patterns are taken from Ref. [107]

of valence electrons forms significant portion of the overall number of electrons in the molecule. In many cases, the number of core electrons, which are minimally perturbed by binding interactions, greatly outnumbers the number of valence electrons, and the approximation has been shown to produce a good match to experimentally observed data [110, 111]. This equation illustrates that the scattering intensity is influenced by the distance between all pairs of atoms within the molecule, weighted by their respective form factors. The sine term accounts for the phase differences between scattered waves owing to different atomic separations, and the division by qr_{ij} ensures that the intensity is properly scaled with the distance and scattering vectors.

The overall observed scattering pattern is the result of the combined effects of atomic, molecular and inelastic scattering:

$$I_{tot}(q) = \sum_{i}^{N_{atom}} |f_i(q)|^2 + \sum_{i \neq j}^{N_{atom}} f_i(q) f_j(q) \frac{sinqr_{ij}}{qr_{ij}} + \sum_{i}^{N_{atom}} S_{inel,i}(q) \tag{4.7}$$

where $I_{tot}(q)$ is the total observed scattering from a molecule, $f_i(q)$ is the scattering form factor of the ith atom and r_{ij} is the distance between atoms i and j. The term $S_{inel,i}(q)$ denotes the inelastic scattering contribution of atom i. The first term of this equation is atomic scattering, whereas the second term is molecular scattering. Because of the $sin(qr_{ij})$ relationship of the scattering intensity with the interatomic distance, it can be deduced that large interatomic separations will contribute high-frequency patterns to the overall scattering and vice versa for short distances.

Contributions from each component to the overall scattering spectrum of 2IT are shown in Figure 4.3 where the calculated patterns for the ground state equilibrium structure of 2IT are plotted. It can be seen that the major component of the overall scattering pattern is the atomic scattering, the molecular component adds an oscillation on top of otherwise smooth atomic scattering curve. As 2IT is a relatively heavy molecule the inelastic scattering component has a small but, as shown in a later section, significant contribution.

4.2 Experimental Details

The specifics of the experimental apparatus used in this Chapter are introduced in Chapter 2. The objective of this section is to outline the primary parameters used in the experiment presented in this Chapter.

The experiment was performed at the Coherent X-ray Imaging (CXI) instrument at the Linac Coherent Light Source. X-ray pulses were generated at a repetition rate of 150 Hz, with an estimated duration of 30 fs and energy of 15 keV. The shot-to-shot X-ray pulse energy was measured outside the vacuum chamber using x-ray photodiodes [103].

The generation of UV pump pulses (252 nm) was achieved through hollow-core fibre based Four-Wave Mixing source [112]. The resulting UV pulses were focused using a 350 mm focusing lens and delivered collinearly with the X-rays.

The time delay between the UV and X-ray pulses was controlled using a motorized optical delay stage. The pump-probe delays were systematically scanned from -2 ps to 2 ps in variable step sizes. At LCLS the optical laser systems are locked into the radio-frequency (RF) that dictates the accelerator's electron pulse, and so the time zero of the X-ray and UV laser systems is achieved through RF feedback technique which provides sub-picosecond stability [113].

The arrival time of x-ray and therefore the discrepancy of the optical and x-ray pulses on a shot-to-shot basis, is called "timing jitter" and can be attributed to thermal changes in the accelerator and noise in the RF system [114]. Shot-to-shot jitter is measured using a Spectral Encoding Time-tool which reduces uncertainty to approximately 10 fs. To obtain this timing correction a fraction of the optical laser light is picked off by a beamsplitter upstream of the interaction region. A white light ps pulse is generated in a sapphire substrate concurrently with the pump laser. The white light is then transmitted through a thin film of silicon nitrite (Si_3N_4) and dispersed with a diffraction grating on the other side before being captured on a camera. When the film absorbs the arriving x-ray photon, its refractive index changes which generates an edge in the white light power profile (in time, and therefore also spectrally due to the chirp). The edge will move back and forth on the camera depending on the relative time delay between the pump laser and X-rays. In this way, the time-delay for each collected frame of scattering pattern can be collected [115].

A gas cell was used in this experiment for sample delivery. The 2IT gas was delivered to the cell by placing liquid 2IT in a bubbler and delivering to the cell without using a seed gas. The flow rate was computer-controlled. The gas cell had a beryllium out-coupling window to minimize absorption and re-scattering of scattered X-rays.

The scattered X-rays were detected with a Jungfrau hard X-ray pixel detector with a pixel size of 75 μm, operating in high-gain mode, situated approximately 8 cm behind the gas cell. The Jungfrau detector operates by detecting the charge generated when high-energy photons interact with its silicon sensor. Each photon creates electron-hole pairs in the sensor, with the number of pairs being proportional to the photon energy. The detector processes the collected charge and converts it into a digital signal, with the charge amplitude providing information about the photon's energy [116]. The raw images are thresholded to eliminate detector noise and X-ray hits were then identified and localized within a 2x2 pixel area. Only pixels with energy close to that of the incoming x-ray beam were selected to avoid hits from fluorescence photons.

4.3 Data Treatment

4.3.1 FEL fluctuations

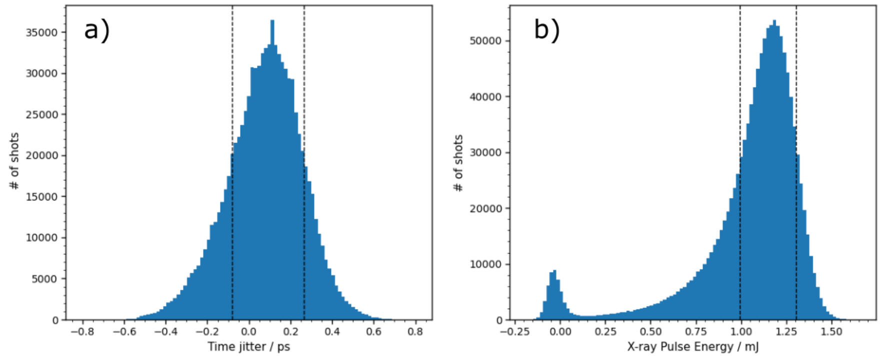

FIGURE 4.4: A histogram of a) FEL arrival time jitter and b) FEL pulse power of all shots recorded as part of the dataset. Dashed vertical lines mark the subset of data chosen for further analysis.

The first step in the data analysis workflow is to select the subset of data to be analysed based on the relevant metadata that has been gathered. This helps mitigate any intensity artefacts caused by the inherent instability of FEL radiation.

In a manner similar to that described in the previous chapter, the data were selected based on the FEL power and arrival time jitter values on a shot-to-shot basis. The histograms of the arrival time jitter and FEL power for all shots collected during the experiments are shown in panels a) and b) of Figure 4.4, respectively. The arrival time jitter has a Gaussian distribution, and shots were discarded if their value was outside one standard deviation of the mean, marked by dashed vertical lines in Figure 4.4. On the other hand, the FEL power shows a double Gaussian distribution, with some intensity centred around 0. This indicated that some shots were recorded without X-rays because of a brief interruption in the lasing of the FEL. A Gaussian was fitted only to the peak centred away from zero, and shots where the power was outside one standard deviation of the mean were excluded, also marked by dashed vertical lines.

Once the dataset for analysis was selected, a time correction of the nominal pump-probe delay times was performed on a shot-to-shot basis according to :

$$t = t_{nominal} + t_{jitter} \tag{4.8}$$

The data was then sorted into 25 fs bins in the range of -200 fs to 1 ps. Each time bin was normalised to the total FEL power. During the experiment a nominal time zero is used which allows the desired experimental time ranges to be selected. The absolute value of time zero is later obtained through fits of the experimental data (Section 4.4.3).

4.3.2 Image integration

The three dimensional scattering patterns collected during the experiment were radially averaged to produce two-dimensional curves as part of the LCLS data acquisition process. This is appropriate as the structural information is encoded in a radially symmetric manner due to the random orientation of molecules in the gas phase. Radial averaging simplifies the data, which facilitates its interpretation, and it also helps to reduce noise, thus enhancing the clarity of the resulting patterns.

Multiple masking filters were applied to the images before radial averaging to enhance the signal-to-noise ratio. To create these masks, additional images were captured throughout the course of the experiment. This included a ”dark image,” which is an image obtained without any laser pulses in the interaction chamber. It serves as a baseline measurement for the inherent electronic and thermal noise generated by the detector itself. These signals may originate from sources such as dark current, which is a small amount of current that flows through the detector even in the absence of light, and readout noise, which occurs when the signal is read from the detector. The dark image was subtracted from the images in the pump-probe dataset.

The second mask is used to eliminate pixels containing high photon counts that are unrelated to molecular scattering. These high counts can be caused by various factors, such as stray light, reflections, or burnt out pixels, which do not provide any meaningful information regarding the molecular structure under investigation. To create this mask, a control image was obtained by directing both laser pulses into the interaction chamber without any sample gas present. This image captures the background signal and any external sources of photons that could interfere with the accurate measurement of the scattering data, which is generally much weaker. If these ”hot” pixels were included in the radial average, the true value of the scattering intensity can be significantly distorted. Therefore, pixels with significantly higher counts relative to their surrounding pixels (typically orders of magnitude higher) are identified and masked in all images collected.

4.3.3 Detector Geometry Calibration

To express the data as a function of the momentum transfer vector q defined by the equation 4.1, it is necessary to determine the distance and position of the detector relative to the interaction point. This can be achieved by comparing a well-known scattering pattern with detected data. Using trigonometry, the scattering angle θ is related to the momentum transfer vector q according to[117]:

$$\theta = tan^{-1}\left(\frac{\sqrt{(x-x_0)^2+(y-y_0)^2}}{z_0}\right) \tag{4.9}$$

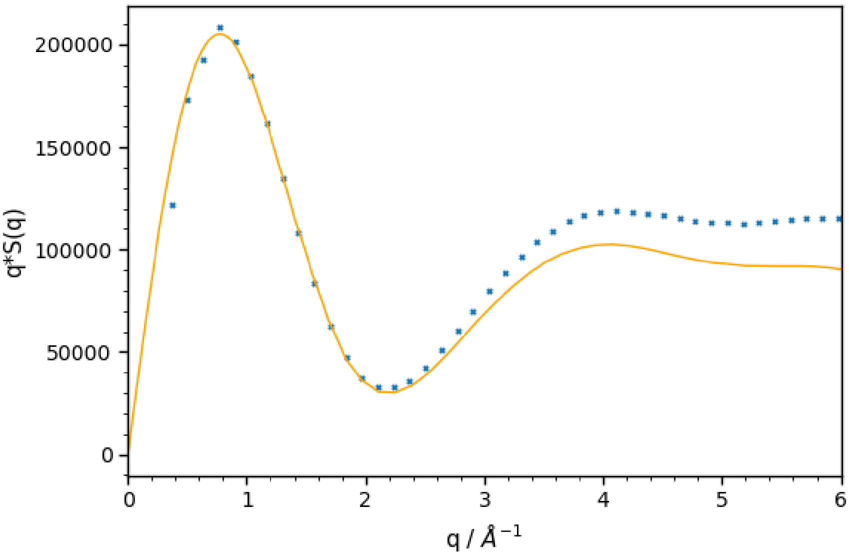

FIGURE 4.5: Scattering pattern of ground state of SF_6 calculated using the IAM (solid orange line) and the experimental scattering pattern (blue crosses) used to calibrate the detector position as desribed in text. Both patterns are multipled by momentum transfer vector q to improve visibility at large q values.

where x and y refer to the coordinates of the pixel where a scattered photon is detected, and the detector centre has coordinates x_0 and y_0. The distance from the scattering point to the detector is denoted by z_0.

The geometry of the detector was precisely calibrated by collecting and fitting a static scattering signal from sulfur hexafluoride (SF_6) to the expected scattering pattern, which included both the elastic and inelastic components, calculated using the IAM. SF_6 was chosen because of its well-known structure and the clear scattering pattern it produces [118]. The difference between the expected and collected patterns was minimised using a least-squares fitting algorithm, with x_0, y_0 and z_0 as the fitting parameters, the calculated and fitted patterns are shown in Figure 4.5. The positional stability of an X-ray beam is greater than 10 μu [37]. This is more than seven times smaller than a single pixel of the detector; therefore, a single determination of the centre position is sufficient for all frames.

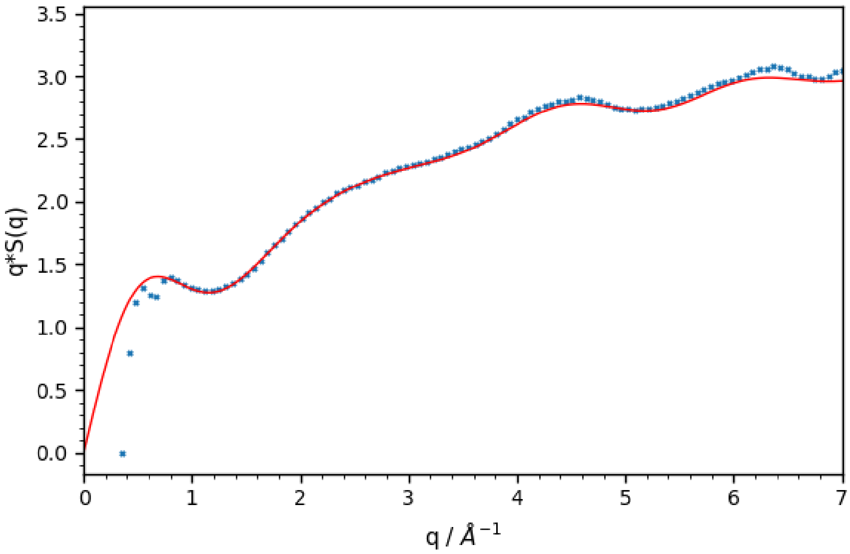

FIGURE 4.6: Scattering pattern of ground state of 2IT calculated using the IAM (solid red line) and adjusted for Compton Scattering, and the experimental scattering pattern (blue crosses). Both patterns are multiplied by momentum transfer vector q to improve visibility at large q values.

The accuracy of the calibration was verified by comparing the theoretical and observed static scattering patterns of 2IT, as shown in Figure 4.6. These 2IT static scattering patterns were collected using the FEL laser in absence of UV light. The IAM model was used to calculate the expected patterns. The curves show exceptional agreement which validates the precision of the calibration process but also reinforces the validity of the IAM model when applied to 2IT.

4.4 Results

4.4.1 Dynamics Scattering Results

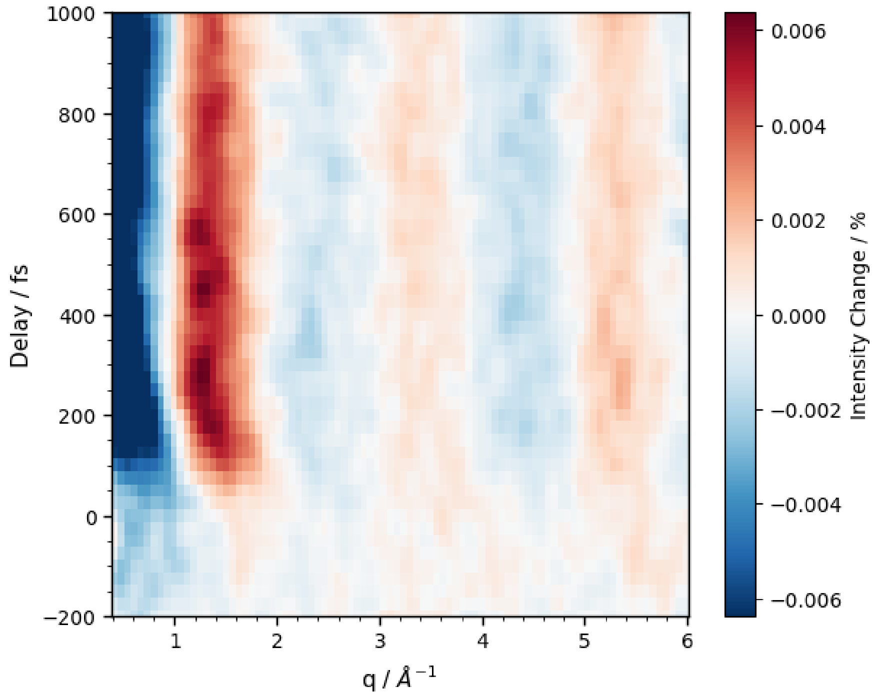

FIGURE 4.7: Time-resolved difference map of scattering intensity as a function of the momentum transfer, q, and pump-probe delay (fs) following excitation by a 252 nm photon.

The changes in scattering patterns following molecule excitation in time-resolved experiments are best represented by calculating difference scattering patterns. These are obtained by taking a difference between the pattern of the ground state and the scattering pattern collected at each pump-probe delay point. The ground state scattering pattern was collected by setting the UV laser to arrive several ns after the X-rays, this was done for approximately every 7th laser shot throughout the experiment. Calculating the difference spectra makes the small changes caused by UV excitation easier to distinguish, however it also removes artifacts caused by systematic errors such as uneven gain across the detector or scattering from background gases. In TRXS experiments it is common to express the difference pattern as a percentage:

$$\Delta S(q,t) = 100 * \frac{S(q,t) - S_{off}(q)}{S_{off}(q)} \tag{4.10}$$

where $S(q,t)$ is the total recorded scattering pattern, $\Delta S(q,t)$ is the difference scattering pattern both as a function of momentum transfer q and pump-probe time delay t. $S_{off}(q)$ is the scattering pattern of the ground state molecule. The experimental percent difference spectrum is shown in Figure 4.7.

In Figure 4.7, the red areas indicate an increase in scattering intensity in comparison to the ground-state molecule, while the blue areas represent a decrease. After the time-zero point, when the UV and X-ray pulses temporally overlap, a distinct pattern emerges. The first prominent depletion is centered at $\sim$ 0.5 Å^{-1} and the first enhancement is visible at $\sim$ 1.4 Å^{-1} . Unlike spectroscopic methods, these changes are not independent and do not represent distinct depletions and enhancements. Each pair of atoms contributes a sinusoidal component to the overall scattering. An increase or decrease in the bond length, manifests as a change in amplitude of the sinusoidal component in the difference pattern. The observed oscillatory pattern is the sum of the sine wave scattering patterns resulting from all the changing bond lengths with respect to the ground state molecule.

The observation of a negative feature at low q values signifies a decrease in the amplitude of the scattering pattern with respect to the ground-state pattern. This is consistent with geometry changes within the molecule following excitation with UV light; for example as molecules undergo photolysis, there are fewer of them to produce the ground state pattern. A second characteristic of the spectrum indicative of dissociation is the shift of the peaks towards lower q values observed in the first 200 fs. Because the relationship between momentum transfer and bond length is proportional to the sine function $sin(qr_{ij})$, peaks in the scattering pattern that shift towards lower q are indicative of bond length increases. The shift was examined by tracking the zero-crossing point between the first observed depletion and the first enhancement. The zero-crossing shifts by 0.38 Å^{-1} and reaches an asymptotic position after 300 fs. Although the change in bond length cannot be directly estimated from these values, as the overall pattern is a superposition of all structural changes, it is worth noting that the time taken to reach the asymptotic distance is similar to the appearance times seen in the preceding chapter for the ”prompt” dissociation channel.

4.4.2 Frequency-resolved spectrum

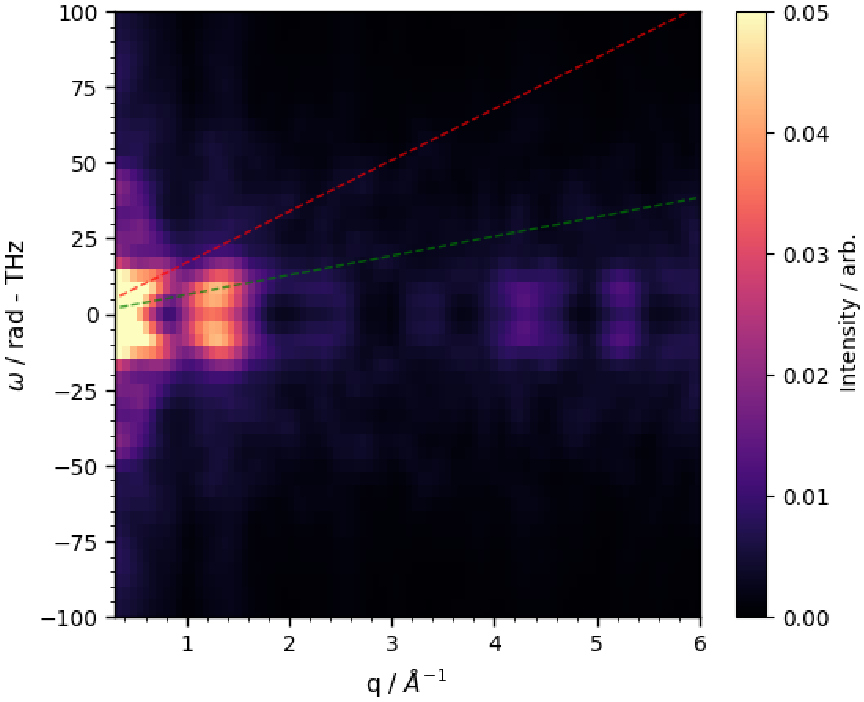

FIGURE 4.8: FRXS representation of the TRXS data in the range $-200 < t < 1200$ fs. The dissociation velocities calculated through the Hough transform approach described in text are marked as dashed lines for 6.42 Å/ ps (green) and 16.95 Å/ ps (red).

Information related to nuclear motion in a TRXS spectrum is distributed in q and t. To differentiate between various components, the data can be analysed using a Fourier transform along the time-delay axis. This analysis technique is commonly referred to as frequency-resolved X-ray scattering (FRXS), in which the spectrum is plotted as a function of q and frequency ω. In the FRXS spectrum, constant-frequency molecular vibrations appear as horizontal lines, while dissociations manifest as slanted features. The precise positions of these features can provide information about the constants of motion, such as vibrational frequency and final dissociation velocity [101, 119, 120]. The FRXS spectrum of the TRXS data derived from scattering from photoexcited 2IT is shown in Figure 4.8.

The extraction of the time-averaged dissociation velocity from the FRXS spectrum involves determining the gradient of the slanted feature indicative of dissociation. This slanted line is defined by the first-order polynomial equation:

$$\omega = q \times v \tag{4.11}$$

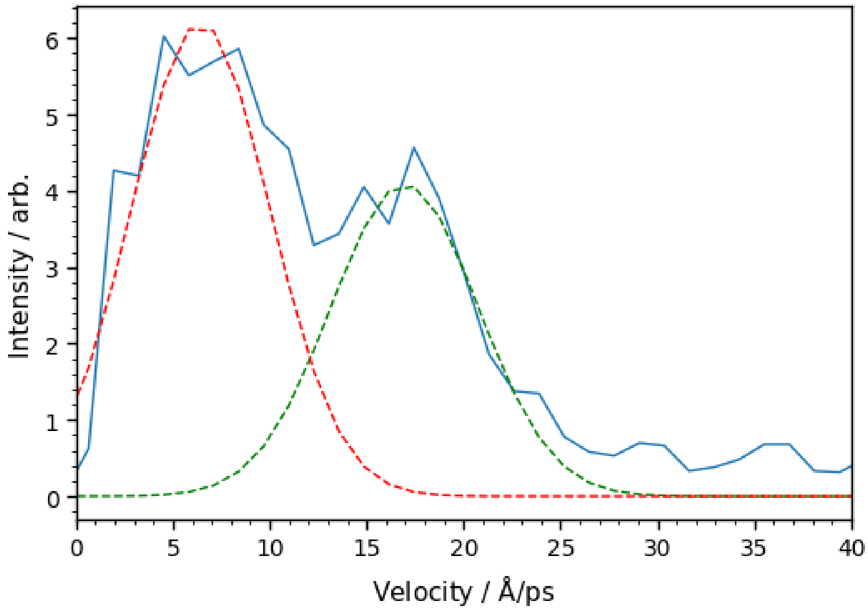

FIGURE 4.9: Velocity - resolved Hough transform taken for y-intercept $v_0 = 0$ (blue solid line). The gaussian fits used to describe the two dissociating pathways peaking at 6.42 Å/ ps (red) and 16.95 Å/ ps (green) are shown as dashed lines.

The dissociation velocity v can then be obtained by identifying large-amplitude lines in the spectrum that pass through the origin $q = \omega = 0$ [119, 120]. Previously, this was typically achieved by picking the bright lines by eye; however, recently, a Hough transform-based process has been shown to be an effective technique capable of achieving this automatically [101, 120]. This technique also allows for the extraction of dissociation velocity ranges, as opposed to isolated values. This approach maps bright lines from the input spectrum to a 2D curve of the intensity against the dissociation velocity by taking the line integrals of the spectrum. This is presented in Figure 4.9. The lines are defined by Equation 4.11, and scan a range of v values. The Hough transform method should be used cautiously because it has several limitations that need to be considered. This is most reliable for dissociations with narrow distributions, resulting in clearly defined lines in the FRXS spectrum. However, when broad features overlap, the transform may overestimate the distribution width associated with each feature. The accuracy of the Hough transform also decreases when investigating predissociation dynamics, which occur when a molecule is excited to a bound state that non-adiabatically couples to a dissociative state, as expected in 2IT. The shift in the dissociation time of a specific pathway influences the phase intensity within the FRXS data [120]. The phase variation of the dissociation line for a pathway with a dissociation time shift of t can be calculated using equation e^{iwt} [101, 120]. When the dissociation is not prompt and occurs at a range of pump-probe delay times, the FRXS intensity along that specific dissociation line is averaged over the phase, reducing the visibility of the line in the FRXS data as ω increases. Signal suppression has been shown to be manageable for pre-dissociation timescales of a few hundred femtoseconds or less. This also means that the intensity obtained using this approach is not reflective of the yield of the pathway [120].

Nevertheless, this approach provides a useful tool for the analysis of 2IT, particularly in the absence of detailed trajectory calculations which are commonly used to interpret scattering data. Although branching ratios cannot be directly inferred from these data, the dissociation velocities and their distribution can be used to construct a simple mechanical dissociation model. The Hough transform spectrum as shown in Figure 4.9, possess two main peaks at 6.42 Å/ ps and 16.95 Å/ ps.

4.4.3 Data Fitting

A straightforward mechanical model of structural changes was applied to further investigate the data. After UV excitation, the C-I bond was extended, while the structure of the co-fragment remained unchanged. The structures expected along the dissociation pathway are not currently known, and to maintain simplicity and avoid confirmation bias, the thiophene ring fragment was assumed to remain unchanged.

The results of the Hough transform were used to model the velocity distribution at which the I atom product recoils. A Gaussian distribution of dissociation velocities was assumed for each channel and their sum was fitted to the Hough transform spectrum. The individual Gaussian components are shown in Figure 4.9 as dashed lines. This approach yielded mean dissociation velocities of 6.42 Å/ps and 16.95 Å/ ps along with the standard deviations of 3.58 Å/ps and 3.79 Å/ps for the fast and slow channels, respectively. To create the simulated spectra, the Gaussian distributions were normalised to their maximum values. This allows the relative contribution of each channel to be calculated in a subsequent fitting step. A separate simulated dataset was calculated for each dissociation channel. For each channel, Gaussian profiles from the Hough transform were sampled at 0.5 Å/ps intervals. A spectrum was created for each sampled dissociation by calculating a scattering pattern (using IAM) at pump-probe delays matching the experimental data. The final spectrum for each channel was determined as the weighted sum of the spectra at each sampled dissociation velocity.

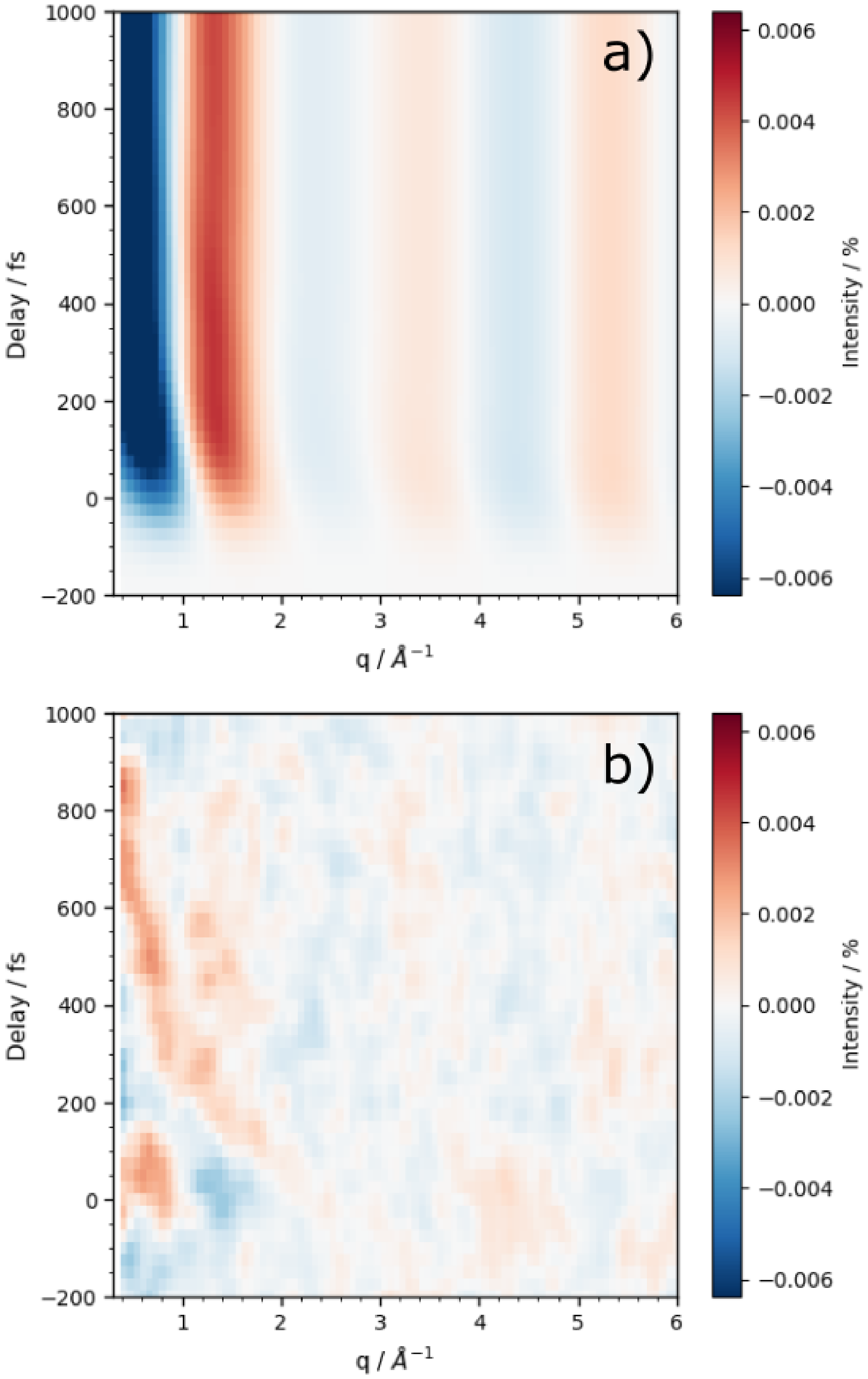

FIGURE 4.10: a) Time-resolved difference map of scattering intensity as a function of the momentum transfer q, and pump-probe delay (fs) calculated using the fitting procedure described in text. b) Residual error between the experimental and fitted data.

The obtained experimental data was then assumed to be the weighted sum of the two channels. The weights for each channel were determined using a least-squares fitting algorithm to minimise the difference between the calculated and experimental spectra, with the weight of each channel serving as the fitting parameter. In addition, the calculated spectrum was convolved with a Gaussian representation of the cross-correlation between the X-ray and UV laser pulses affecting the temporal resolution of the experiment. The FWHM of this Gaussian distribution is also a fitting parameter, resulting in a value of 145 fs. The spectrum resulting from this fitting process is illustrated in panel a) of Figure 4.10, and the residual difference between the experimental and calculated data is shown in panel b) of the same figure. The calculated weights resulted in a branching ratio of 3:1, in favour of the rapid dissociation channel.

The model shows a satisfactory fit to the data, but a considerable residual signal remains. In an effort to reduce this, a number of modifications were made to the model, such as introducing a time offset between the two channels and incorporating an acceleration period within the model. However, the fitting algorithm was unsuccessful in both instances because it was unable to locate a minimum.

4.5 Discussion

Two dissociation pathways were observed following the excitation of 2IT with a 252 nm photon. This is consistent with the findings of previous studies and the results presented in the previous chapter. The wavelength utilised in this study is shorter than that employed in the experiment discussed in the previous section, which is expected to lead to differences in dissociation velocities and branching ratios. However, previous research on the photolysis of 2IT at various wavelengths showed that the energy distribution of the atomic iodine product remained relatively unchanged with decreasing excitation wavelength, indicating a greater energy partition into the co-fragment [22]. The dissociation velocities obtained in this chapter were 6.42 Å/ps and 16.95 Å/ ps. In the previous chapter, the total kinetic energy release peaked at 9000 cm^{-1} and 1000 cm^{-1} for the prompt and delayed channels,respectively, corresponding to dissociation velocities of 6.9 and 20.7 Å/ ps^{-1}.

The values of the slow channel were unchanged within the experimental error between the two excitation wavelengths studied; however, a significant difference was observed for the fast channel. A previous study resolved the I and I* products [22]. This showed that the TKER distribution of I* peaks at 6000 cm^{-1} which corresponds to a dissociation velocity of 16.5 Å/ ps^{-1}. This value is much closer to the observed value of 16.95 Å/ ps^{-1}. The initially populated states have previously been correlated with I* products, with efficient nonadiabatic coupling to other $(n/\pi)\sigma^*$ states, providing an efficient route for the production of ground state I products [22, 24]. The features observed in this data suggest that dissociation along the repulsive $(n/\pi)\sigma^*$ states, leading to I* products, becomes a more significant channel when excited at 252 nm as opposed to 262 nm.

The consistency in the dissociation velocity of the slow channel following photolysis of 2IT at shorter excitation wavelengths is consistent with the proposed initial excitation into the $\pi\pi^*$ state, which then couples with $(n/\pi)\sigma^*$ continua. As postulated in the previous section, the relative importance of this channel increases at this excitation wavelength, leading to a ratio of 3:1 compared with 23:1 when 2IT was excited at a 262 nm. The low-energy pathway remains a minor channel, even with the absorption cross-section into $\pi\pi^*$ state state being much larger than that into the $(n/\pi)\sigma^*$ state. This suggests that a large portion of the excited population remains trapped within the $\pi\pi^*$ state. Comparisons with analogous thiophene and thiophenone photochemistry suggest possible rival ring-opening channels through nonadiabatic coupling to the ground state and the subsequent dissociation of ”hot” cyclic or acyclic ground state molecules [25–30]. While currently no such dynamics are identified within the data, this might be a contributing factor to the significant residual between the calculated and residual spectra. This analysis would benefit from further potential energy surface and trajectory calculations, which may describe this pathway and provide a better model of the experimental data.

4.6 Conclusion

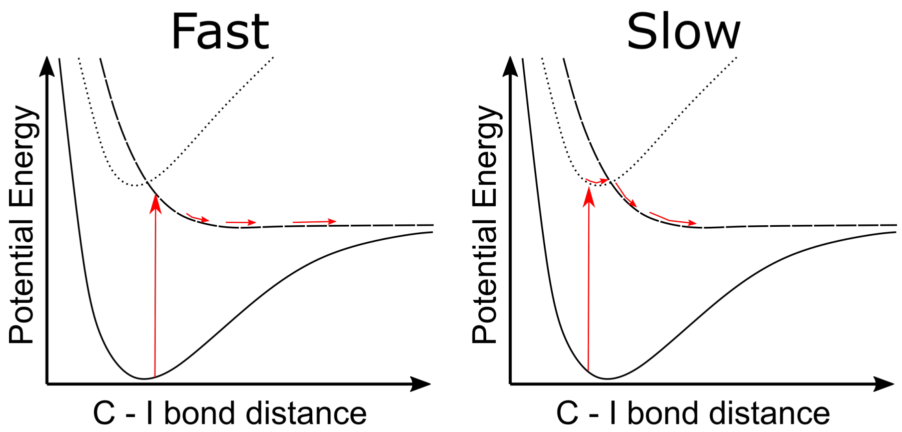

FIGURE 4.11: A schematic representation of the main PESs involved in photodissociation dynamics observed in 2IT following excitation at 252 nm including: the ground state (solid line), the $(n/\pi)\sigma^*$ state (dashed line) and the $\pi\pi^*$ state (dotted line). Constructed with the aid of calculations from [22]. Proposed pathways as described in text marked by red arrows.

The fragmentation dynamics of 2IT following excitation at 252 nm were investigated through time-resolved measurement of the X-ray scattering patterns. Two C-I bond fission channels were identified matching the results of the previous chapter. The schematic interpretation of the most relevant PESs is shown again in Figure 4.11. A simplistic model gives a branching ratio of 3:1 in favour of direct dissociation producing fast I fragments a significant increase when compared to the 262 nm dissociation results. The observed dissociation velocity is lower for this channel compared with results obtained following photolysis initiated by a 262 nm photon suggesting higher yield of spin-orbit excited I* products. A significant residual remains between the fitted and experimental data, further investigation will benefit from trajectory calculations.

Chapter 5

Time-resolved Valence Photoelectron Study of Iodothiophene Dissociation Dynamics

5.1 Introduction

Time-resolved photoelectron spectroscopy (TRPES) is a highly effective method for investigating the excited state populations that arise following photoexcitation [31, 32, 121]. This technique offers valuable insights into the dynamics of excited states and energy relaxation pathways within the studied system. By using a probe pulse to ionise the system and release electrons, TRPES allows the kinetic energy (KE) of the emitted photoelectrons to be correlated with the electronic state from which the electrons are ionised. This technique is particularly useful for capturing transient states and understanding the fast relaxation processes.

In contrast to the methodologies employed in the previous chapters, the experiment discussed here utilised a high-harmonic generation (HHG) source to generate probe pulses. The choice of probe source is a critical aspect of experimental design, and several key factors influence its selection to ensure the collection of accurate and meaningful data. In a TRPES experiment a critical consideration is that the probe photons must possess sufficient energy to ionise all relevant states within the system under investigation. Without this capability, the experiment would fail to capture the complete dynamics of the system, leading to gaps in the data and potentially incorrect interpretation.

Free-electron lasers (FELs), such as those utilised to generate probe pulses in previous experiments, are excellent sources for producing photons with the necessary energy on ultrafast timescales. However, the use of FELs has significant drawbacks, primarily owing to the extensive and complex infrastructure they demand. Setting up and maintaining a FEL requires considerable resources, including advanced facilities, specialised equipment, and highly trained personnel. These requirements limit the accessibility and use of FELs. By contrast, HHG sources offer an efficient alternative, particularly in settings where the complexity and cost of FELs are prohibitive. HHG sources can deliver the required high-energy photons (which in the context of TRPES are photons with sufficient energy to ionise all states of interest) with sufficient temporal resolution to effectively probe ultrafast dynamics. Importantly, the infrastructure required to operate an HHG source is significantly more manageable than that of an FEL. HHG systems can be integrated into standard laser laboratory environments, making them more accessible to a broader range of researchers and allowing for greater flexibility in the experimental design. Furthermore, the use of an HHG source does not compromise the accuracy of the data. These sources can still generate photons with energies sufficiently high to ionise a wide array of electronic states, thereby providing comprehensive insights into the behaviour of the system following photoexcitation.

However, it is important to recognise the challenges associated with utilising HHG sources. One significant issue is the relatively lower signal levels derived from lower photon flux compared with FELs. Despite the inherent advantages in terms of accessibility and infrastructure, HHG sources often produce lower photon fluxes than FELs, resulting in weaker signals that can affect the sensitivity and accuracy of the measurements. Addressing this challenge necessitates careful optimisation of the experimental conditions and often requires the use of highly sensitive detection equipment to ensure that the data collected are both reliable and meaningful. An example of successfully implemented HHG-based TRPES measurement is an experiment I was a part of during my PhD time which does not form a part of this thesis. There the key geometric and electronic structure changes associated with roaming dynamics were observed following photoexcitation of $\mathsf{CH_3CHO}$. The global HHG probe was used to observe the formation of the roaming intermediate on a < 100 fs time scale. This highlights the capabilities of HHG sources as probes for valance shell TRPES experiments [122].

In the experiment here 2IT molecules were excited and the resulting fragments were ionised using an ~ 22 eV laser pulse. The time-of-flight of the resulting photoelectrons was measured. The TRPES measurements were carried out separately using 245 nm and 262 nm pump pulses to excite the 2IT molecules. As previously discussed, the proposed mechanism involves initial excitation into a superposition of $(n/\pi)\sigma^*$ and $\pi\pi^*$ states with the relative contribution of each state being wavelength dependent.

Dissociation directly from $(n/\pi)\sigma^*$ states yields iodine atoms with high KE, and $\pi\pi^*$ states dissociate on a longer timescale and produce less energetic iodine atom fragments. The chosen excitation wavelengths of 245 nm and 262 nm were close to the peak absorption of the $\pi\pi^*$ and $(n/\pi)\sigma^*$ orbitals, respectively. This choice was made to investigate the differences between intermediates accessed by 2IT following excitation into each state. By pumping at 245 nm and 262 nm we will be able to investigate the dynamics of the system where the dominant excitation step is either into the $\pi\pi^*$ or $(n/\pi)\sigma^*$ manifold of states separately. From previous measurement we expect the excited state lifetime of the $(n/\pi)\sigma^*$ states to be very short, the characteristics of the $\pi\pi^*$ state are less known and are expected to be longer lived involving structural rearrangements localised on the ring initially.

5.1.1 Principles of time-of-flight spectrometry

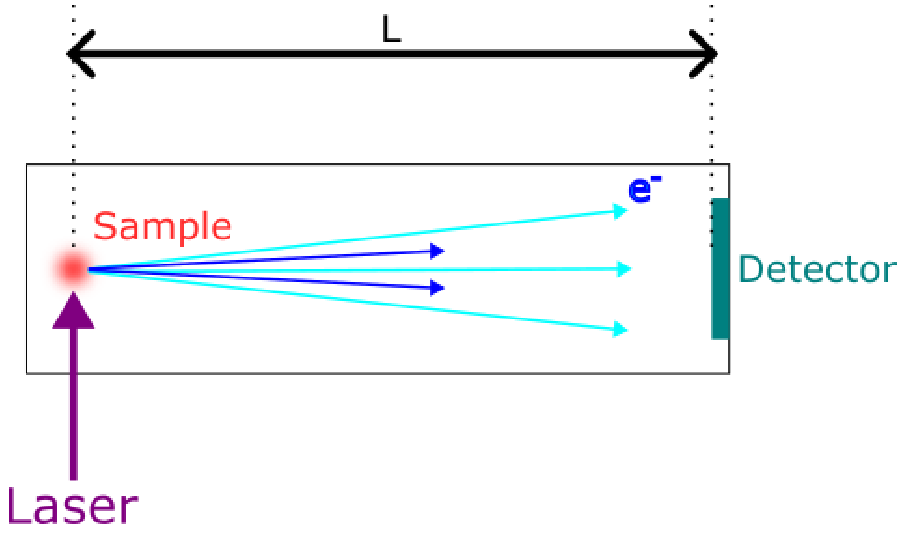

FIGURE 5.1: A simple schematic representation of a time-of-flight spectrometer. Higher energy electrons are shown in light blue and slower ones in dark blue.

The fundamental principles of electron time-of-flight (eTOF) spectroscopy are generally comparable to those of mass spectrometry, which is briefly discussed in Chapter 4. Unlike mass spectroscopy, which determines the mass-to-charge ratios of ions, eTOF spectroscopy focuses on the electron energy. An eTOF spectrometer is comprised of a vacuum-sealed tube, with photoelectrons generated at one end and detected at the other. This is illustrated schematically in Figure 5.1. The relationship between the KE of the electron and its flight time in the drift tube of length L is represented mathematically by the following equation:

$$E_{KE} = \frac{1}{2} m_e v^2 = \frac{1}{2} m_e \left(\frac{L}{t}\right)^2 \tag{5.1}$$

where m_e is the mass of the electron.

In the field-free configuration, only the electrons emitted towards the detector are detected. This may be problematic when attempting to probe states with low populations. One of the measures taken to address this drawback was setting the polarisation of the pump and probe laser pulses to be in the plane of the TOF axis, which maximises the number of electrons ejected towards the detector.

The KE of the emitted photoelectrons is related to their binding energy (BE) which means that by measuring the flight times, we can directly probe the electronic states of the target molecule. The KE of the emitted photoelectrons is related to the BE according to:

$$\text{Kinetic energy} = \text{Probe energy} - \text{Binding energy} \tag{5.2}$$

5.2 Experimental Details

The experiment was performed at the Artemis laser facility at the Rutherford Appleton Laboratory in Didcot, UK [123].

For the pump and probe pulses, the output of a 1 kHz Ti:Sapphire chirped pulse amplification (CPA) laser system operating at 800 nm with approximately 30 fs pulses at 14 mJ was used. This output was split to produce synchronised pulses. For the probe pulse, a 400 nm beam was obtained by frequency doubling the 800 nm output of the CPA system. This was then focused into a jet of argon gas for HHG. A single harmonic, with an energy of $\sim$ 22 eV, was selected using the time-preserving monochromator, and this was then focused into the interaction region with a torodial mirror [123].

For the pump pulse, the 800 nm pulse was directed to a HE-TOPAZ optical parametric amplifier (OPA) to produce wavelengths of 245 nm and 262 nm. The pump beam was focused with an f = 50 cm mirror outside of the vacuum chamber and a D-shaped mirror inside the chamber was used to reflect it towards the interaction region so that the angle between the pump and probe beams was small (around 3 degrees).

The photoelectrons entered a approximately 60 cm long drift tube, after which there is a 111 mm long region where the electrons are accelerated by 1 keV to reduce any effects of the Earth's magnetic field penetrating through the detector end of the spectrometer. This acceleration is high enough that the time spent by the electrons in this region is negligible compared to their flight time in the drift tube. The spectrometer has a resolution of $\frac{T}{\Delta T} \sim 100$, which corresponds to an energy resolution on the order of 0.1 eV for electrons with kinetic energies on the order of 10 eV.

The electrons are detected by a 40 mm diameter chevron stack MCP. The signal from the MCP is amplified and then sent to a constant fraction discriminator (CFD). This takes the input signal and attenuates it by a constant fraction f. It then takes a copy of the original input signal, inverts it, and delays it by some amount of time grater than the rise time. The attenuated and inverted/delayed signals are added to produce a signal that crosses zero at a time independent of the amplitude of the input pulse. Then the output of the CFD is sent to a time-to-digital converter (TDC). This starts measuring when it is triggered by the laser pulse, using a fast photodiode, and then the arrival time of the signal from the CFD causes it to stop measuring and output the time between these two events. A list of times of electrons hitting the MCP is therefore produced.

A translation stage in the pump beam path was used to change the pump-probe time delay. To find time zero - where the pump and probe beams both arrive at the interaction region at the same time - the pulses were approximately overlapped in time by moving the stage and using an oscilloscope to monitor the overlap. Then time zero was found with greater accuracy by looking for an increase in intensity in the electron counts. Once time zero was found, the translation stage was moved through positions corresponding to a range of pump probe delays from -2 ps to 1.5 ps in non-linear steps.

The 2IT sample was contained in a liquid sample holder, and He was used as a carrier gas to introduce it to the interaction region through a nozzle.

5.3 Data Treatment

The data collected in this experiment consist of a list of electron arrival times and the corresponding electron counts for a range of pump–probe delays, which are converted into BE using the following equations:

$$\begin{aligned} BE &= E_{photon} - KE \\ &= E_{photon} - \frac{1}{2} m_e v^2 \\ &= E_{photon} - \frac{1}{2} m_e \left(\frac{L}{t_{tdc} - t_{offset}} \right) \end{aligned} \tag{5.3}$$

where E_{photon} is the photon energy of the probe pulse (eV), m_e is the mass of the electron, L is the distance the electrons travel in meters, t_{tdc} is the time from the TDC, and t_{offset} is the TDC time at which the laser pulses are incident on the sample.

A TDC, possesses an arbitrary but consistent zero offset. A small number of photons from the laser pulses reach the detector, and as they travel significantly faster than the electrons, their arrival time is used to define t_{offset}.

In Equation 5.3, the values of E_{photon}, and L are constant and are known approximately. E_{photon} is a harmonic of 400 nm light, but various factors, such as phase-matching effects and variation of transmission of the beamline with wavelength, mean that the exact harmonic photon energy must be determined from the data. The value of L is also known approximately because the length of the spectrometer is known, but the exact distance the electrons travel depends on the precise position of the crossing point of the laser beams in the sample. Therefore, this must also be determined using data.

In order to deduce the values of these constants, a first-order polynomial was fitted to specific features in the spectrum with known energies. The gradient of this polynomial therefore represents the value of $(\frac{1}{2} m_e L)$ and E_{photon} is given by the y-intercept. The peaks used in the calibration were the ground-state peaks of iodothiophene with binding energy of 8.63, 9.56, 10.0 and 10.73 eV [34]. The number of counts must also be scaled by a Jacobian as a part of the conversion from the TDC electron arrival time to energy. Because the raw data counts correspond to counts per nanosecond, and the calibrated spectrum refers to counts per electron. The value of $|J|$ by which the counts should be divided is given by the following:

$$\begin{aligned} J &= \frac{\delta}{\delta t}(KE) \\ &= \frac{1}{2}m_e L^2 \left(\frac{\delta}{\delta t}t^{-2}\right) \\ &= \frac{1}{2}m_e d^2(-2t^{-3}) \\ &= -2t^{-1}\left(\frac{1}{2}m_e\frac{d^2}{t^2}\right) \\ |J| &= \frac{2KE}{t} \end{aligned} \tag{5.4}$$

5.4 Results

5.4.1 245 nm data

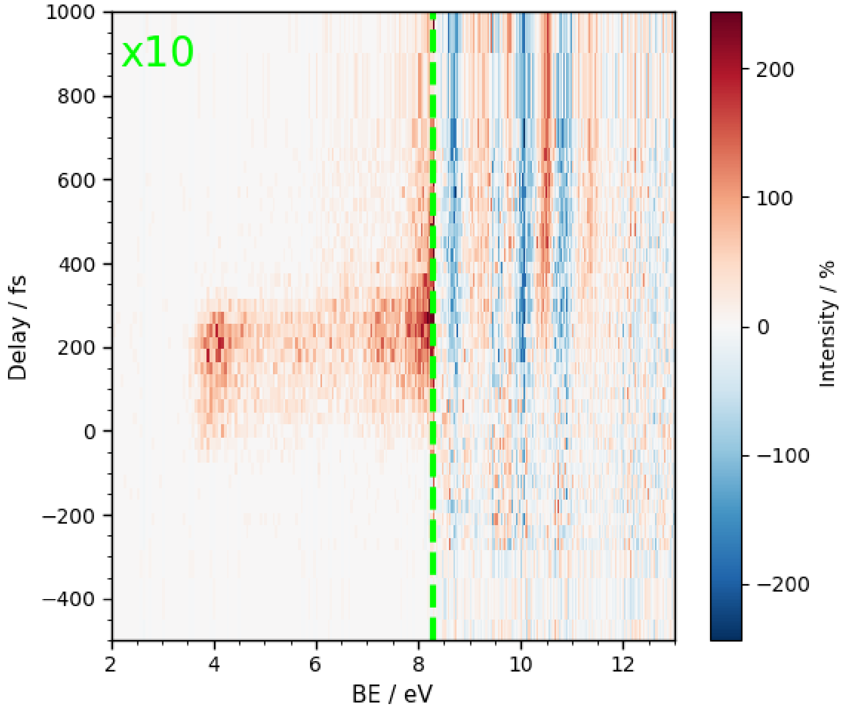

FIGURE 5.2: Difference spectrum following photolysis of 2IT using a 245 nm laser pulse. The ground state deletions are shown in blue and increased populations of other states in red. The intensity on the left hand side of the green dashed line is multiplied by 10 to make the lower intensity features clearer,

The intensity levels associated with ionisation from the excited states were relatively minor compared to those corresponding to ionisation from the ground states (by approximately 3 orders of magnitude). To make these changes more apparent, a background subtraction was performed. The average of the spectra from -0.5 ps to -1 ps was used as the spectrum of the ground state 2IT, which served as the background for the changes in intensity following time zero. This average was subtracted from the spectra at all time delays, resulting in a series of difference spectra that showed enhancements (in red) and depletions (in blue) relative to the 2IT ground state spectrum. The difference spectrum following photoexcitation of 2IT with 245 nm photons is shown in Figure 5.2.

A clear depletion of the ground state 2IT peaks after time zero is seen in the 245 nm dataset centred at 8.63, 9.56, 10.0 and 10.73 eV. Rises in intensity are observed at other binding energies, indicating population of new states. In the 3.8-8 eV region, a transient increase in intensity is visible around time zero. These peaks can be clearly identified due to the absence of ground-state features in this energy range. To show the population changes of these states more clearly, the total difference signal over time was found in several distinct energy regions and plotted in Figure 5.3.

The peak associated with the initially excited state appears at 3.8-4.2 eV, the temporal trace of intensity in this energy region following excitation with 245 nm photons, as shown in Figure 5.3a), shows a double-peaked feature resembling a superposition of two Gaussian profiles. Upon examining the colour map, it can be seen that the initially excited state peaks at a slightly lower binding energy around 3.9 eV and rapidly shifts to a peak at approximately 4.1 eV. The two features are difficult to isolate for the purposes of the lineouts shown in Figure 5.3. Therefore, in the absence of trajectory calculations to support the analysis of this data, only the two intensity peaks are considered to provide a qualitative timeline for this shift. The peak values show the motion occurs within $\sim$ 150 fs.

The shift from the FC region at 3.8-4.2 eV to the highest binding energy that can be measured before overlap with the ground state occurs begins after the second peak, and takes $\sim$ 200 fs. This final state, shown in Figure 5.3b), has a roughly Gaussian profile at early pump-probe delays. Following the initially Gaussian decay, some intensity remains in this energy region at all investigated pump-probe time delays.

An increase in intensity associated with the I atom fragments produced by the photolysis is observed at 10.38-10.53 eV (Figure 5.3c)) and 11.2-11.45 eV (Figure 5.3d)) for the two spin-orbit excited states of the iodine atom. To gain some qualitative insight into the dynamics, a simple error function was fit to the product traces, shown in red. This results in a time offset of 250 fs in both cases which coincides with the the peak of the highest binding energy excited state, this is highlighted in Figure 5.3 by a dashed black line spanning all panels.

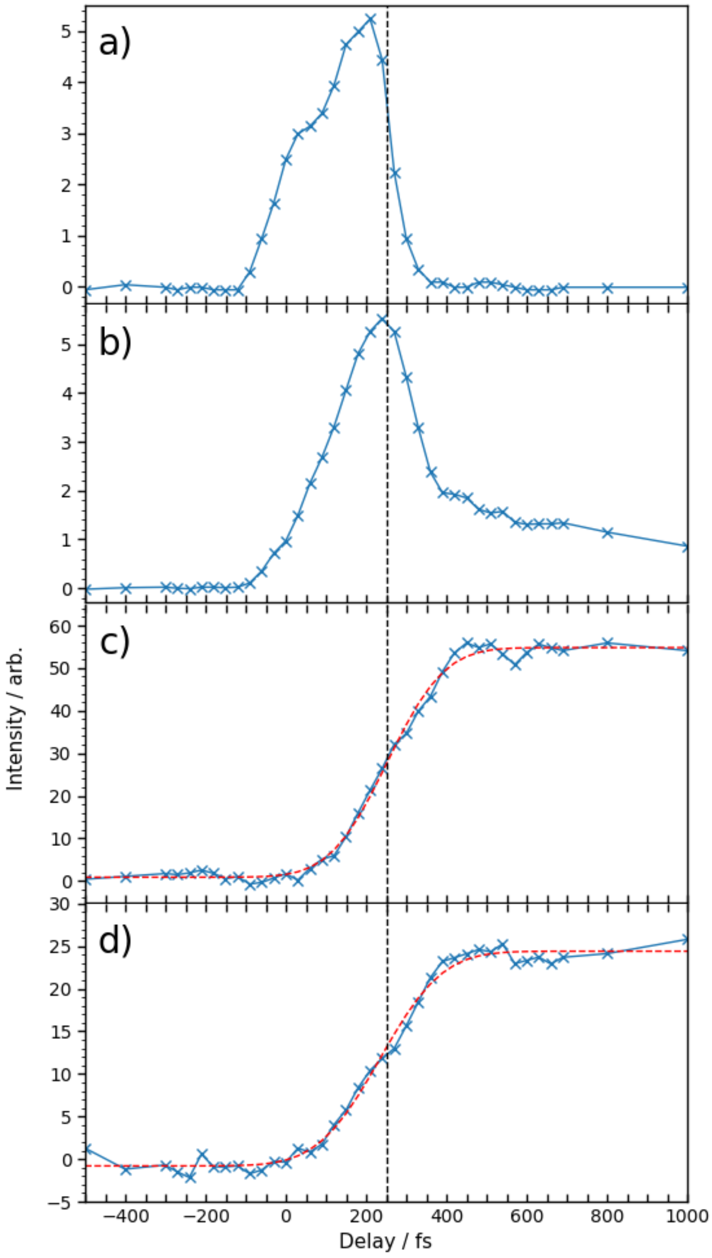

FIGURE 5.3: Total difference photoelectron intensities following photolysis of 2IT with a 245 nm laser pulse in the energy regions: a)3.8-4.2 eV, b) 7.25-8.0 eV, c) 10.38-10.53 eV and d) 11.2-11.45 eV. The measured intensities are shown in blue with "x" marking the data points and fits in panels c) and d) are shown as red dashed lines. A vertical dashed line marks the centre of rise calculated in the fit.

5.4.2 262 nm data

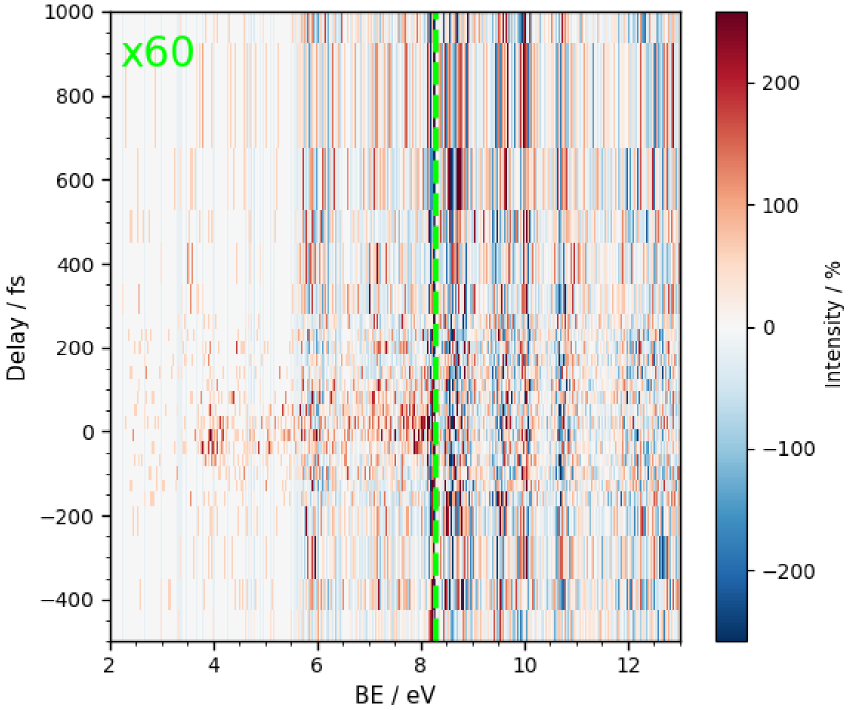

FIGURE 5.4: Difference spectrum following photolysis of 2IT using a 262 nm laser pulse. The ground state deletions are shown in blue and increased populations of other states in red. The intensity on the left hand side of the green dashed line is multiplied by 60 to make the lower intensity features clearer,

Figure 5.4 shows the difference spectra following photoexcitation at 262 nm. The difference in the signal level of the data obtained at the two pump wavelengths is apparent. The data acquired following the excitation of 2IT by 262 nm photons appears considerably weaker and noisier. This is clearly evident when examining the ground-state peaks of 2IT in each spectrum. While a clear depletion of the ground state 2IT peaks after time zero is seen in the 245 nm dataset equivalent features in the 262 nm dataset are nowhere near as clear. This is predominately due to the much lower absorption cross-section of the $(n/\pi)\sigma^*$ orbital. By referring to the absorption spectrum shown in Figure 3.13 in Chapter 3, the absorption in the $\pi\pi^*$ states is estimated to be approximately an order of magnitude larger than that in the $(n/\pi)\sigma^*$ states at the two wavelengths used.

At a pump wavelength of 262 nm the signal shows a rapid shift to higher binding energy as the C-I bond breaks. The shift from the FC region at 3.8-4.2 eV, plotted as a lineout in Figure 5.5a, to the highest binding energy we can measure, shown in Figure 5.5, before overlap with the ground state signal occurs within $\sim$ 50 fs, this is much faster than in the case of 245 nm dataset. The appearance of the spectrum is very similar to that of previously reported methyl iodide suggesting a similar rapid dissociation of the C-I bond following excitation into a dissociative $(n/\pi)\sigma^*$ state as

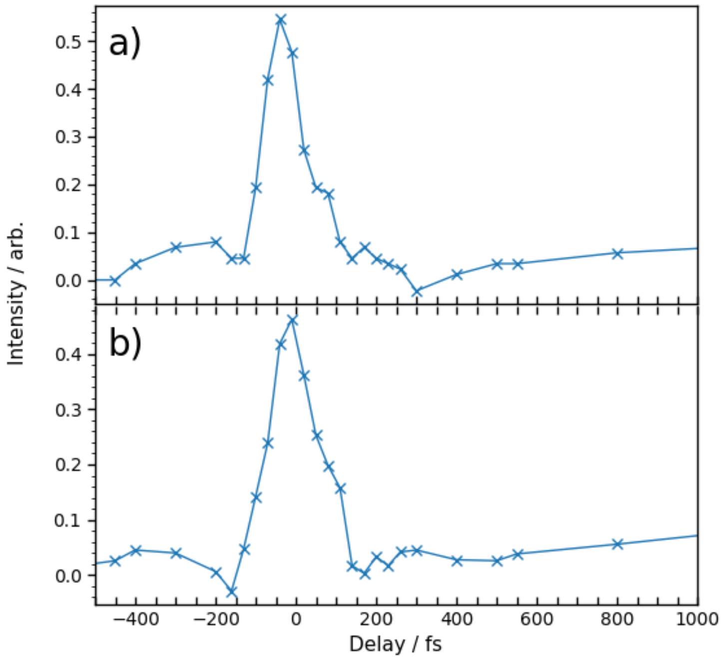

FIGURE 5.5: Total difference photoelectron intensities following photolysis of 2IT with a 262 nm laser pulse in the energy regions: a)3.8-4.2 eV, b) 7.25-8.0 eV.

discussed in previous chapters [31, 32]. Due to the low excitation cross-section the appearance of the fragments could not be captured.

5.5 Discussion

The findings from the TRPES method used to probe 2IT following excitation using 245 nm and 262 nm photons broadly align with the conclusions and the proposed mechanism outlined in earlier sections. Although the data in this chapter do not allow for a direct examination of the KE distribution of iodine fragments and cannot be compared directly to the results from earlier sections, it does offer insight into the energy states accessed. This provided new information about the mechanism.

As previously mentioned, the absorption of a 262 nm photon mainly results in excitation into the $(n/\pi)\sigma^*$ state, which quickly couples to the $(n/\pi)\sigma^*$ continuum, leading to a narrow-intensity peak at $\sim$ 4 eV. However, when 2IT molecules are excited using a 245 nm photon, a different structure emerges. In this case, the initial excitation is primarily proposed to occur in the $\pi\pi^*$ state, which is predominantly located on the thiophene ring and couples into the $(n/\pi)sigma^*$ continuum through rapid contortion of the ring structure. This change in ring geometry results in the overlapping appearance of the features in Figure 5.3b). By calculating the difference between the two peaks, it is suggested that this initial ring motion occurs within 250 fs.

In both instances, the excited states initially couple with the $(n/\pi)\sigma^*$ continuum through the C-I bond extension, which manifests as a broad, short-lived feature spanning 4.2 to 7 eV. Within 10s of fs, the repulsive $(n/\pi)\sigma^*$ states from which the molecule can dissociate are populated, resulting in rapid C-I bond breakage. Major differences in the intensity profiles at the two excitation wavelengths in this energy region can be observed at long pump-probe time delays. While excitation with 262 nm photons results in the intensity rapidly dropping back to the baseline, the use of a 245 nm pump laser appears to leave some population trapped at this energy at all measured time delays. It is unlikely that this population is trapped within repulsive $(n/\pi)\sigma^*$ states; however, this feature appears at the energy predicted for the thiophenyl radical in Chapter 3 (8.0 eV). While trajectory calculations would aid in the full assignment, this feature is currently assigned to the thiophenyl product formation.

Previous studies have suggested that coupling to the ground state is possible through either C-I or C-S bond extension [22–24]. However, whether the ring remains closed or opens remains unknown, as this finding does not eliminate either option.

In the context of the 245 nm dataset, it was possible to identify the formation of I atom products on top of the ground state depletion peaks. The low signal levels at 262 nm prevented such identification. The intensity associated with the iodine atom products yielded by photolysis of 2IT with 245 nm photons increases alongside the depletion of highest binding energy excited state. Notably, no delayed increase in iodine atom products was identified. There are two potential explanations for this observation: Firstly, the secondary increase in iodine atom yield remains a minor channel at all excitation wavelengths as was seen in this thesis and previous studies, thus being undetectable atop the dominant prompt dissociation signal. Alternatively, both channels can produce iodine products on similar timescales, rendering them indistinguishable in the TRPES experiment. In this case, the thiophenyl radical is produced in either the $\tilde{X}$ or $\tilde{A}$ state, leading to the previously observed difference in the kinetic energy of the iodine atom products. The pathway producing thiophenyl radicals in the $\tilde{A}$ state becomes more significant at shorter excitation wavelengths. This was suggested as a possibility and was supported by calculations in previous studies [22].

5.6 Conclusion

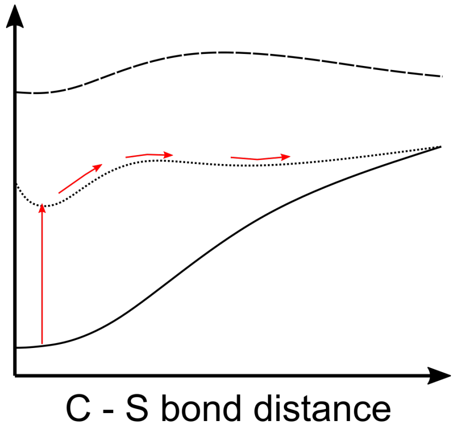

FIGURE 5.6: A schematic representation of the main PESs involved in photodissociation dynamics observed in 2IT following population of the $\pi\pi^*$ state (dotted) including: the ground state (solid line), the $(n/\pi)\sigma^*$ state (dashed line). Constructed with the aid of calculations from [22]. Proposed pathway to a ring-opened structure as described in text marked by red arrows.

The photolysis of 2IT molecules following excitation at 245 nm and 262 nm were investigated through time-resolved measurement of photoelectron energies. The analysis was complicated by low ionisation cross-section of the $(n/\pi)\sigma^*$ state as well as presence of overlapping features in the 245 nm dataset. Therefore, this data, as well as all data presented in previous chapters, would benefit greatly from comparison to trajectory calculations. Nevertheless useful insights are gained through this experiment. The observed changes are consistent with initial excitation into $(n/\pi)\sigma^*$ at 262 nm and $\pi\pi^*$ states at 245 nm. When populating the $\pi\pi^*$ state the observed features are consistent with coupling into the $(n/\pi)\sigma^*$ continuum through ring contortion. This provides further evidence towards the previous assignment of pathways, described in the previous chapters. Furthermore, the experiment described in this chapter was able to for the first time see clear indication of a ring-opened structure, formed by an alternative route along the $\pi\pi^*$ state as depicted in Figure 5.6.

The observed features are consistent with the rapid dissociation from the $(n/\pi)\sigma^*$ state continuum suggested as one of the dissociation pathways in the previous chapters however no evidence of a secondary dissociation pathway is seen within the data collected using TRPES.

Chapter 6

Summary

This thesis explored the use of FEL and HHG sources to investigate the molecular dynamics of iodothiophenes, with particular focus on their dissociation pathways and the interplay of complementary experimental techniques.

Previous studies on iodothiophenes provided two main insights. Firstly absorption of a photon in the range of 220-305 nm results in population of either the $(n/\sigma)\sigma^*$ or the $\pi\pi^*$ states. Based on cross-sections, both from previous literature [22, 24] as well as those presented in Chapter 3 of this thesis, the peak absorption into each state happens at approximately 245 nm and 275 nm respectively.

The kinetic energies of iodine fragments resulting from neutral photodissociation of 2-iodothiophene were previously investigated at their asymptotic yield [22]. In Chapter 3 of this thesis the same fragments were investigated through site-selective ionisation following photoexcitation by a 262 nm pump in a time-resolved regime. The wavelength was chosen to predominately populate the $(n/\pi)\sigma^*$ manifold of states while being easily accessible in the facility setting where the experiment was performed. The results showed iodine atom fragments produced via two pathways, consistent with previous time-averaged measurements [22]. The dominant channel is assigned as a direct dissociation from the $(n/\pi)\sigma^*$ with a lifetime consistent with the transient absorption study [24]. This was the only experiment performed as a part of this thesis which was able to capture information about the iodine atom fragments separately for each channel. This is especially important due to the relatively low contribution of the minor pathway which makes it hard to characterise in all other experiments on top of the dominant channel signal. Through site-selective ionisation, it was possible to see a delay in the appearance time of iodine fragments released with the lower kinetic energy. This is consistent with initial population into a $\pi\pi^*$ state which itself is not dissociative with respect to the C-I coordinate. Time is taken to access a conical intersection with the dissociative $(n/\pi)\sigma^*$ states leading to the observed delay. These findings support the assignment of the two channels to initial population of superposition of states.

In Chapter 4 the process was investigated at a shorter excitation wavelength of 252 nm where excitation into the $\pi\pi^*$ manifold of states becomes more significant. The photolysis was then monitored using X-ray scattering. As the two pathways result in the fission of the same bond, their contributions become much harder to distinguish in this experiment. Nonetheless, by utilising a Hough transform approach, the C-I bond was again observed to dissociate via two pathways. The calculated dissociation velocities matched well with those observed in Chapter 4 with any differences easily attributed to the slight difference in pump wavelength. An increase in the contribution from the "slower" channel was observed providing further evidence that it starts from initial excitation into the $\pi\pi*$ state. At the lower pump wavelength the proportion of initial excitation into the $\pi\pi*$ state increases.

A simplistic dissociation model was created where the C-I bond was extended at the calculated dissociation velocities whilst keeping the structure of the co-fragment unchanged. This provided an overall decent fit, however a significant residual difference remained between the model and experimental spectra. This highlights the unique capability of the X-ray scattering experiment to directly measure changes in all of the bond distances in the molecule which the simple model does not account for. While this is outside the scope of this thesis this residual is likely related to the geometry changes within the thiophenyl radical co-fragment including the suspected ring-opening. In order to be able to extract more useful information the study would benefit from trajectory calculations.

Finally in chapter 5, a HHG source was used to supplement the data acquired by using FELs. The 2IT isomer was excited using 245 nm and 262 nm in order to investigate the differences between initial population of the $\pi\pi^*$ and $(n/\pi)\sigma^*$ manifolds of states respectively. Excitation into the $(n/\pi)\sigma^*$ states using the 262 nm pump wavelength lead to a rapid dissociation, with little evidence of other geometry changes. On the other hand following excitation using 245 nm and therefore initial population of $\pi\pi^*$ shows significantly different features. The peak associated with the initially excited state shows a double peak providing direct evidence of a change in geometry required to reach a conical intersection. The product formation then coincides with the depletion of the second peak further supporting the pathway description. This experiment is also the only one to show a long-lived feature which could be an indication of a previously unseen ring-opened structure. Unlike the FEL studies, no evidence of two dissociation pathways was observed in this case (for a single excitation wavelength), underscoring the unique capabilities and limitations of each technique. As with the FEL experiments, trajectory calculations would greatly aid in assigning the observed features and deepening the interpretation of the dynamics.

The three experiments highlight the importance of probing dynamics via several methods in order to obtain a comprehensive understanding of the processes at play. Each experiment provided unique insight into the photodissociation dynamics. The inner-shell ionisation measurement was able to clearly distinguish the temporal characteristics of iodine fragments produced with two distinct kinetic energies, which are too overlapped to separate in other experiments. Through valance-shell ionisation we are able to infer structural changes associated with the key points on the PES in the proposed mechanism. Finally, with input from quantum calculations, the X-ray scattering experiment has the potential to directly observe the previously inferred structure changes.

Beyond the specific findings on iodothiophene dynamics, this work highlights the importance of benchmarking data for advancing theoretical models. The experimental observables obtained in these studies offer valuable constraints for trajectory simulations and theoretical treatments of molecular dynamics, especially in the context of cutting-edge spectroscopies. By providing high-quality data that captures complex processes, such as ring contortion and isomer-specific branching ratios, this work paves the way for improved theoretical frameworks capable of predicting experimental outcomes.

In conclusion, this thesis demonstrates how the synergistic application of state-of-the-art experimental techniques and theoretical advancements can provide a holistic view of complex molecular dynamics. While the dissociation pathways of iodothiophene are not yet fully understood, the insights gained from this work lay a strong foundation for future explorations and contribute to the broader field of ultrafast photochemistry.

Bibliography

(1) R. Emerson and W. Arnold, *The Journal of general physiology*, 1932, **16**, 191–205.

(2) T. F. Schulze and T. W. Schmidt, *Energy & Environmental Science*, 2015, **8**, 103–125.

(3) A. H. Zewail, *The Journal of Physical Chemistry A*, 2000, **104**, 5660–5694.

(4) N. Scherer, J. Knee, D. Smith and A. Zewail, *The Journal of Physical Chemistry*, 1985, **89**, 5141–5143.

(5) M. Dantus, M. J. Rosker and A. H. Zewail, *The Journal of chemical physics*, 1988, **89**, 6128–6140.

(6) R. Berera, R. van Grondelle and J. T. Kennis, *Photosynthesis research*, 2009, **101**, 105–118.

(7) D. P. Millar, *Current opinion in structural biology*, 1996, **6**, 637–642.

(8) S. K. Sahoo, S. Umapathy and A. W. Parker, *Applied Spectroscopy*, 2011, **65**, 1087–1115.

(9) C. Pellegrini, *The European Physical Journal H*, 2012, **37**, 659–708.

(10) P. Baum, *Chemical Physics*, 2013, **423**, 55–61.

(11) A. Messiah, *Quantum mechanics*, Courier Corporation, 2014.

(12) M. Born and W. Heisenberg, *Original Scientific Papers Wissenschaftliche Originalarbeiten*, 1985, 216–246.

(13) G. A. Worth and L. S. Cederbaum, *Annu. Rev. Phys. Chem.*, 2004, **55**, 127–158.

(14) W. Greiner, *Quantum mechanics: an introduction*, Springer Science & Business Media, 2011.

(15) L. González, D. Escudero and L. Serrano-Andrés, *ChemPhysChem*, 2012, **13**, 28–51.

(16) G. Barbarella, M. Melucci and G. Sotgiu, *Advanced Materials*, 2005, **17**, 1581–1593.

(17) R. Shah and P. K. Verma, *Chemistry Central Journal*, 2018, **12**, 1–22.

(18) M. Kobayashi, J. Chen, T.-C. Chung, F. Moraes, A. Heeger and F. Wudl, *Synthetic metals*, 1984, **9**, 77–86.

(19) Y. Xu, L. Sun, J. Wu, W. Ye, Y. Chen, S. Zhang, C. Miao and H. Huang, *Dyes and Pigments*, 2019, **168**, 36–41.

(20) J. Podlesný and F. Bureš, *Organics*, 2022, **3**, 446–469.

(21) B. Amna, H. M. Siddiqi, A. Hassan and T. Ozturk, *RSC advances*, 2020, **10**, 4322–4396.

(22) B. Marchetti, T. N. V. Karsili, O. Kelly, P. Kapetanopoulos and M. N. R. Ashfold, *The Journal of Chemical Physics*, 2015, **142**, 224303.

(23) F. Zhang, Z. Cao, X. Qin, Y. Liu, Y. Wang and B. Zhang, *Acta Physico-Chimica Sinica*, 2008, **24**, 1335–1341.

(24) B. W. Toulson, D. Hait, D. Faccialà, D. M. Neumark, S. R. Leone, M. Head-Gordon and O. Gessner, *The Journal of Chemical Physics*, 2023, **159**, 034304.

(25) X.-F. Wu, X. Zheng, H.-G. Wang, Y.-Y. Zhao, X. Guan, D. L. Phillips, X. Chen and W. Fang, *The Journal of chemical physics*, 2010, **133**.

(26) G. Cui and W. Fang, *The Journal of Physical Chemistry A*, 2011, **115**, 11544–11550.

(27) T. Schnappinger, P. Kölle, M. Marazzi, A. Monari, L. González and R. de Vivie-Riedle, *Physical Chemistry Chemical Physics*, 2017, **19**, 25662–25670.

(28) A. Prlj, B. F. Curchod and C. Corminboeuf, *Physical Chemistry Chemical Physics*, 2015, **17**, 14719–14730.

(29) M. Pederzoli and J. Pittner, *The Journal of Chemical Physics*, 2017, **146**.

(30) S. Pathak, L. M. Ibele, R. Boll, C. Callegari, A. Demidovich, B. Erk, R. Feifel, R. Forbes, M. Di Fraia, L. Giannessi et al., *Nature chemistry*, 2020, **12**, 795–800.

(31) E. M. Warne, B. Downes-Ward, J. Woodhouse, M. A. Parkes, E. Springate, P. A. J. Pearcy, Y. Zhang, G. Karras, A. S. Wyatt, R. T. Chapman and R. S. Minns, *Phys. Chem. Chem. Phys.*, 2020, **22**, 25695–25703.

(32) A. D. Smith, E. M. Warne, D. Bellshaw, D. A. Horke, M. Tudorovskya, E. Springate, A. J. H. Jones, C. Cacho, R. T. Chapman, A. Kirrander and R. S. Minns, *Phys. Rev. Lett.*, 2018, **120**, 183003.

(33) H.-L. Zhu, J. Liu, X. Zheng and D. L. Phillips, *The Journal of chemical physics*, 2006, **125**.

(34) NIST, *NIST Chemistry WebBook*.

(35) M. J. Hogan, C. Pellegrini, J. Rosenzweig, S. Anderson, P. Frigola, A. Tremaine, C. Fortgang, D. C. Nguyen, R. L. Sheffield, J. Kinross-Wright, A. Varfolomeev, A. A. Varfolomeev, S. Tolmachev and R. Carr, *Physical Review Letters*, 1998, **81**, 4867–4870.

(36) P. Emma, R. Akre, J. Arthur, R. Bionta, C. Bostedt, J. Bozek, A. Brachmann, P. Bucksbaum, R. Coffee, F.-J. Decker et al., *nature photonics*, 2010, **4**, 641–647.

(37) P. Emma, R. Akre, J. Arthur, R. Bionta, C. Bostedt, J. Bozek, A. Brachmann, P. Bucksbaum, R. Coffee, F.-J. Decker et al., *nature photonics*, 2010, **4**, 641–647.

(38) J. M. Madey, *Journal of Applied Physics*, 1971, **42**, 1906–1913.

(39) A. Kondratenko and E. Saldin, *Part. Accel*, 1980, **10**, 103.

(40) *Handbook of Physics*, ed. W. Benenson, J .W. Harris, H. Stocker and H. Lutz, Springer New York, 1st edn., 2002.

(41) Z. Huang and K.-J. Kim, *Physical Review Special Topics-Accelerators and Beams*, 2007, **10**, 034801.

(42) S. V. Milton, E. Gluskin, N. D. Arnold, C. Benson, W. Berg, S. G. Biedron, M. Borland, Y. C. Chae, R. J. Dejus, P. K. Den Hartog, B. Deriy, M. Erdmann, Y. I. Eidelman, M. W. Hahne, Z. Huang, K. J. Kim, J. W. Lewellen, Y. Li, A. H. Lumpkin, O. Makarov, E. R. Moog, A. Nassiri, V. Sajaev, R. Soliday, B. J. Tieman, E. M. Trakhtenberg, G. Travish, I. B. Vasserman, N. A. Vinokurov, X. J. Wang, G. Wiemerslage and B. X. Yang, *Science*, 2001, **292**, 2037–2041.

(43) SLAC, *XPP Specifications*, 2021.

(44) *Free-electron laser FLASH*.

(45) J. Duris, S. Li, T. Driver, E. G. Champenois, J. P. MacArthur, A. A. Lutman, Z. Zhang, P. Rosenberger, J. W. Aldrich, R. Coffee et al., *Nature Photonics*, 2020, **14**, 30–36.

(46) E. L. Saldin, E. A. Schneidmiller and M. V. Yurkov, *Optics Communications*, 1998, **148**, 383–403.

(47) E. Allaria, R. Appio, L. Badano, W. Barletta, S. Bassanese, S. Biedron, A. Borga, E. Busetto, D. Castronovo, P. Cinquegrana et al., *Nature Photonics*, 2012, **6**, 699–704.

(48) G. Geloni, Z. Huang and C. Pellegrini, 2017.

(49) E. Allaria, R. Appio, L. Badano, W. A. Barletta, S. Bassanese, S. G. Biedron, A. Borga, E. Busetto, D. Castronovo, P. Cinquegrana, S. Cleva, D. Cocco, M. Cornacchia, P. Craievich, I. Cudin, G. D'Auria, M. Dal Forno, M. B. Danailov, R. De Monte, G. De Ninno, P. Delgiusto, A. Demidovich, S. Di Mitri, B. Diviacco, A. Fabris, R. Fabris, W. Fawley, M. Ferianis, E. Ferrari, S. Ferry, L. Froehlich, P. Furlan, G. Gaio, F. Gelmetti, L. Giannessi, M. Giannini, R. Gobessi, R. Ivanov, E. Karantzoulis, M. Lonza, A. Lutman, B. Mahieu, M. Milloch, S. V. Milton, M. Musardo, I. Nikolov, S. Noe, F. Parmigiani, G. Penco, M. Petronio, L. Pivetta, M. Predonzani, F. Rossi, L. Rumiz, A. Salom, C. Scafuri, C. Serpico, P. Sigalotti, S. Spampinati, C. Spezzani, M. Svandrlik, C. Svetina, S. Tazzari, M. Trovo, R. Umer, A. Vascotto, M. Veronese, R. Visintini, M. Zaccaria, D. Zangrando and M. Zangrando, *Nature Photonics 2012 6:10*, 2012, **6**, 699–704.

(50) J. Feldbaus, E. L. Saldin, J. R. Schneider, E. A. Schneidmiller and M. V. Yurkov, *Nuclear Instruments and Methods in Physics Research Section A: Accelerators, Spectrometers, Detectors and Associated Equipment*, 1997, **393**, 162–166.

(51) J. Amann, W. Berg, V. Blank, F. J. Decker, Y. Ding, P. Emma, Y. Feng, J. Frisch, D. Fritz, J. Hastings, Z. Huang, J. Krzywinski, R. Lindberg, H. Loos, A. Lutman, H. D. Nuhn, D. Ratner, J. Rzepiela, D. Shu, Y. Shvyd'Ko, S. Spampinati, S. Stoupin, S. Terentyev, E. Trakhtenberg, D. Walz, J. Welch, J. Wu, A. Zholents and D. Zhu, *Nature Photonics 2012 6:10*, 2012, **6**, 693–698.

(52) D. Ratner, R. Abela, J. Amann, C. Behrens, D. Bohler, G. Bouchard, C. Bostedt, M. Boyes, K. Chow, D. Cocco, F. J. Decker, Y. Ding, C. Eckman, P. Emma, D. Fairley, Y. Feng, C. Field, U. Flechsig, G. Gassner, J. Hastings, P. Heimann, Z. Huang, N. Kelez, J. Krzywinski, H. Loos, A. Lutman, A. Marinelli, G. Marcus, T. Maxwell, P. Montanez, S. Moeller, D. Morton, H. D. Nuhn, N. Rodes, W. Schlotter, S. Serkez, T. Stevens, J. Turner, D. Walz, J. Welch and J. Wu, *Physical Review Letters*, 2015, **114**, 054801.

(53) Getoni Gianluca, Kocharyan Vitali and Saldin Evgeni, *arXiv: Accelerator Physics*, 2010.

(54) S. Schreiber and B. Faatz, *High Power Laser Science and Engineering*, 2015, **3**, e20.

(55) H. Weise, W. Decking et al., *Proc. FEL'17*, 2017, 9–13.

(56) M. Yabashi, H. Tanaka and T. Ishikawa, *Journal of synchrotron radiation*, 2015, **22**, 477–484.

(57) E. Allaria, L. Badano, S. Bassanese, F. Capotondi, D. Castronovo, P. Cinquegrana, M. Danailov, G. D'auria, A. Demidovich, R. De Monte et al., *Journal of synchrotron radiation*, 2015, **22**, 485–491.

(58) I. S. Ko, H.-S. Kang, H. Heo, C. Kim, G. Kim, C.-K. Min, H. Yang, S. Y. Baek, H.-J. Choi, G. Mun et al., *Applied Sciences*, 2017, **7**, 479.

(59) Z. Zhao, D. Wang, Q. Gu, L. Yin, G. Fang, M. Gu, Y. Leng, Q. Zhou, B. Liu, C. Tang et al., *Synchrotron Radiation News*, 2017, **30**, 29–33.

(60) C. J. Milne, T. Schietinger, M. Aiba, A. Alarcon, J. Alex, A. Anghel, V. Arsov, C. Beard, P. Beaud, S. Bettoni et al., *Applied Sciences*, 2017, **7**, 720.

(61) J. Grünert, M. P. Carbonell, F. Dietrich, T. Falk, W. Freund, A. Koch, N. Kujala, J. Laksman, J. Liu, T. Maltezopoulos et al., *Journal of Synchrotron Radiation*, 2019, **26**, 1422–1431.

(62) J. Galayda, 9th International Particle Accelerator Conference, 2018.

(63) T. Liu, N. Huang, H. Yang, Z. Qi, K. Zhang, Z. Gao, S. Chen, C. Feng, W. Zhang, H. Luo et al., *Frontiers in Physics*, 2023, **11**, 1172368.

(64) A. McPherson, G. Gibson, H. Jara, U. Johann, T. S. Luk, I. McIntyre, K. Boyer and C. K. Rhodes, *JOSA B*, 1987, **4**, 595–601.

(65) W. Koch and D. J. Tannor, *Annals of Physics*, 2021, **427**, 168288.

(66) J. Li, J. Lu, A. Chew, S. Han, J. Li, Y. Wu, H. Wang, S. Ghimire and Z. Chang, *Nature Communications*, 2020, **11**, 2748.

(67) R. Forbes, F. Allum, S. Bari, R. Boll, K. Borne, M. Brouard, P. H. Bucksbaum, N. Ekanayake, B. Erk, A. J. Howard et al., *Journal of Physics B: Atomic, Molecular and Optical Physics*, 2020, **53**, 224001.

(68) K. Amini, E. Savelyev, F. Brauße, N. Berrah, C. Bomme, M. Brouard, M. Burt, L. Christensen, S. Düsterer, B. Erk, H. Höppner, T. Kierspel, F. Krecinic, A. Lauer, J. W. L. Lee, M. Müller, E. Müller, T. Mullins, H. Redlin, N. Schirmel, J. Thøgersen, S. Techert, S. Toleikis, R. Treusch, S. Trippel, A. Ulmer, C. Vallance, J. Wiese, P. Johnsson, J. Küpper, A. Rudenko, A. Rouzée, H. Stapelfeldt, D. Rolles and R. Boll, *Structural Dynamics*, 2018, **5**, 014301.

(69) F. Allum, N. Anders, M. Brouard, P. Bucksbaum, M. Burt, B. Downes-Ward, S. Grundmann, J. Harries, Y. Ishimura, H. Iwayama et al., *Faraday Discussions*, 2021, **228**, 571–596.

(70) R. Boll, B. Erk, R. Coffee, S. Trippel, T. Kierspel, C. Bomme, J. D. Bozek, M. Burkett, S. Carron, K. R. Ferguson et al., *Structural Dynamics*, 2016, **3**, 043207.

(71) B. Erk, R. Boll, S. Trippel, D. Anielski, L. Foucar, B. Rudek, S. W. Epp, R. Coffee, S. Carron, S. Schorb et al., *Science*, 2014, **345**, 288–291.

(72) H. Ryufuku, K. Sasaki and T. Watanabe, *Physical Review A*, 1980, **21**, 745.

(73) A. Niehaus, *Journal of Physics B: Atomic and Molecular Physics (1968-1987)*, 1986, **19**, 2925.

(74) M. L. Murillo-Sánchez, J. González-Vázquez, M. E. Corrales, R. de Nalda, E. Martínez-Núñez, A. García-Vela and L. Bañares, *The Journal of Chemical Physics*, 2020, **152**, 014304.

(75) M. L. Murillo-Sánchez, A. Zanchet, S. Marggi Poullain, J. González-Vázquez and L. Bañares, *Scientific Reports*, 2020, **10**, 2045–2322.

(76) M. E. Corrales, V. Loriot, G. Balerdi, J. González-Vázquez, R. de Nalda, L. Bañares and A. H. Zewail, *Phys. Chem. Chem. Phys.*, 2014, **16**, 8812–8818.

(77) R. Forbes, A. De Fanis, D. Rolles, S. T. Pratt, I. Powis, N. A. Besley, A. R. Milosavljević, C. Nicolas, J. D. Bozek and D. M. P. Holland, *Journal of Physics. B, Atomic, Molecular and Optical Physics*, 2020, **53**, 155101.

(78) N. Saito and I. H. Suzuki, *International Journal of Mass Spectrometry and Ion Processes*, 1992, **115**, 157–172.

(79) J. Yeh and I. Lindau, *Atomic data and nuclear data tables*, 1985, **32**, 1–155.

(80) S. W. Crane, J. W. Lee, M. N. Ashfold and D. Rolles, *Physical Chemistry Chemical Physics*, 2023, **25**, 16672–16698.

(81) M. E. Corrales, J. González-Vázquez, R. Nalda and L. Bañares, *The journal of physical chemistry letters*, 2018, **10 2**, 138–143.

(82) C. Slater, S. Blake, M. Brouard, A. Lauer, C. Vallance, C. Bohun, L. Christensen, J. Nielsen, M. P. Johansson and H. Stapelfeldt, *Physical Review A*, 2015, **91**, 053424.

(83) S. Owada, K. Togawa, T. Inagaki, T. Hara, T. Tanaka, Y. Joti, T. Koyama, K. Nakajima, H. Ohashi, Y. Senba, T. Togashi, K. Tono, M. Yamaga, H. Yumoto, M. Yabashi, H. Tanaka and T. Ishikawa, *Journal of Synchrotron Radiation*, 2018, **25**, 282–288.

(84) S. Owada, M. Fushitani, A. Matsuda, H. Fujise, Y. Sasaki, Y. Hikosaka, A. Hishikawa and M. Yabashi, *Journal of Synchrotron Radiation*, 2020, **27**, 1362–1365.

(85) T. Tanaka, M. Kato, N. Saito, S. Owada, K. Tono, M. Yabashi and T. Ishikawa, *Nuclear Instruments and Methods in Physics Research Section A: Accelerators, Spectrometers, Detectors and Associated Equipment*, 2018, **894**, 107–110.

(86) S. Owada, K. Nakajima, T. Togashi, T. Katayama, H. Yumoto, H. Ohashi and M. Yabashi, *Journal of Synchrotron Radiation*, 2019, **26**, 887–890.

(87) H. Fukuzawa, K. Nagaya and K. Ueda, *Nuclear Instruments and Methods in Physics Research Section A: Accelerators, Spectrometers, Detectors and Associated Equipment*, 2018, **907**, Advances in Instrumentation and Experimental Methods, 116–131.

(88) A. T. J. B. Eppink and D. H. Parker, *Review of Scientific Instruments*, 1997, **68**, 3477–3484.

(89) E. Rennie, L. Cooper, L. Shpinkova, D. Holland, D. Shaw and P. Mayer, *International Journal of Mass Spectrometry*, 2010, **290**, 142–144.

(90) J. Butler and T. Baer, *Journal of the American Chemical Society*, 1980, **102**, 6764–6769.

(91) L. M. Culberson, C. C. Blackstone, A. A. Wallace and A. Sanov, *The Journal of Physical Chemistry A*, 2015, **119**, 9770–9777.

(92) L. M. Culberson and A. Sanov, *The Journal of Chemical Physics*, 2011, **134**, 204306.

(93) J. A. DeVine, M. L. Weichman, S. J. Lyle and D. M. Neumark, *Journal of Molecular Spectroscopy*, 2017, **332**, 16–21.

(94) M. Frisch, G. Trucks, H. Schlegel, G. Scuseria, M. Robb, J. Cheeseman, J. Montgomery Jr, T. Vreven, K. Kudin, J. Burant et al., *Google Scholar There is no corresponding record for this reference*, 2013.

(95) T. H. Dunning Jr, *The Journal of chemical physics*, 1989, **90**, 1007–1023.

(96) F. Allum, V. Music, L. Inhester, R. Boll, B. Erk, P. Schmidt, T. M. Baumann, G. Brenner, M. Burt, P. V. Demekhin, S. Dörner, A. Ehresmann, A. Galler, P. Grychtol, D. Heathcote, D. Kargin, M. Larsson, J. W. L. Lee, Z. Li, B. Manschwetus, L. Marder, R. Mason, M. Meyer, H. Otto, C. Passow, R. Pietschnig, D. Ramm, K. Schubert, L. Schwob, R. D. Thomas, C. Vallance, I. Vidanović, C. von Korff Schmising, R. Wagner, P. Walter, V. Zhaunerchyk, D. Rolles, S. Bari, M. Brouard and M. Ilchen, *Communications Chemistry*, 2022, **5**, 42.

(97) F. Allum, Y. Kumagai, K. Nagaya, J. Harries, H. Iwayama, M. Britton, P. H. Bucksbaum, M. Burt, M. Brouard, B. Downes-Ward, T. Driver, D. Heathcote, P. Hockett, A. J. Howard, J. W. L. Lee, Y. Liu, E. Kukk, J. W. McManus, D. Milsesevic, A. Niozu, J. Niskanen, A. J. Orr-Ewing, S. Owada, P. A. Robertson, A. Rudenko, K. Ueda, J. Unwin, C. Vallance, T. Walmsley, R. S. Minns, D. Rolles, M. N. R. Ashfold and R. Forbes, *Phys. Rev. A*, 2023, **108**, 043113.

(98) R. Boschi and D. Salahub, *Molecular Physics*, 1972, **24**, 289–299.

(99) A. Gedanken and M. D. Rowe, *Chemical Physics Letters*, 1975, **34**, 39–43.

(100) S. Pathak, L. M. Ibele, R. Boll, C. Callegari, A. Demidovich, B. Erk, R. Feifel, R. Forbes, M. Di Fraia, L. Giannessi, C. S. Hansen, D. M. P. Holland, R. A. Ingle, R. Mason, O. Plekan, K. C. Prince, A. Rouzée, R. J. Squibb, J. Tross, M. N. R. Ashfold, B. F. E. Curchod and D. Rolles, *Nature Chemistry*, 2020, **12**, 795–800.

(101) I. Gabalski, M. Sere, K. Acheson, F. Allum, S. Boutet, G. Dixit, R. Forbes, J. M. Glownia, N. Goff, K. Hegazy et al., *The Journal of Chemical Physics*, 2022, **157**.

(102) Y. Lee, K. Y. Oang, D. Kim and H. Ihee, *Structural Dynamics*, 2024, **11**, 031301.

(103) S. Boutet and G. J. Williams, *New Journal of Physics*, 2010, **12**, 035024.

(104) B. E. Warren, *X-ray Diffraction*, Courier Corporation, 1990.

(105) J. D. Jackson, *Classical electrodynamics*, John Wiley & Sons, 2012.

(106) J. T. Randall, *The diffraction of X-rays and electrons by amorphous solids, liquids, and gases*, Chapman & Hall London, 1934.

(107) E. Prince and P. Boggs, *International Tables for Crystallography, Volume C: Mathematical, physical and chemical tables*, Wiley Online Library, 1995.

(108) A. H. Compton, *Physical review*, 1923, **21**, 483.

(109) P. Debye, *Annalen der Physik*, 1915, **351**, 809–823.

(110) J. H. Hubbell, W. J. Veigele, E. Briggs, R. Brown, D. Cromer and d. R. Howerton, *Journal of physical and chemical reference data*, 1975, **4**, 471–538.

(111) J. Cao and K. R. Wilson, *The Journal of Physical Chemistry A*, 1998, **102**, 9523–9530.

(112) G. Marcus, G. Penn and A. A. Zholents, *Phys. Rev. Lett.*, 2014, **113**, 024801.

(113) M. P. Minitti, J. S. Robinson, R. N. Coffee, S. Edstrom, S. Gilevich, J. M. Glownia, E. Granados, P. Hering, M. C. Hoffmann, A. Miahnahri et al., *Journal of synchrotron radiation*, 2015, **22**, 526–531.

(114) J. M. Glownia, J. Cryan, J. Andreasson, A. Belkacem, N. Berrah, C. Blaga, C. Bostedt, J. Bozek, L. DiMauro, L. Fang et al., *Optics express*, 2010, **18**, 17620–17630.

(115) M. Harmand, R. N. Coffee, M. R. Bionta, M. Chollet, D. French, D. Zhu, D. M. Fritz, H. T. Lemke, N. Medvedev, B. Ziaja, S. Toleikis and M. Cammarata, *Nature Photonics*, 2013, **7**, 215–218.

(116) S. Redford, M. Andrä, R. Barten, A. Bergamaschi, M. Brückner, R. Dinapoli, E. Fröjdh, D. Greiffenberg, C. Lopez-Cuenca, D. Mezza, A. Mozzanica, M. Ramilli, M. Ruat, C. Ruder, B. Schmitt, X. Shi, D. Thattil, G. Tinti, S. Vetter and J. Zhang, *Journal of Instrumentation*, 2018, **13**, C01027–C01027.

(117) J. D. Cardoza, R. C. Dudek, R. J. Mawhorter and P. M. Weber, *Chemical physics*, 2004, **299**, 307–312.

(118) B. R. Miller and M. Fink, *The Journal of Chemical Physics*, 1981, **75**, 5326–5328.

(119) M. R. Ware, J. M. Glownia, N. Al-Sayyad, J. T. O'Neal and P. H. Bucksbaum, *Physical Review A*, 2019, **100**, 033413.

(120) P. H. Bucksbaum, M. R. Ware, A. Natan, J. P. Cryan and J. M. Glownia, *Phys. Rev. X*, 2020, **10**, 011065.

(121) G. Wu, P. Hockett and A. Stolow, *Phys. Chem. Chem. Phys.*, 2011, **13**, 18447–18467.

(122) G. L. Abma, M. A. Parkes, W. O. Razmus, Y. Zhang, A. Wyatt, E. Springate, R. Chapman, D. A. Horke and R. S. Minns, *Journal of the American Chemical Society*, 2024, **146**, 12595–12600.

(123) E. Springate, C. Froud, I. C. E. Turcu, S. S, D. Wolff, S. Hook, B. Landowski, J. Underwood, A. Cavalleri, S. Dhesi, F. Frassetto, S. Bonora, L. Poletto and P. Villoresi, *Artemis: synchronised XUV and laser sources for ultrafast time-resolved science*.